Johannes Gutenberg University of Mainz

Doctoral Thesis

Imaging Spin-Filter Efficiency of W(001) and Ir(001) Single Crystals

Author:

Dmytro Kutnyakhov

Born in Romny (Ukraine)

Dissertation in Physics

to obtain the degree of

"Doktor der Naturwissenschaften"

in the

Faculty 08: Physics, Mathematics and Computer Science

Institute of Physics

11.February.2014

1. Berichterstatter:
2. Berichterstatter:

Tag der mündlichen Prüfung: 28.April.2014

D77 Mainzer Dissertation

Kurzfassung

Doktor der Naturwissenschaften
Effizienz abbildender Spinfilter von W(001) und Ir(001)-Einkristallen
von Dmytro KUTNYAKHOV

Während der letzten Jahre wurde für Spinfilter-Detektoren ein wesentlicher Schritt in Richtung stark erhöhter Effizienz vollzogen. Das ist eine wichtige Voraussetzung für spinaufgelöste Messungen mit Hilfe von modernen Elektronenspektrometern und Impulsmikroskopen. In dieser Doktorarbeit wurden bisherige Arbeiten der parallel abbildenden Technik weiterentwickelt, die darauf beruht, dass ein elektronenoptisches Bild unter Ausnutzung der **k**-parallel Erhaltung in der Niedrigenergie-Elektronenbeugung auch nach einer Reflektion an einer kristallinen Oberfläche erhalten bleibt. Frühere Messungen basierend auf der spekularen Reflexion an einer W(001) Oberfläche [Kolbe et al., 2011; Tusche et al., 2011] wurden auf einen viel größeren Parameterbereich erweitert und mit Ir(001) wurde ein neues System untersucht, welches eine sehr viel längere Lebensdauer der gereinigten Kristalloberfläche im UHV aufweist. Die Streuenergie- und Einfallswinkel-"Landschaft" der Spinempfindlichkeit S und der Reflektivität I/I_0 von gestreuten Elektronen wurde im Bereich von 13.7 - 36.7 eV Streuenergie und 30° - 60° Streuwinkel gemessen. Die dazu neu aufgebaute Messanordnung umfasst eine spinpolarisierte GaAs Elektronenquelle und einen drehbaren Elektronendetektor (Delayline Detektor) zur ortsauflösenden Detektion der gestreuten Elektronen. Die Ergebnisse zeigen mehrere Regionen mit hoher Asymmetrie und großem Gütefaktor (figure of merit FoM), definiert als $S^2 \cdot I/I_0$. Diese Regionen eröffnen einen Weg für eine deutliche Verbesserung der Vielkanal-Spinfiltertechnik für die Elektronenspektroskopie und Impulsmikroskopie.

Im praktischen Einsatz erwies sich die Ir(001)-Einkristalloberfläche in Bezug auf. längere Lebensdauer im UHV (ca. 1 Messtag), verbunden mit hoher FOM als sehr vielversprechend. Der Ir(001)-Detektor wurde in Verbindung mit einem Halbkugelanalysator bei einem zeitaufgelösten Experiment im Femtosekunden-Bereich am Freie-Elektronen-Laser FLASH bei DESY eingesetzt. Als gute Arbeitspunkte erwiesen sich 45° Streuwinkel und 39 eV Streuenergie, mit einer nutzbaren Energiebreite von 5 eV, sowie 10 eV Streuenergie mit einem schmaleren Profil von $<$ 1 eV aber etwa 10× größerer Gütefunktion. Die Spinasymmetrie erreicht Werte bis 70 %, was den Einfluss von apparativen Asymmetrien deutlich reduziert. Die resultierende Messungen und Energie-Winkel-Landschaft zeigt recht gute Übereinstimmung mit der Theorie (relativistic layer-KKR SPLEED code [Braun et al., 2013; Feder et al., 2012])

Abstract

Doktor der Naturwissenschaften

Imaging Spin-Filter Efficiency of W(001) and Ir(001) Single Crystals

by Dmytro KUTNYAKHOV

Recently, spin-filter detectors made a prominent step forward towards strongly increased efficiency meeting the needs of modern electron spectrometers and momentum microscopes. In this thesis previous work on the novel imaging spin-filter technique that can transport a full image by making use of **k**-parallel conservation in low-energy electron diffraction based on specular reflection from W(001) [Kolbe et al., 2011; Tusche et al., 2011], was extended to a much larger parameter space for W(001) and to the new Ir(001) system, which shows a much longer lifetime of the prepared crystal surface in UHV than the W(001) surface. The scattering energy and angle of incidence landscape of the spin sensitivity S, and reflectivity I/I_0 of spin-polarized primary electrons was measured in the region of 13.7 - 36.7 eV scattering energy and $30° - 60°$ scattering angle. The setup includes a spin-polarized GaAs electron source and a rotatable delayline detector for spatially-resolving detection of the scattered electrons. The results identify several regions of high asymmetry and large figure of merit. The latter is defined as $S^2 \cdot I/I_0$. These regions open a path for a substantial improvement of the multichannel spinfilter for electron spectroscopy and momentum microscopy with optimal performance.

Searching for a longer "lifetime" in UHV combined with a high analyzing power as spin polarimeter we found the Ir(001) single crystal surface being promising. The novel detector was placed behind a dispersive electron energy analyzer and has been used in a time-resolved experiment in the femtosecond region at the free-electron laser FLASH at DESY. For 45° scattering angle a good working point appears at 39 eV scattering energy revealing a broad asymmetry maximum of 5 eV usable width. A second one at about 10 eV exhibits a narrower profile < 1 eV but much longer figure of merit. The Ir surface showed a stable efficiency for a full measurement day. The asymmetry function reaches values of 70 % which considerably reduces the significance of spurious asymmetries. The resulting measurements and energy-angular landscape show rather good agreement with theory (relativistic layer-KKR SPLEED code [Braun et al., 2013; Feder et al., 2012]).

Contents

List of Figures

List of Tables

Abbreviations

AES - Auger electron spectroscopy

APW – augmented plane wave

CCD – charge-coupled device

CMA – cylindrical mirror analyser

DLD – delay line detector

FEL – free electron laser

FLAPW – full-potential linearised augmented plane wave

FWHM – full width at half maximum

IMFP – inelastic mean free path

HAXPES – hard x-ray photoemission electron spectroscopy

KKR – Koringa-Kohr-Rostoker

LAPW – linear augmented plane wave

LEED – low energy electron diffraction

MCD – magnetic circular dichroism

MCP – multi channel plate

NEA – negative electron affinity

PEEM – photoemission electron microscopy

SEMPA – scanning electron microscope with polarization analysis

SPLEED – spin polarized low energy electron diffraction

FoM – figure of merit

UHV – ultra-high vacuum

VLEED – very low energy electron diffraction

VUV – vacuum ultra violet

Chapter 1

Introduction

Stern-Gerlach-type spin filters for electrons are impossible because of the interplay between Lorentz force and Heisenberg uncertainty relation. Spin analysis of electron beams is accomplished by spin dependent scattering processes that are based on spin-orbit or exchange interaction. In the high energy range Mott-scattering at high-Z targets or Moller scattering at ferromagnetic targets are exploited. In the energy range below 100 eV spin polarized low energy electron diffraction (SPLEED) at high-Z single crystals or at ferromagnetic surfaces can be utilized (for details, see textbooks [Feder, 1985; Kessler, 1976; Kirschner, 1985]. All of these are inherently single-channel methods. The spin-detection efficiency is given by the *figure of merit* (definition see Eq. 3.1). Mostly used spin polarimeters of the present generation, e.g. the Mott detector [Gay, 2009] or SPLEED detector [Kirschner and Feder, 1979; Yu et al., 2007] utilizing the (2,0)-reflexes from a W(001) surface are characterized by a low figure of merit of the order of 10^{-4}. Two orders of magnitude can be gained via exchange scattering from an Fe surface [Bertacco et al., 1998; Hillebrecht et al., 2002; Okuda et al., 2008; Winkelmann et al., 2008]. Lateral resolution can only be achieved by scanning the electron beam across a sample like in scanning electron microscopy with polarization analysis (SEMPA).

A strong discrepancy becomes obvious when comparing spin detector development with the development of electron spectrometers. The advent of multichannel detection increased detection efficiency by orders of magnitude. A modern hemispherical analyzer acquires a certain energy and angular interval simultaneously, detecting up to 10^4 data points in parallel. Comparing such a hemispherical energy analyzer with multichannel intensity detection and a spectrometer with state-of-the-art single channel spin polarimeter, we are facing a total loss in detection efficiency by 6-7 orders of magnitude!

Our basic idea for a substantial improvement of the performance of spin detectors was to *conserve the lateral distribution* of the electrons in a beam during the scattering process. In photoemission electron microscopy (PEEM) this requires to implement a reflection-type spin filter into the column of the microscope. In electron spectrometer applications, it means to adopt the multichannel detection concept that is so effective in intensity spectroscopy. The new approach exploits that an electron-diffraction process can transmit lateral image information. Owing to $\mathbf{k}_\parallel$ momentum conservation, the specular beam in low-energy electron diffraction (LEED) behaves like a photon beam reflected at an optical mirror. The idea to exploit $\mathbf{k}_\parallel$-conservation in a SPLEED setup brought up the concept of *2D electron spin filtering of PEEM images* [Tusche et al., 2013, 2011]. Moreover, it opened the door to a substantial improvement of spin detection efficiency in spectroscopic applications, e.g. behind a *hemispherical electron spectrometer* [Hahn et al., 2011; Kolbe et al., 2012] and in the future spin filtering of momentum distributions.

This work is organized as follows:

In **Chapter 2** we describe appropriate theoretical concepts. Thus, we briefly discuss spin polarization of an electron beam in Ch. 2.1 as well as the fundamental spin-dependent interactions spin-orbit and exchange coupling in Ch. 2.2. Additionally, in Ch. 2.3 we discuss the basics of the one electron picture. Mainly we focus on the theory of spin-polarized low energy electron diffraction (SPLEED), which is explained in the Ch. 2.4.

In **Chapter 3** and **4** we present and discuss the experimental results. Since the measurements for this thesis have been carried out using two different imaging spin filters for electrons based on specular reflection from W(001) as well as from Ir(001), the result were separated in individual chapters. One set of measurements was done at the University of Mainz and the second one at two synchrotron facilities: the Swiss Light Source (SLS) at the Paul Scherrer Institut (Villigen, Switzerland) and at FLASH, the soft X-ray free-electron laser (FEL) at DESY (Hamburg, Germany)respectively. Therefore, two different experimental setups are described in these chapters.

In **Chapter 5** we summarize the results, illuminate the scientific findings and give some conclusions for future applications which can be drawn from their interpretation.

Chapter 2

Theoretical background

2.1 Spin polarization of an electron beam

On the basis of the textbooks of J. Kessler [Kessler, 1976], J. Kirschner [Kirschner, 1985] and R. Feder [Feder, 1985] we recall the basics of spin-polarized low-energy electron diffraction (SPLEED).

Spin polarization of an electron beam can be determined by the number of electrons in the two possible spin states ("up" or "down") with respect to a given spatial direction. If each electron in the beam has the same spin – the electrons are totally polarized, or have polarization (absolute value) of 1. If the number of electrons in both states is equal, they are unpolarized, or have a polarization of 0 along that direction.

The spin of an electron can be described with the help of a spin operator ($\mathbf{s} = s_x, s_y, s_z$) satisfying the permutation relation $[s_x, s_y] = -is_z$ (and cyclic permutations). Using the vector of Pauli matrices, $\boldsymbol{\sigma}$, we can represent the vector spin operator in the limit of nonrelativistic interactions, which may be assumed for low-energy electrons (although the spin itself is a relativistic phenomenon):

$$\mathbf{s} = \frac{\hbar}{2}\boldsymbol{\sigma}, \tag{2.1}$$

where the spin operator is proportional to the operator of the angular momentum **s**.

The polarization **P** is a vector, given by the expectation value of the spin operator:

$$\mathbf{P} = \frac{\langle\chi|\boldsymbol{\sigma}|\chi\rangle}{\langle\chi|\chi\rangle}. \tag{2.2}$$

The degree of polarization parallel to the quantization axis z is a scalar:

$$P_z = \frac{\langle\chi|\sigma_z|\chi\rangle}{\langle\chi|\chi\rangle} = \frac{|a_1|^2 - |a_2|^2}{|a_1|^2 + |a_2|^2} = \frac{N^{\uparrow} - N^{\downarrow}}{N^{\uparrow} + N^{\downarrow}}, \tag{2.3}$$

with $-1 \leq P_z \leq 1$. $N^{\uparrow}$ ($N^{\downarrow}$) denotes the number of electrons with spin parallel $s_z = +1/2$ (antiparallel $s_z = -1/2$) to the quantization axis. The polarization state can be described by $\chi = \begin{pmatrix} a_1 \\ a_2 \end{pmatrix}$. A mixed spin state is described by the density matrix, essentially a sum over pure spin states with appropriate coefficients [Kessler, 1976].

2.2 Spin-orbit and exchange coupling

One of the many effects of the electron having an intrinsic spin angular momentum is the coupling between the spin and the electron's own orbital angular momentum. This is the so called spin-orbit coupling and can be an important interaction in solid state electronic structures. It is also the interaction at the heart of the most popular types of instruments for electron spin analysis.

As a first step in the calculation of an electron scattering process, one examines the scattering by a radially symmetric potential $V(r)$. In the vicinity of the atomic nucleus, electrons acquire relativistic velocities, i.e. the relativistic Dirac equation has to be solved. As a direct consequence, the spin of the electron is always coupled to its orbital momentum. In a nonrelativistic approximation, this spin-orbit interaction can be characterized by an additional spin-orbit interaction potential

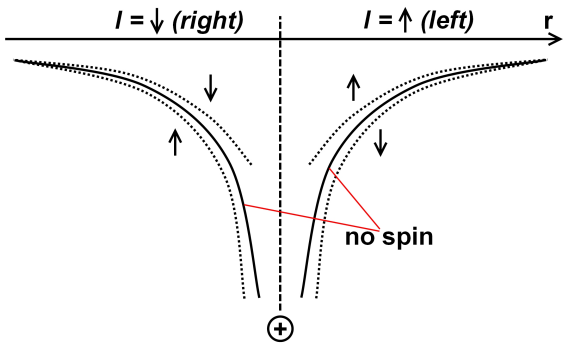

FIGURE 2.1: Scattering potential of a nucleus: including spin-orbit interaction (dotted lines) and plain Coulomb potential (solid lines) for electrons with spin up ↑ and spin down ↓. Figure adapted from [Kessler, 1976].

[Kessler, 1976]:

$$V_{so} = \frac{1}{2m^2c^2}\frac{1}{r}\frac{dV}{dr}(\mathbf{s}\cdot\mathbf{l}), \tag{2.4}$$

where $\mathbf{s}$ is the spin and $\mathbf{l}$ is the orbital moment operator. The spin direction and the path of the electron, left-hand or right-hand around the nucleus, derive the sign of this additional spin-orbit potential. In the rest system of the electron, the positive charge of the nucleus forming the scattering potential passes by and generates a magnetic field, which interacts with the magnetic moment of the electron (see Fig. 2.1).

Considering that the electron travels along the x-axis and transversally polarized parallel to the z axis it scatters in the x-y plane at a scattering angle θ (thus the orbital moment is parallel to the spin). The spin-orbit interaction results in different differential scattering cross sections for spin-up and spin-down electrons $\sigma^{\uparrow}(E,\theta)$ and $\sigma^{\downarrow}(E,\theta)$. Spin-orbit coupling contributes quite weakly to the total scattering potential. Significant differences depending on the spin can be observed essentially near minima of the differential cross sections. The *spin-orbit scattering asymmetry* is defined as:

$$A_{so}(\theta) = \frac{\sigma^{\uparrow}(\theta) - \sigma^{\downarrow}(\theta)}{\sigma^{\uparrow}(\theta) + \sigma^{\downarrow}(\theta)}. \tag{2.5}$$

The proportionality of the number of scattered electrons N to the scattering cross

section leads to the polarization of an unpolarized electron beam after the scattering according to:

$$P = A_{so}(\theta) = \frac{N^{\uparrow}(\theta) - N^{\downarrow}(\theta)}{N^{\uparrow}(\theta) + N^{\downarrow}(\theta)}, \tag{2.6}$$

with the *polarizing power* P [Kessler, 1976]. For a given mirror symmetry of the scattering potential with respect to the scattering plane, change of sign of the orbital momentum will be equivalent to a change of sign of the polarization: $\sigma^{\uparrow}(-\theta)=\sigma^{\downarrow}(\theta)$ and consequently $A_{so}(\theta) = -A_{so}(-\theta)$. This relation is often referred to as "Left-right asymmetry". Assuming a totally polarized electron beam one will measure an asymmetry A according to [Feder, 1981]:

$$A = \frac{N^{\uparrow}(\theta) - N^{\downarrow}(-\theta)}{N^{\uparrow}(\theta) + N^{\downarrow}(-\theta)} = \frac{\sigma^{\uparrow}(\theta) - \sigma^{\downarrow}(\theta)}{\sigma^{\uparrow}(\theta) + \sigma^{\downarrow}(\theta)} = P. \tag{2.7}$$

Thus, due to the spin-orbit coupling the polarization generated by the scattering of an unpolarized electron beam is identical to the scattering asymmetry produced by a totally polarized electron beam (analyzing power equals polarizing power).

As a result of the requirement of antisymmetry in particle permutation usually interactions and properties of many-electron systems are explained by the term exchange. *Exchange coupling* is a quantum-mechanical effect, which does not have any classical analogue. The Pauli principle, demanding for spin-1/2 particles a totally antisymmetric wave function, is the origin of the exchange coupling. The wave function is antisymmetric with respect to the exchange of any two particles and the differential scattering cross section depends on the relative orientation between the spin of the incoming electron and the spin of the target (e.g., a polarized atom). If we consider the scattering of polarized electrons $e^{\uparrow\downarrow}$ at polarized atoms $A^{\uparrow\downarrow}$ with neglection of spin-orbit coupling, then we have the following scattering channels:

$$e^{\downarrow} + A^{\uparrow} \rightarrow e^{\downarrow} + A^{\uparrow} \quad (|f|^2), \tag{2.8a}$$

$$e^{\downarrow} + A^{\uparrow} \rightarrow e^{\uparrow} + A^{\downarrow} \quad (|g|^2), \tag{2.8b}$$

$$e^{\uparrow} + A^{\uparrow} \rightarrow e^{\uparrow} + A^{\uparrow} \quad (|f - g|^2). \tag{2.8c}$$

Thus, we have direct scattering of electrons without exchange scattering amplitude f (2.8a), exchange scattering (spin-flip) with amplitude g – (2.8b). Since the electrons cannot be distinguished, one may have exchange or direct scattering in case (2.8c). Direct determination of the scattering cross section can be done in a complete experiment where one knows the polarization of electron and atom before and after the scattering. When unpolarized electrons are scattered at a polarized target, the scattered electrons are polarized according to:

$$A_{ex}(\theta) = \frac{|g|^2 + |f-g|^2 - |f|^2}{|f|^2 + |g|^2 + |f-g|^2} = P(\theta). \tag{2.9}$$

Also the exchange scattering provides contributions to the total scattering cross section, in all cases when electrons are scattered at a polarized target. It is true even during scattering of unpolarized electrons if no polarization analysis is performed. The total cross section for scattering at a spin-up polarized atom $A^{\uparrow}$ is then given by

$$\sigma_0(\theta) = \frac{1}{2}(|f|^2 + |g|^2 + |f-g|^2). \tag{2.10}$$

The same cross section can be obtained for a spin-down polarized target $A^{\downarrow}$, since the cross section depends only on the relative orientation of electron spin and target spin. Therefore, changing of the magnetization direction does not change the intensity of the scattered electron beam along the direction θ. The scattered intensity also remains constant when the polarization of an incident polarized beam on an unpolarized target is reversed. Additionally, there is no left-right asymmetry for the case of exchange scattering in comparison to spin-orbit scattering [Feder, 1981]:

$$A_{ex}(\theta) = A_{ex}(-\theta). \tag{2.11}$$

2.3 One electron picture

According to the schematic sketch in Fig. 2.2, the relevant scattering methods can be classified by their input and output channels as follows. We assume an incident electron beam of kinetic energy E, momentum $\mathbf{k}$ and polarization $\mathbf{P}$. We

can consider: (a) detection (measurement) of elastically scattered electrons with $E' = E$, $\mathbf{k}'$ and $\mathbf{P}'$ (elastic electron scattering or more special elastic low-energy electron diffraction (LEED) from a crystalline target); (b) detection of outgoing electrons with $E' < E, \mathbf{k}'$ and $\mathbf{P}'$; this comprises inelastic electron scattering (energy loss spectroscopy), Auger emission and true secondary electron emission; (c) detection of outgoing photons with $\hbar\omega' \leq E - E_F$ (bremsstrahlung, appearance potential spectroscopy, inverse photoemission). For incident electromagnetic radiation (photons $\hbar\omega$), the most interesting polarized-electron emission process is photoemission [Feder, 1985].

In particular, this work deals with LEED with an emphasis on spin-polarized low-energy electron diffraction (SPLEED). In this method electrons with energies below about 200 eV, which have mean free paths in solids of the order of a few nearest-neighbor distances and are therefore particularly suited for studying the surface region, which typically comprises a few monoatomic layers. The observable quantities, such as the cross section (intensity) and polarization of the outgoing electrons as functions of the intensity and polarization of the incident projectiles, depending on the energy and on the scattering geometry are carrying the information about the surface system.

In general we have an electron, which is added to or removed from a surface [Feder et al., 1983], i.e. we are dealing with single particle excitation of an inhomogeneous many-electron system. In order to find a solution of this many-body problem, it is a common approach to reduce it to an effective one-electron problem using several simplifying assumptions. In the limit of nonrelativistic interaction the effective Dirac Hamiltonian can be written as

$$H = c\boldsymbol{\alpha}p + \beta mc^2 + V(E, \mathbf{r}) - \beta\overline{\boldsymbol{\sigma}}\mathbf{B}(E, \mathbf{r}), \tag{2.12}$$

where E is the energy of electron, c the velocity of light, m the electron rest mass. The effective electrostatic potential $V(E, r)$, which incorporates the Coulomb interaction with the nuclei and the electrons of the solid, exchange and correlation effects plus the influence of inelastic processes. The effective magnetic field $\mathbf{B}(E, \mathbf{r})$,

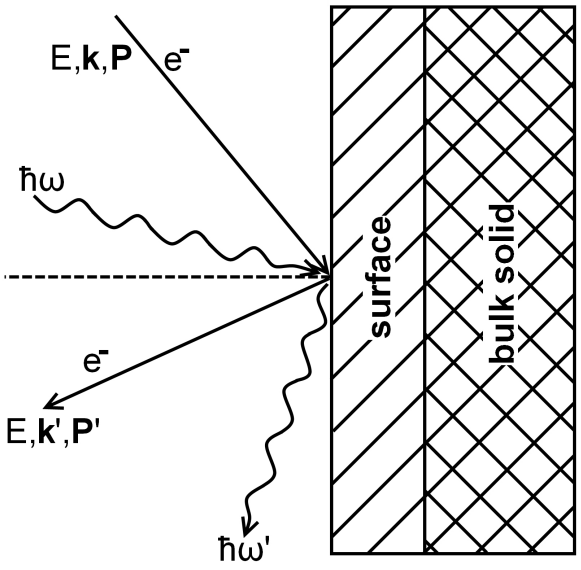

FIGURE 2.2: Scattering methods based on incoming polarized electrons (e^-) and linearly or circularly polarized photons ($\hbar\omega'$). Figure adapted from [Feder, 1985].

arises from exchange, correlation and (spin-dependent) inelastic scattering in the case of ferromagnetic ordering. The (4×4) matrices α_k, β, σ_k (with k=1,2,3) can be expressed in terms of the usual (2×2) Pauli matrices $\overline{\sigma_k}$ (with k=1,2,3) as the tensor products (see details in [Feder et al., 1983])

$$H = \frac{p^2}{2m} + V(E,\mathbf{r}) - \boldsymbol{\sigma}\mathbf{B}(E,\mathbf{r}) - \frac{p^4}{8m^3c^2} + \frac{\hbar}{4m^2c^2}\boldsymbol{\sigma} \cdot [\nabla V(E,\mathbf{r}) \times \mathbf{p}]. \quad (2.13)$$

The first three terms represent the standard Pauli Hamiltonian, and the last three give the relativistic mass correction, the Darwin term and spin-orbit coupling. Neglecting the spin-orbit coupling and assuming that the effective magnetic field $\mathbf{B}(E,\mathbf{r})$ has a uniform direction throughout the system, chosen as the z-axis, we have the (2×2) matrix Eq. (2.13), which is diagonal and consist of two "scalar relativistic" (or – without the mass correction and Darwin terms – Schrödinger) Hamiltonians with a spin-up potential $V^+(E,\mathbf{r})$ and spin-down potential $V^-(E,\mathbf{r})$, respectively.

$$V^{\pm}(E,\mathbf{r}) = V(E,\mathbf{r}) \pm B(E,\mathbf{r}), \quad (2.14)$$

where $B = \mathbf{B}\hat{\mathbf{z}}$. Spin-orbit coupling is always present in reality, therefore whether

it may be neglected or not, depends on the physical properties and mechanisms of study, and on the atomic number Z of the material (recalling that spin-orbit interaction increases with Z).

V and B can be expressed in terms of spin-dependent effective potentials $V^s(E, \mathbf{r})$ with $s = +/-$ for spin up/down electrons:

$$V = \frac{1}{2}(V^+ + V^-), \;\; B = -\frac{1}{2}(V^+ - V^-). \tag{2.15}$$

The effective one-electron potential V^s consist of an electrostatic (Hartree) part V^H and self-energy part Σ^s, which in turn is made up of an exchange part Σ^s_X and Coulomb correlation part Σ^s_C:

$$V^s(E, \mathbf{r}) = V_H(r) + \Sigma^s(E, \mathbf{r}), \text{ with } \Sigma^s = \Sigma^s_X + \Sigma^s_C. \tag{2.16}$$

A local-density approximation to Σ^s:

$$\Sigma^s(E, \mathbf{r}) = \Sigma^s_h(k^s(\mathbf{r}), \rho^+(\mathbf{r}), \rho^-(\mathbf{r})) \text{ with } s = +/-, \tag{2.17}$$

where Σ^s_h is the self-energy of a quasi-particle of momentum $k^s(\mathbf{r})$ and spin s in a homogeneous electron gas with spin densities $\rho^+(\mathbf{r})$ and $\rho^-(\mathbf{r})$. The local momentum $k^s(\mathbf{r})$ is defined by

$$\frac{1}{2}(k^s(\mathbf{r}))^2 = E - V_H(\mathbf{r}) - \Sigma^s_h(k^s(\mathbf{r}), \rho^+(\mathbf{r}), \rho^-(\mathbf{r}). \tag{2.18}$$

At the Fermi energy, i.e. for $E = E_F$, $V^s(E, \mathbf{r})$ coincides with the ground state effective potential $V^s(\mathbf{r})$ as obtained in the local-spin-density approximation. Above and below E_F, however, it departs from $V^s(\mathbf{r})$. Using Hartree-Fock approximation, where exchange but not correlation is taken into account, one then has

$$V^s(E, \mathbf{r}) = V_H(\mathbf{r}) - \alpha^s(E, \mathbf{r}) 3 \left(\frac{6\rho^s(\mathbf{r})}{8\pi} \right)^{1/3}, \tag{2.19}$$

$$\alpha^s(E, \mathbf{r}) = \frac{4}{3}\Big[0.5 + \frac{(1-\eta^2)}{4\eta} ln\Big|\frac{1+\eta}{1-\eta}\Big|\Big], \tag{2.20}$$

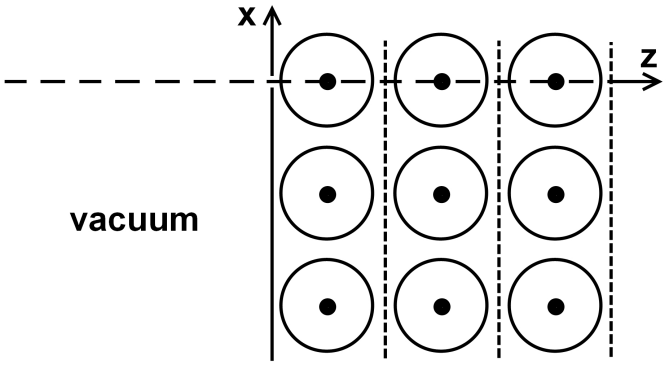

FIGURE 2.3: Schematic sketch of muffin-tin potential approximation shown in a plane perpendicular to the surface [containing the atomic nuclei (•)]. Figure adapted from [Feder, 1985].

with $\eta = \dfrac{k^s}{k_F^s}$ and $k_F^s = \left(6\pi^2\rho^s(\mathbf{r})\right)^{1/3}$. Potentials of the type of Eq. (2.19) have been found superior to ground-state potentials in scattering situations involving electrons with kinetic energies ranging from about 20 eV to several hundred eV: elastic electron-atom scattering, elastic low-energy-electron diffraction (LEED) and spin-polarized LEED [Feder, 1985].

Common quantitative theories are based on scattering potential models, which are subject of two shape restrictions of $V_r(E, r)$: (a) the muffin-tin form Fig. 2.3 (i.e. spherical symmetry around atomic sites and spatially uniform (with the real "inner potential" value $V_{or}(E)$) in the interstitial region) inside the solid for electron energies of several tens of eV and (b) a surface barrier (i.e. a potential going from the inner potential value inside the solid towards zero outside) for sufficiently high beam energy and in the surface region for "open" surfaces.

The real potential for the case of a non-magnetic semi-infinite crystal is show schematically in Fig. 2.4. In the "near region" (Fig. 2.4 for $z < 0$) it has lattice-periodic variations parallel to the surface ((x,y) plane). For $z \to -\infty$, the surface potential barriers obtained in local-density approximation obviously reaches zero together with the ground-state electron density.

Constant inner potential comprises, in addition to a real part $V_{or}(E)$, an imaginary part $V_{oi}(E)$, which determines the electron life-time τ and the (inelastic) mean free

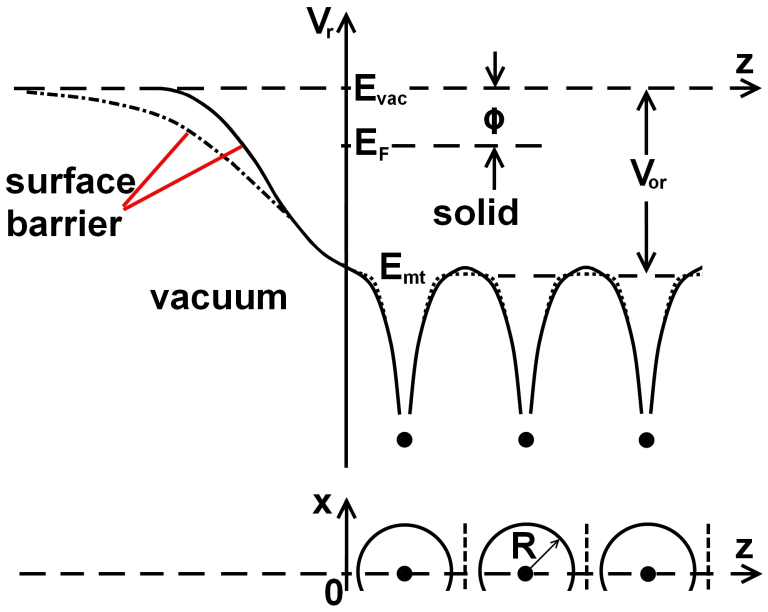

FIGURE 2.4: Influence of muffin-tin form (dotted line) and absence of shape approximation (solid line) on real part V_r of effective electron crystal potential, obtained from Eq. (2.17), where E_{vac}, E_F and E_{mt} are the vacuum, Fermi and muffin-tin levels, respectively. V_{or} is the (energy-dependent) real part of the "inner potential", and ϕ the work function. Surface potential barrier without (solid line) and with (dash-dot line) image asymptotics. Figure adapted from [Feder, 1985].

path λ according to

$$\tau(E) = (2|V_{oi}(E)|)^{-1} \text{ [Hart}^{-1}\text{]} \text{ and } \lambda(E) = \tau\sqrt{2(E+V_{or})} \text{ [Bohr]}. \tag{2.21}$$

Where E is the kinetic energy (in Hartree; atomic units: $\hbar = m_e = 1$) (relative to the vacuum zero). Usually the imaginary potential is of the order of 4 eV, which phenomenologically takes into account the effect of the removal of electrons from the elastic channel by electron-hole pair and plasmon excitation [Feder, 1981].

2.4 Theory of SPLEED

The content of Chapter 2.4, describes the fundamental footing of *ab-initio* theory for SPLEED, has been taken from [Elmers, 2007; Feder, 1985].

Using spherically symmetric potentials (within the core region) generated from *ab initio* electronic-structure calculations, one can describe electron scattering from atoms in the surface. The muffin-tin approach proves very adequate for calculating the electron reflectivity and asymmetry for electron energies of several tens of eV. In its simplest form, non-overlapping spheres are centered on the atomic positions. Within these regions ($r < R$), the screened potential experienced by an electron is approximated to be spherically symmetric about the given nucleus and as a constant in the remaining interstitial region. Continuity of the potential between the atom-centered spheres and interstitial region is enforced. In such a case wave functions, which can be expanded in terms of plane waves in the interstitial regions and in terms of spherical harmonics and the eigenfunctions of a radial Schrödinger equation in the atom-centered regions, density and potentials are defined in a piece-wise manner, i.e. consisting of some analytic form in the interstitial and numerical solutions inside the spheres. Using functions other than plane waves as basis functions brings us to the augmented plane-wave approach. It allows for an efficient representation of single-particle wave functions in the vicinity of the atomic cores where they can vary rapidly (and where plane waves would be a poor choice on convergence grounds in the absence of a pseudopotential).The imaginary part of the inner potential is slightly changing with energy and can be chosen in a way that the mean free path fits the experimentally observed universal curve.

For typical LEED energies, inside the muffin-tin spheres, the portion of the ion-core potential is mainly determined by the nuclear charge and tightly bound core-state electrons, which can not be easily polarized and retain their atomic nature in the solid environment. Therefore, this portion of the potential is, to a good approximation, spherically symmetric and stays almost unchangeable with placing the atom in the surface environment. On the other hand, the valence and conduction electrons (the outer parts of the atom) are affected by the neighboring atoms and the surface, which breaks the spherical symmetry of the ion-core potential. The distortions are significant at very low energy (< 30 eV) but play almost no role for electron energies > 50 eV. Therefore, one may use only the spherical part of bulk potentials, generated by *ab initio* electronic-structure calculations on the basis of

a quantitative theory. Such as explained below in more detail, calculation schemes for electron reflectivities and asymmetries may be used as an input self-consistently calculated ground-state potential functions provided by separate program packages. Such packages can provide different levels of sophistication depending on the particular system and required accuracy for the calculations. Self-consistent band structure calculations are useful for well ordered structures using the full potential linearized augmented plane-wave (FLAPW) method provided by Blaha, Schwarz, Sorantin and Tricky [Blaha et al., 1990] and Schwarz, Blaha and Madsen [Schwarz et al., 2002] (Wien2k 04). In this method, only core states are handled relativistically. For less ordered structures, e.g. random alloys, it is appropriate to carry out self-consistent band structure calculations using the Korringa-Kohn-Rostocker (KKR) method provided by Akai [Akai, 1998] and Kotani and Akai [Kotani and Akai, 1996]. The program gives possibility also to deal with both approximations: muffin-tin and atomic-sphere approximation.

2.4.1 Single site scattering

According to the muffin-tin approximation the Dirac Hamiltonian Eq. (2.12) has a spherically symmetric potential V and field B inside spheres of radius R, but is itself not spherically symmetric because of $\tilde{\boldsymbol{\sigma}} \cdot \mathbf{B}$. Taking the interstitial constant potential as energy zero level, V vanishes and $B = 0$ are assumed for $r > R$. The four-spinors $\phi(\mathbf{r})$ of the time-independent Dirac equation can be expanded in spherical waves (Fig. 2.5) with radial function f and g inside a sphere,

$$\phi(\mathbf{r}) = \sum_{k\mu} \frac{1}{r} \begin{pmatrix} f_k^\mu(r) & \chi_k^\mu(\widehat{\mathbf{r}}) \\ ig_k^\mu(r) & \chi_k^\mu(\widehat{\mathbf{r}}) \end{pmatrix}. \tag{2.22}$$

The two-component spin angular functions χ occurring here given by

$$\chi_k^\mu(\widehat{\mathbf{r}}) = \sum_{\sigma=\pm 1/2} C(l\tfrac{1}{2}j; \mu-\sigma, \sigma) Y_l^{\mu-\sigma}(\widehat{\mathbf{r}}) \chi^\sigma, \tag{2.23}$$

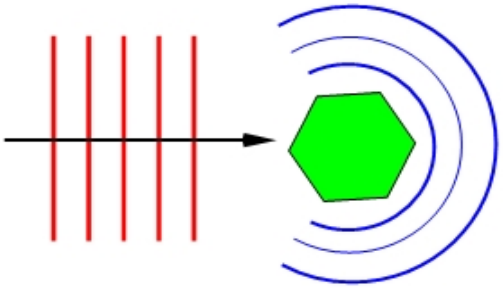

FIGURE 2.5: Single scattering – incident plane wave and scattered spherical waves. Figure adapted from [Braun et al., 2013]

where C are the Clebsch-Gordan coefficients, Y the complex spherical harmonics and χ^σ the two Pauli basis spinors.

Thus the Dirac equation transforms to a system of coupled differential equations for the radial functions, which can be easily solved in the field-free region outside the sphere (for $r > R$) [Koelling and Harmon, 1977], yielding with Eq. (2.22) incoming spherical waves with amplitudes A_k^μ and outgoing ones with amplitudes B_k^μ (with $\hbar = m = 1$)

$$A_k^\mu \begin{pmatrix} j_l(kr)\chi_k^\mu(\hat{\mathbf{r}}) \\ i\varepsilon S_k j_{\bar{l}}(kr)\chi_{-k}^\mu \end{pmatrix}, \quad B_k^\mu \begin{pmatrix} h_l^{(1)}(kr) & \chi_k^\mu(\hat{\mathbf{r}}) \\ i\varepsilon S_k h_{\bar{l}}^{(1)}(kr) & \chi_{-k}^\mu(\hat{\mathbf{r}}) \end{pmatrix}, \tag{2.24}$$

where $\varepsilon = \frac{c}{E + c^2}$, $E = (c^4 + k^2c^2)^{1/2}$, $\bar{l} = l - S_k$, and $j_l(h_l^{(1)})j_1$ are spherical Bessel functions. Therefore we can define the atomic t-matrix $\underset{\approx}{t}$ in so called $(k\mu)$ representation by

$$\mathbf{B}^{(s)} = \underset{\approx}{t} A \text{ with } \mathbf{B}^{(s)} = (\cdots, B_k^\mu, \cdots) \text{ and } \mathbf{A} = (\cdots, A_k^\mu, \cdots). \tag{2.25}$$

It can be calculated first numerically inside the sphere and then matching at R the general solution with a linear combination of outside solutions (Eq. (2.24)) with specified A_k^μ to determine the scattered B_k^μ. Since for B$\|\hat{\mathbf{z}}$ there is no μ coupling and $\underset{\approx}{t}$ is diagonal in μ. With respect to k, there are off-diagonal elements corresponding to the dominant coupling between $j = l + 1/2$ and $j = l - 1/2$, and the weak $\triangle\ l = \pm 2$ coupling. $\underset{\approx}{t}$ is also diagonal in k, for non-magnetic systems,

where these couplings are absent, and its elements t_k are $(\exp(2i\sigma_k) - 1)$, where σ_k are usual relativistic scattering phase shifts (commonly denoted by δ_l^+ and δ_l^- relating to $j = l + \frac{1}{2}$ and $j = l - \frac{1}{2}$).

With help of the above atomic t-matrix (Eq. (2.25)) and denoting by $u \cdot \exp(i\mathbf{kr})$ an incident plane wave and $v(\mathbf{k}, \mathbf{k'})$ the spinor amplitude of the asymptotic scattered wave $\exp \frac{ikr}{r}$ and recalling that free four-spinors are completely specified by their two "large" components, we look for the (2×2) matrix $\underset{\approx}{T}$ in order to completely describe the scattering process by $\tilde{v}(k, k') = \underset{\approx}{T}\tilde{u}$. This matrix transforms the two large components of u into those of v.

$$T_{\sigma'\sigma}(\mathbf{k}, \mathbf{k}') = -\frac{2\pi i}{k} \sum_{\mu\tau nn'} t^{n'}_{\mu n\tau} C(n', \tau; \mu, \sigma') \cdot C(n, \tau; \mu, \sigma) \cdot (Y^{\mu-\sigma'}_{l(n',\tau)}(\widehat{\mathbf{k}})) * Y^{\mu-\sigma}_{l(n,\tau)}(\mathbf{k}'), \tag{2.26}$$

with $C(n, \tau; \mu, \sigma) = C(l(n, \tau), \frac{1}{2}, j(n, \tau); \mu - \sigma, \sigma)$.

The index k has been expressed by the pair (n, τ) according to $k = \tau(-l)^n n$, with $n = 1, 2, \cdots$; where n (and thus k and j) compatible with the given μ and τ denotes a value required for convergence. And k and k' determine j, l and j', l' according to

$$j = |k| - \frac{1}{2}, \; l = j + \frac{S_k}{2}, \; \text{with } S_k = \frac{k}{|k|}. \tag{2.27}$$

Remembering that $\underset{\approx}{t}$ is diagonal in μ and k for non-magnetic systems, Eq. (2.26) reduces to the form

$$\underset{\approx}{T}(\mathbf{k}', \mathbf{k}) = f(\theta) + g(\theta)\widehat{\mathbf{n}} \cdot \boldsymbol{\sigma}, \; \text{with } \widehat{\mathbf{n}} = \frac{\mathbf{k} \times \mathbf{k}'}{|\mathbf{k} \times \mathbf{k}'|}, \tag{2.28}$$

$\theta = \sphericalangle(\mathbf{k}', \mathbf{k})$ is the scattering angle, and the "direct" scattering amplitude $f(\theta)$ and the "spin flip" amplitude $g(\theta)$ are given in terms of the phase shifts $\delta_l^\pm$ (for $j = l \pm \frac{1}{2}$) and Legendre polynomials P_l and P_l^1 as

$$f(\theta) = \frac{1}{2ik} \sum_l \Big((l+1)[\exp(2i\delta_l^+) - 1] + l[\exp(2i\delta_l^-) - 1] \Big) P_l(\cos\theta), \tag{2.29}$$

$$g(\theta) = \frac{1}{2ik} \sum_l [-\exp(2i\delta_l^+) + \exp(2i\delta_l^-)] P_l^1(\cos\theta). \tag{2.30}$$

From Eq. (2.28), cross section I, spin polarization P (directed along the scattering-plane normal $\widehat{\mathbf{n}}$) and asymmetry A (for primary beams fully polarized parallel and antiparallel) are given by [Feder, 1981]

$$\begin{aligned} I(\theta) &= |f(\theta)|^2 + |g(\theta)|^2, \\ P(\theta) = A(\theta) &= \frac{-2\mathbf{Im}[f(\theta)g^*(\theta)|}{I(\theta)}. \end{aligned} \tag{2.31}$$

The number of l, which is needed for convergence (in Eqs. 2.26, 2.29 and 2.30) increases with energy and with atomic number. It typically ranges between 4 and 7 for kinetic energies below 100 eV [Feder, 1985].

2.4.2 Intra – and interlayer scattering

The best way to treat intralayer multiple scattering is to use a "layer-KKR" method, i.e. a two-dimensional version of the Green function band structure method, which was introduced by Korringa [Korringa, 1947] and Kohn and Rostoker [Kohn and Rostoker, 1954]. A characteristic feature of this method is the use of multiple scattering theory for solving the Schrödinger equation. It helps to split the problem into two parts. First, one solves the single scattering problem, mentioned above, presented by a single potential in free space. Second, one solves the multiple scattering problem, which composes the incident wave to each potential from the sum of the outgoing waves from all other scattering centers. As a result we get a beautiful separation between potential and structural properties being characteristic for the KKR method. Another characteristic feature of the KKR method is that it does not rely on a finite basis set for the expansion of the wave functions as practically all other methods of electronic structure calculations do. The choice of the basis functions usually completely characterizes each method and is the decisive factor for the successes and limitations of the method. In the KKR method one solves the radial Schrödinger equation for each site exactly, which in a sense may be interpreted as using a size-, angular momenta- and energy-adapted basis set, which is optimally small.

According to [Feder, 1985] and taking into account the total angular momentum together with plane wave representation, the wave field incident from both sides on a single layer (chosen in the (x, y) plane centered at $z = 0$) (see Fig. 2.6) is

$$\sum_{g\sigma} u_g^\sigma \exp(i\mathbf{k}_g^\sigma \cdot \mathbf{r}) \text{ with } \mathbf{k}_g^\sigma = \left(\mathbf{k}_g^\parallel, \sigma[2(E+V_0) + (\mathbf{k}_g^\parallel)^2]^{1/2}\right), \tag{2.32}$$

where $\sigma = +(-)$ for $z < 0$ (> 0) and g corresponds to the surface reciprocal lattice vectors. The two small components of a four-spinor are of the order of $(E+V)/mc^2$ and may therefore be neglected for low-energy electrons in the interstitial region. Thus the spinors u_g^σ in Eq. (2.32) can be restricted to the two large components u_{gs}^σ, with $s = +(-)$ corresponding to spin up (down). Therefore, intralayer scattering is treated using the total angular momentum representation, explained above for single-site scattering. Expansion of Eq. (2.32) with respect to $j_l(kr)\chi_k^\mu(\mathbf{r})$, where χ_k^μ are the spin angular functions (Eq. (2.23)) and j_l the spherical Bessel functions, yields the total incident amplitude obtained in terms of "direct" incident amplitudes (onto each atom) $A_{k\mu}^{(0)}$ and multiple scattering matrix element $\underset{\approx}{X}$ (see Eqs. (41)-(43) in [Feder, 1985]) as

$$A_{k\mu} = \sum_{k'\mu'} A_{k'\mu'}^{(0)} (1 - \underset{\approx}{X})_{k'\mu' k\mu}^{-1}. \tag{2.33}$$

Thus, scattered-wave two-spinors expressed by the incident-wave, unscattered plane waves and the S-matrix, which transforms the ingoing into the total outgoing field (see Fig. 2.6) as

$$v_{gs}^\sigma = \sum_{\sigma'=\pm} \sum_{g'} \sum_{s'} M_{gg'ss'}^{\sigma\sigma'} u_{g's'}^{\sigma'}, \tag{2.34}$$

with the S-matrix element given as

$$\begin{aligned} M_{gg'ss'}^{\sigma\sigma'} = \delta_{gg'ss'}^{\sigma\sigma'} + (8\pi^2)/(kAk_g^+) \sum_{k\mu} \sum_{k''\mu''} t_{k''\mu''k\mu} \times \\ \times C\left(l''\frac{1}{2}j''; \mu'', s\right) i^{-l''} Y_{l''}^{\mu''-s}\left(\widehat{\mathbf{k}}_g^\sigma\right) \times \\ \times \sum_{k'\mu'} i^{l'} C\left(l'\frac{1}{2}j'; \mu' s'\right) \left[Y_{l'}^{\mu'-s'}(\widehat{\mathbf{k}}_g^{\sigma'})\right]^* (1 - \underset{\approx}{X})_{k'\mu' k\mu}^{-1}, \end{aligned} \tag{2.35}$$

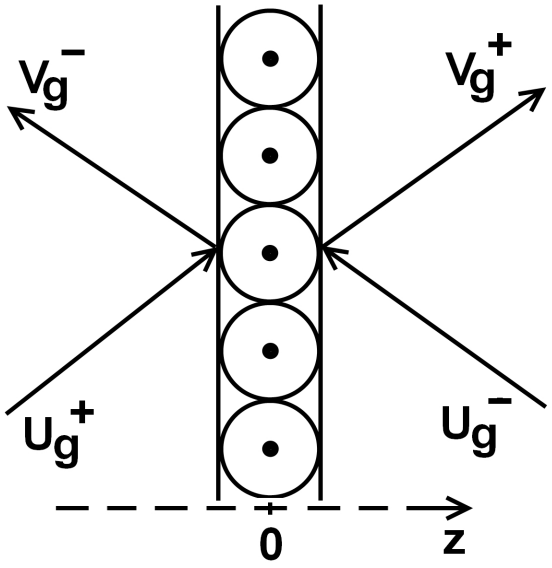

FIGURE 2.6: Scattering of plane-wave field $u_g^{\pm}$ from a single layer of identical crystal atoms (see. Eq. (2.32)). Figure adapted from [Feder, 1985].

where $\delta_{gg's s'}^{\sigma\sigma'}$ is a Kronecker symbol, which is equal to 1 if $\sigma = \sigma'$, $g = g'$ and $s = s'$, otherwise it is equal to 0, A the area of the two-dimensional unit cell. And $\underset{\approx}{X}$ is given by Eqs. 23(b,c) in [Feder et al., 1983].

In order to explain interlayer scattering we can transform the single-layer S-matrix Eq. (2.35) into the $(4N \times 4N)$ "transfer matrix" $\underset{\approx}{Q}$, which relates the plane wave spinor amplitudes (u_g^-, v_g^+) on the $z > 0$ side of the layer to (u_g^+, v_g^-) on the $z < 0$ side. Therefore, in this second stage of treating multiple scattering, the scattering matrices $\underset{\approx}{M}$ (Eq. (2.35)) or transfer matrices $\underset{\approx}{Q}$ of the individual layers plus scattering by a surface potential barrier are combined to yield the S-matrix of the whole system. Then diffraction by a semi-infinite stack of identical layers (i.e. a truncated bulk crystal) accurately provided with corresponding Bloch waves: denoting by u_g^+ and v_g^- the incident and reflected plane-wave spinor amplitudes, respectively, matching of the plane-wave field outside to a linear combination of Bloch waves inside gives the $(2N \times 2N)$ "bulk reflection matrix" $\mathbf{R}^b$ [Feder, 1981]:

$$v_{gs}^- = \sum_{g's'} R_{gg's s'}^b u_{g's'}^+. \tag{2.36}$$

It is quite important to take into account the transition region between vacuum and

bulk, the "selvedge", which usually involves, in addition to the surface potential barrier (see Fig. 2.4), atomic layers which differ from the bulk layers chemically (adsorbates), geometrically (reconstruction with a larger unit cell, relaxation of interlayer spacing for one or several layers) or magnetically (with effective field **B** different from that in the bulk). The transfer matrices $\underset{\approx}{Q}_n$ of the atomic layers (enumerated by $n = 1, \cdots, L$) are obtained using the corresponding scattering matrices $\underset{\approx}{M}_n$, which are calculated according to Eq. (2.35).

The surface barrier has the two-dimensional periodicity of the topmost atomic layer and can be Fourier-expanded as $\sum_g V_g(z)\exp(igr)$. Substituting this and $\sum_g \psi_g(z)\exp(i\mathbf{k}_g\mathbf{r})$ into the Dirac or Schrödinger equation, one obtains a set of coupled ordinary differential equations for the $\psi_g(z)$, and integrating them numerically gives the barrier matrices $\underset{\approx}{M}_0$ and $\underset{\approx}{Q}_0$. Neglecting the "corrugation" of the barrier, i.e. only $V_{oo}(z) =: V(z)$ retained, the differential equations are decoupled, and $\underset{\approx}{M}_0$ and $\underset{\approx}{Q}_0$ are diagonal in g. Whether barrier corrugation may actually be disregarded or not, depends, for barrier-sensitive observable features, on whether these are significantly influenced by the near-surface part of the barrier. For example, LEED fine structure features are determined by the image asymptotic behavior and can therefore be described by one-dimensional surface barrier models, importance and examples of them will be explained below in the context of the 2D reflectivity and asymmetry landscapes.

Scattering by the entire selvedge (surface barrier plus special near-surface atomic layers) is described by the product matrix $\underset{\approx}{Q} = \underset{\approx}{Q}_0 \times \underset{\approx}{Q}_1 \times \ldots \times \underset{\approx}{Q}_L$. Partitioning $\underset{\approx}{Q}$ into four $(2N \times 2N)$ submatrices $\underset{\approx}{Q}^{\sigma\sigma'}$, where (σ, σ') are the propagation direction indices (cf. Eqs. (2.32) and (2.34)), and combining these via simple matrix algebra with the $(2N \times 2N)$ bulk reflection matrix $\underset{\approx}{R}^b$ (Eq. (2.36)), one obtains the reflection matrix $\underset{\approx}{R}$ for the complete system [Feder, 1985].

2.4.3 Full potential KKR method

All-electron methods based on a spherical potential of muffin-tin type or on the atomic sphere approximation have in general proven to be very successful and efficient for the description of the electronic structure of solids. However, systems with lower symmetry and/or open structures require a more accurate treatment going beyond the spherical approximation. This is also necessary, if forces and lattice relaxations are calculated, since for these problems the spherical approximation fails completely. The KKR method can be extended into an accurate and efficient full potential method, fulfilling all desired requirements for successful electronic structure calculations.

As we could see from theoretical approaches used above, calculating eigenfunctions and eigenvalues and single-particle energies represents the central problem in the density functional calculations. However, such a calculations can be avoided, if instead the single-particle Green function of the Kohn-Sham equation is determined. This quantity, which is the solution of the Schrödinger equation, contains all the information about the ground state, in particular the charge density and the local density of states can be directly calculated from the Green function.

Expanding the fundamental equation for KKR-Green function into spherical harmonics as a function of r and r', for non-overlapping and space-filling cells centered at position R_n, where the electrons are scattered by potential v_n [Zeller, 1987]

$$G(r+R^n, r'+R^n; E) = \delta_{nn'}\sqrt{E}\sum_L H_L^n(r;E)R_L^n(r;E) + \\ + \sum_{LL'} R_L^n(r;E)G_{LL'}^{nn'}(E)R_{L'}^{n'}(r';E), \tag{2.37}$$

where the radial solutions $R_L^n(r;E)$ and $H_L^n(r;E)$ represent the single-site problem. And the matrix $G_{LL'}^{nn'}(E)$, the so-called structural Green function, describes the connection of the solutions in the different cells on the sites n and n', with $L = (l, m)$ representing the orbital angular momentum and magnetic quantum

numbers, thus it contains all information about multiple scattering problem [Drittler et al., 1991]:

$$G_{LL'}^{nn'}(E) = g_{LL'}^{nn'}(E) + \sum_{n'L''} g_{LL''}^{nn''}(E) t_l^{n''}(E) G_{L''L'}^{n''n'}(E), \tag{2.38}$$

where the t-matrix $t_l^{n''}$ for the potential $v^n(r)$ is given by

$$t_l^{n''}(E) = \int_0^R r^2 dr j_l(\sqrt{E}r) v^n(r) R_l^n(r;E). \tag{2.39}$$

For the full potential case the important separation between the single-potential problem and the multiple scattering problem survives fully. The single-site eigenfunctions are now the solutions for the general potential $v^n(r)$ no longer being spherical

$$R_L(r;E) = j_l(\sqrt{E}r) Y_{L'}(r) + \int d^3r' g(r,r';E) v(r') R_L(r';E), \tag{2.40}$$

where $j_{l'}(\sqrt{E}r)Y_{L'}(r)$ is a spherical wave incident on the potential $v(r')$ and $g(r,r';E)$ is the Green function for free space, the index L' refers to the angular momentum of the incoming partial wave. Thus, the single-site eigenfunctions $R_L^n(r;E)$ and $H_L^n(r;E)$, which represent single-site properties, clearly separated from multiple scattering properties $G_{LL'}^{nn'}(E)$ is the main advantage of the KKR method. Using three-dimensional integration and expanding the potential as well as the wave function into spherical harmonics, we obtain coupled radial equations for the double-indexed radial functions $R_{LL'}$ (the following equations are taken from [Papanikolaou et al., 2002] and references therein)

$$R_{LL'}(r;E) = \delta_{LL'} j_{l'}(\sqrt{E}r) + \int_0^S dr' r'^2 g_l(r,r';E) \sum_{L''} v_{LL'}(r) R_{L''L'}(r';E). \tag{2.41}$$

Here the first index L refers to the r-coordinate of the outgoing partial wave and the second one L' to the angular momentum of the incoming wave.

Where

$$v_{LL'}(r) = \sum_{L''} C_{LL'L''} v_{L''}(r), \tag{2.42}$$

with $C_{LL'L''} = \int d\Omega Y_L Y_{L'} Y_{L''}$ are the Gaunt coefficients. Solution of integral equation (2.41) comes in the form

$$R_{LL'}(r,E) = \delta_{LL'} \mathring{R}_l(r,E) + \int_0^S dr' r'^2 G_l(r,r';E) \sum_{L''} \Delta v_{LL''}(r) R_{L''L'}(r';E), \tag{2.43}$$

where the effect of the spherical part of the potential is already included in the incident radial wave function $\mathring{R}_l(r,E)$ and $G_l(r,r';E)$ is the l-dependent radial Green function for the spherical component of the potential

$$G_l(r,r';E) = \sqrt{E} \mathring{H}_l(r;E) \mathring{R}_l(r;E), \tag{2.44}$$

and $\Delta v_{LL''}$ the non-spherical component of the potential, providing the coupling between the different angular moments:

$$\Delta v_{LL''}(r) = \sum_{L'' \neq 0} C_{LL'L''} v_{L''}(r). \tag{2.45}$$

For non-spherical potentials everything remains valid, only $R_L(r)$ and $H_L(r)$ have to be replaced by the single-site solutions for the anisotropic potential and multiple scattering. And t-matrix $t_l^n(E)$ has to be replaced by the t-matrix $t_{LL'}^n(E)$ for a general potential $v^n(r)$ being given by

$$t_{LL'}^n(E) = \int_0^S dr' r'^2 j_l(\sqrt{E} r') \sum_{L''} v_{LL''}^n(r') R_{L''L'}^n(r';E). \tag{2.46}$$

Since the Green functions are anyhow L, L'-matrices, the numerical effort in solving the multiple scattering problem is the same for both, the spherical and non-spherical potentials. Therefore, we have only linear scaling of numerical effort with the number N of non-equivalent atoms for full potentials in the KKR method. This advantage is a direct consequence of the multiple scattering character of the KKR method, which means that in typical calculations the full-potential method does

not require a significant increase in computing time [Papanikolaou et al., 2002].

Additionally, in case of a full-potential treatment muffin-tin construction for the charge and potential distribution or atomic sphere approximation have to be replaced by the exact Wigner-Seitz cells, which are non-overlapping and fill the whole space completely. For these purpose a step function $\Theta(r)$, which is 1 inside the Wigner-Seitz polyhedron and zero outside, can be used. Thus, all integrals are convoluted with $\Theta(r)$ which is expanded in spherical harmonics:

$$\Theta(\mathbf{r}) = \sum_{L} \Theta_L(r) Y_L(\mathbf{r}), \tag{2.47}$$

where $\Theta_L(r)$ is an expansion coefficient and can be calculated for polyhedra of an arbitrary shape [Stefanou et al., 1990; Stefanou and Zeller, 1991]. A similar full-potential, spin-polarized, relativistic KKR method for the elemental ferromagnets was presented in [Huhne et al., 1998] as a full-potential extension for the Dirac equation.

2.4.4 FLAPW

Another method for electronic structure calculation, which has no shape approximations to the density or to the potential and includes all electrons, is the full-potential linearized augmented-plane-wave (FLAPW) method [Slater, 1937]. It has no shape approximations to the density or to the potential, and all electrons are included. In this method the core is processed fully relativistically, while a semirelativistic (neglecting spin-orbit interaction) approach is used for the valence electrons. The FLAPW is a plane-wave-based method with basis function consisting from radial functions and their energy derivatives inside the spheres (shape of the nucleus at fixed position), which are matched onto plane waves in the interstitial region with conditions for the value and for the first derivative [Jansen and Freeman, 1984; Weinert et al., 1982; Wimmer et al., 1981].

Using the local spin density approximation to the density functional theory, the solution of such a many-electron problem in a crystal with nuclei at fixed positions

can be obtained via the total energy in terms of the spin densities $n_\sigma(\mathbf{r})$ [Blaha et al., 1990]:

$$E_{tot}[n_\uparrow, n_\downarrow] = T[n_\uparrow, n_\downarrow] + E_{ee}[n_\uparrow, n_\downarrow] + E_{Ne}[n_\uparrow, n_\downarrow] + E_{xc}[n_\uparrow, n_\downarrow] + E_{NN}, \quad (2.48)$$

with E_{NN} being the repulsive Coulomb energy of the fixed nuclei, and the electronic contributions are labeled conventionally as, the electron-electron repulsion – E_{ee}, nuclear-electron attraction – E_{Ne}, and exchange-correlation energies – E_{xc}, respectively. E_{xc} can be written in terms of a local exchange-correlation energy density $\mu_{xc}(n_\uparrow, n_\downarrow)$ as $E_{xc} = \int dr \mu_{xc}(n_\uparrow, n_\downarrow)(n_\uparrow + n_\downarrow)$ and several particular forms can be chosen for μ_{xc} [Connolly, 1977; Hedin and Lundqvist, 1971; Moruzzi et al., 1978; Slater, 1974; von Barth and Hedin, 1972]. Variation of E_{tot} provided by the Kohn-Sham equation (in Rydberg atomic units; the obvious spin-labeling of the potential was omitted)[Kohn and Sham, 1965]

$$\Big[-\nabla^2 + V_{Ne} + V_{ee} + V_{xc} \Big] \chi^\sigma_{ik}(\mathbf{r}) = \varepsilon^\sigma_{ik} \chi^\sigma_{ik}(\mathbf{r}), \quad (2.49)$$

the solution of which is the primary computational task for so called "energy band methods", e.g. the augmented plane wave (APW) scheme presented by J.C. Slater [Alder et al., 1968; Slater, 1937]. It was implemented with a muffin-tin potential, i.e. one that is spherically averaged in non-overlapping spheres centered upon nuclear sites and volume-averaged to a constant in the interstitial region.

Introduction of the orbitals χ_{ik} works as a most effective way to minimize E_{tot} by means of the variational principle. Such orbitals constrained to construct the densities as a sum over occupied orbitals according to [Schwarz and Blaha, 2003]

$$n_\sigma(r) = \sum_{i,k} n^\sigma_{ik} |\chi^\sigma_{ik}(\mathbf{r})|^2. \quad (2.50)$$

Here, the n^σ_{ik} are occupation numbers such that $0 \leq n^\sigma_{ik} \leq 1/\omega_k$, and ω_k is the symmetry-required weight of the point k. In those two distinct regions different basis functions ϕ are defined in the canonical APW:

(i) Inside atomic sphere t of radius R_t, each ϕ is a linear combination of radial functions u_l times spherical harmonics $Y_{lm}(\widehat{\mathbf{r}})$ (the index t is omitted when not needed)

$$\phi(\mathbf{k}_n, \mathbf{r}) = \sum_{l.m} A^n_{lm} u_l(r, E) Y_{lm}(\widehat{\mathbf{r}}), \tag{2.51}$$

where $u_l(r, E)$ is the regular solution of the radial Schrödinger equation for energy E in the spherical potential inside sphere t, obtained by numerical integration on a radial mesh in that sphere, and the coefficients A^n_{lm} are functions of

$$\mathbf{k}_n = \mathbf{k} + \mathbf{K}_n, \tag{2.52}$$

(k is the reduced wave vector in the first Brillouin zone and the K_n are the reciprocal lattice vectors) which are determined by requiring that this basis function matches (in value) the corresponding interstitial region basis function at the sphere boundary.

(ii) In the interstitial region each ϕ is simply a plane wave

$$\phi(\mathbf{k}_n, \mathbf{r}) = \Omega^{-1/2} \exp(i\mathbf{k}_n \mathbf{r}), \tag{2.53}$$

with Ω being the unit-cell volume.

The basis thus defined is energy-dependent because E in Eq. (2.51) must in turn be equal to $\varepsilon^{\sigma}_{ik}$ in Eq. (2.49) for each band i at each k. In fact it is this requirement which in the limit of an infinite expansion in APW's would yield a basis with a continuous radial derivative at each MT boundary. It is easy enough to include the full potential in the interstitial region since the plane wave basis enables matrix elements of a Fourier representation of the full potential. A calculation of this kind was shown readily by [Schlosser and Marcus, 1963].

The LAPW and APW bases differ only within the spherical regions. Thus the LAPW replaces possibility (i) above with:

(i') Inside atomic sphere t of radius R_t, each ϕ is a linear combination of radial functions times spherical harmonics $Y_{lm}(\widehat{r})$ [Blaha et al., 1990],

$$\phi(\mathbf{k}_n, \mathbf{r}) = \sum_{l,m} \Big[A_{lm}(\mathbf{k}_n) u_l(r, E_l) + B_{lm}(\mathbf{k}_n) \dot{u}_l(r, E_l) \Big] Y_{lm}(\widehat{\mathbf{r}}), \tag{2.54}$$

where $u_l(r, E_l)$ is the regular solution of the radial Schrödinger equation for the spherical part of the potential in sphere t, but now for fixed energy E_l. The second set of radial functions, which appears in the LAPW but not the APW, consists of the energy derivatives $\dot{u}_l(r, E_l) = \dfrac{\partial u_l(r, E)}{\partial E}\Big|_{E_l}$. The linearization of the energy dependence of the radial function was realized by a linear combination of these two functions, which are obtained by numerical integration of the radial Schrödinger equation on a radial mesh inside sphere t within the spherical part of the potential. The coefficients A_{lm}, B_{lm} are determined by requiring that this basis function matches the corresponding interstitial region basis function at the sphere boundary in value and in slope.

Region (ii) is treated just as in the original APW method so $\phi(\mathbf{k}_n, \mathbf{r})$ is given by eq. (2.53). The solutions to the KS equation are expanded in this combined basis set in the usual linear fashion

$$\chi^{\sigma}_{ik}(\mathbf{r}) = \sum_{n} c_n(\sigma, i, \mathbf{k}) \phi(k_n, \mathbf{r}), \tag{2.55}$$

and the coefficients c_n are determined by the Rayleigh-Ritz variational principle. The convergence of this basis set is controlled by a cutoff parameter $R_{mt}K_{max} = 6-9$, where R_{mt} is the smallest atomic sphere radius in the unit cell and K_{max} is the magnitude of the largest K_n vector in Eq. (2.55). The critical difference between the LAPW and APW secular equations is that the LAPW secular equation is not energy dependent because the LAPW basis is not. The LAPW basis removes this dependency by fixing E_l then compensating for the resulting loss of variational flexibility by inclusion in the basis of a systematic estimator (to linear order) of the energy dependence, namely $\dot{u}_l$. The adaptive character of the canonical APW is not lost by this procedure.

With an energy-independent basis, the barriers to treatment of the full potential are also removed. In its general form the LAPW method can treat straightforwardly and potential expanded into lattice harmonics (inside each atomic sphere) and as Fourier series (in the interstitial region) in the form

$$V(\mathbf{r}) = \sum_{L,M} V_{LM}(r) Y_{LM}(\hat{\mathbf{r}}), \text{ inside sphere,} \tag{2.56}$$

$$V(\mathbf{r}) = \sum_{k} V(\mathbf{K}) \exp(i\mathbf{K} \cdot \mathbf{r}), \text{ outside sphere,} \tag{2.57}$$

with the spin (charge) densities expanded in the same fashion. Thus no shape approximations are required in general. When implemented in this fashion, which is completely general, the procedure is frequently called a "full-potential LAPW" (F-LAPW) method [Blaha et al., 1990; Wimmer et al., 1981].

2.5 Importance of surface barrier

The shape of the potential acting on electrons near a metal surface is a fundamental question that has long attracted theoretical interest. It has a width in the order of the lattice constant of the crystal. The surface barrier determines electron transfer processes through conductive surfaces for electrons with kinetic energies below 50 eV. Additionally, the surface barrier is essential for the interpretation of data from electron spectroscopies such as direct and inverse photoemission and low-energy electron diffraction (LEED). At large distances z from the crystal surface it exhibits the Coulomb-like $V(z) = 1/(4(z - z_0))$ image potential and inside the crystal we find a constant inner potential V_0. For decreasing distances in the near surface region, the potential is progressively weaker than the image potential and gradually approaches the inner potential of the crystal. In order to determine the shape of the surface-barrier in this transition region one can focus on two following problems [Burgbacher et al., 2013]:

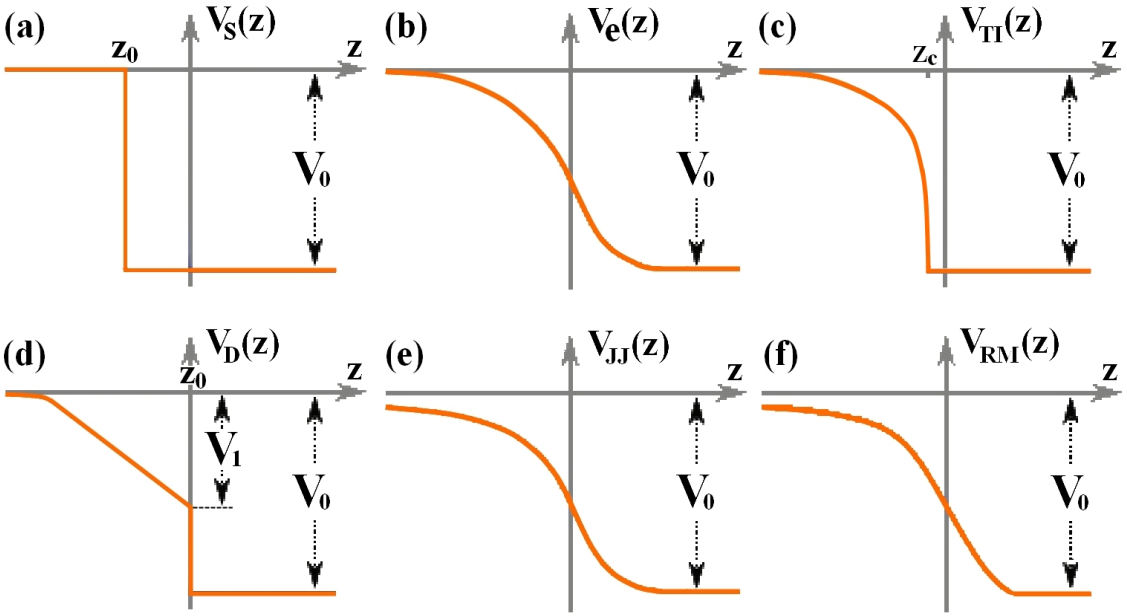

FIGURE 2.7: Surface-barrier models: (a) Step barrier, (b) Exponential barrier, (c) Truncated image potential, (d) Dietz et al.; (e) Jennings-Jones barrier; (f) Rundgren-Malmström barrier.

a) Where is the classical image plane z_0 located relative to the topmost atomic layer?

b) What is the exact shape of the transition region?

Several barrier models have been proposed by [Dietz et al., 1980; Jones et al., 1984; Rundgren and Malmstrom, 1977; Thurgate and Sun, 1995] to ensure a smooth transition between the two different potentials (See Fig. 2.7). They differ in the way in which the transition occurs. The two simplest examples are the step and exponential [see Fig. 2.7(a, b)], which are mathematically convenient but have little physical justification and yield unsatisfactory results in simulation of LEED fine structures, but it is therefore somewhat useful for qualitative analysis. The step potential (Fig. 2.7(a)) has the form

$$V_s(z) = \begin{cases} 0, & \text{if } z \leq z_0 \\ -V_0, & \text{otherwise} \end{cases}, \tag{2.58}$$

where V_0 is the inner potential and z_0 is the image plane location. This simple model is usually used for the identification of effects, which are coming from a realistic surface barrier model during calculations, because it refracts incident beams but does not reflect them at all and commonly it is referred to as a "refracting but non-reflecting" step barrier. Additionally, the step barrier has the wrong asymptotic form and does not predict the existence of Rydberg series of image-potential derived surface states [Jones and Jennings, 1988]. The exponential barrier (see Fig. 2.7(b)) is of the form:

$$V_e(z) = \frac{-V_0}{1 + \exp[-B(z - z_0)]}, \tag{2.59}$$

where B is an arbitrary constant. This model is straightforward to treat analytically, and it provides a rough approximation to result, showing presence of image potential states.

The truncated image potential (Fig. 2.7(c)) attempts to overcome the problem of absence of Rydberg series. The image potential is "cut" by the constant inner potential, which involves a sharp, unrealistic kink at the transition. It is adequate far outside and within the metal, but fails to take into account correctly the electron-electron interactions close to the metal surface:

$$V_{TI}(z) = \begin{cases} 1/4(z - z_0), & z \leq z_c \\ -V_0, & z > z_c \end{cases} \tag{2.60}$$

Surprisingly good agreement with LEED fine-structure measurements was obtained by using a barrier in which a linear interpolation between vacuum and bulk regions is used [Dietz et al., 1980] (Fig. 2.7(d))

$$V_D(z) = \begin{cases} \dfrac{q^2}{2(z - z_0)}, & z < z_1 \\ -V_1 - \dfrac{q^2 z}{2(z_1 - z_0)}, & z_1 < z < 0 \\ -V_0, & z > 0 \end{cases} \tag{2.61}$$

with two adjustable parameters V_1 – being the barrier height at the topmost layer of atoms (z = 0) and z_0 – being the image plane location. It helps to separate clearly barrier scattering effects from spin-dependent and Bragg features.

Modification of this barrier with much better representation of the potential in the transition region than the linear interpolation was done by Jones and Jennings [Jones et al., 1984] (See Fig. 2.7(e)) and given by

$$V_{JJ}(z) = \begin{cases} \dfrac{1}{2(z-z_0)}\Big(1-\exp[\lambda(z-z_0)]\Big), & z < z_0 \\ \dfrac{-V_0}{A\exp[-\beta(z-z_0)]+1}, & z > z_0 \end{cases} \tag{2.62}$$

where the constants A and β are determined by matching V(z) and its derivative at the image plane z=z_0. They are given by

$$\beta = \frac{V_0}{A}, \tag{2.63}$$

$$A = -1 + \frac{2V_0}{\lambda}. \tag{2.64}$$

This model, which is called saturated or *Jennings-Jones barrier*, assumes that the effective potential far from the surface has the classical image form V(z) = 1/4z, but that as soon as the electron approaches the surface it starts to saturate and goes smoothly to a value in the bulk, which is determined by electron-electron interaction.

The *Rundgren-Malmström barrier* [Rundgren and Malmstrom, 1977] shown in Fig. 2.7(f), connects the asymptotic regime $z \leq z_1$ to the bulk muffin-tin zero V_0 by a third-order polynomial in z, spanning the range $z_1 < z < z_2$. The zero of the z scale lies in the outermost layer of atoms. The model potential is assumed to be

$$V_{RM}(z) = \begin{cases} \dfrac{1}{2}(z-z_0)^{-1}, & z \leq z_1 < z_0 \\ s_0 + s_1(z-z_1) + s_2(z-z_1)^2 + s_3(z-z_1)^3, & z_1 < z < z_2 \\ V_0, & z \geq z_2 \end{cases} \tag{2.65}$$

The imaginary part of the barrier potential has been set to zero, avoiding the introduction of additional parameters. The polynomial coefficients s_0, s_1, s_2, and s_3 are fixed through the requirement of continuity and differentiability for $V_{RM}(\mathrm{z})$. Such a smooth surface potential barrier model first of all refracts beams, which are incident from the vacuum and from the bulk crystal side. Then it reflects these beams, with characteristic amplitude reflection coefficients. As a result we have multiple scattering between surface barrier and bulk, which lead to drastic surface resonance fine structures in the intensities and surface barrier effects in LEED.

All of these models are one dimensional barriers, which lead to simplifications and shortcomings. They neglect the three-dimensional effects by not taking into account that the charge density of a real crystal surface is corrugated lateral to the surface. Tamura and Feder [Tamura and Feder, 1986] extended a multiple-scattering theory of low-energy electron diffraction to take into account the three-dimensional nature of the surface potential barrier. The results demonstrate that barrier corrugation has a strong influence on SPLEED spectra from W(001) at energies below about 12 eV and leads to good agreement with experimental data.

Taking into account that the density of states in ferromagnetic surfaces is spin dependent, we will have different interaction of impinged electrons with different spin orientation with the electronic systems of the crystal due to the exchange interaction. That is why for the ferromagnetic surfaces a spin-dependent surface barrier is expected. It was shown by [Braun et al., 2002; Nekovee et al., 1993] that two qualitatively different shapes for the spin-dependent surface-barrier like spin-dependent Rundgren-Malmström type and fully three dimensional potential can be used to explain the experimental data.

In addition to the shape of the surface barrier in the elastic scattering of low-energy electrons from a metal surface a very important role in scattering at the surface barrier is played by the so called *threshold effects*. Together with crystal scattering the barrier scattering can lead to fine structures in very low energy LEED caused by interference between both processes. Several elastic processes contribute to the specularly backscattered intensity, as illustrated in Fig. 2.8:

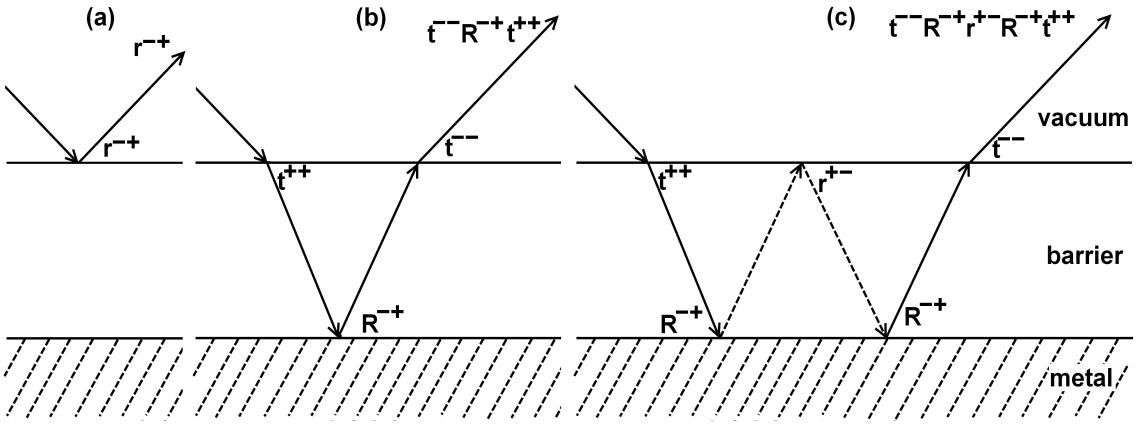

FIGURE 2.8: Mechanism of production of the threshold effect in LEED. Figure adapted from [Jones and Jennings, 1988] and [Burgbacher et al., 2013].

1) The incident electron beam is reflected directly at the barrier (Fig. 2.8(a));

2) The incident electron beam is transmitted through the barrier, reflected at the crystal and further on transmitted through the barrier into vacuum (Fig. 2.8(b));

3) The electron beam, reflected from the crystal, has insufficient energy to cross the surface barrier into vacuum, it will be totally internally reflected back at the barrier. This process can continue until the electron is transmitted into the vacuum as components of the specular and other emergent beams (Fig. 2.8(c)).

The total amplitude reflection matrix of the specularly reflected beam by the crystal is a sum of all these possible processes.

$$R_T^{-+} = r^{-+} + t^{--}R^{-+}t^{++} + t^{--}R^{-+}r^{+-}R^{-+}t^{++} + t^{--}R^{-+}r^{+-}R^{-+}r^{+-}R^{-+}t^{++} + \cdots, \tag{2.66}$$

which may be summed to infinity to yield

$$R_T^{-+} = r^{-+} + t^{--}R^{-+}(1 - r^{+-}R^{-+})^{-1}t^{++}, \tag{2.67}$$

where the crystal fills the half-space $z > 0$ and r^{-+} is the matrix of reflection coefficient for electrons moving along the z-axis in the direction of increasing z which are then scattered by the barrier into the direction of decreasing z. Thus

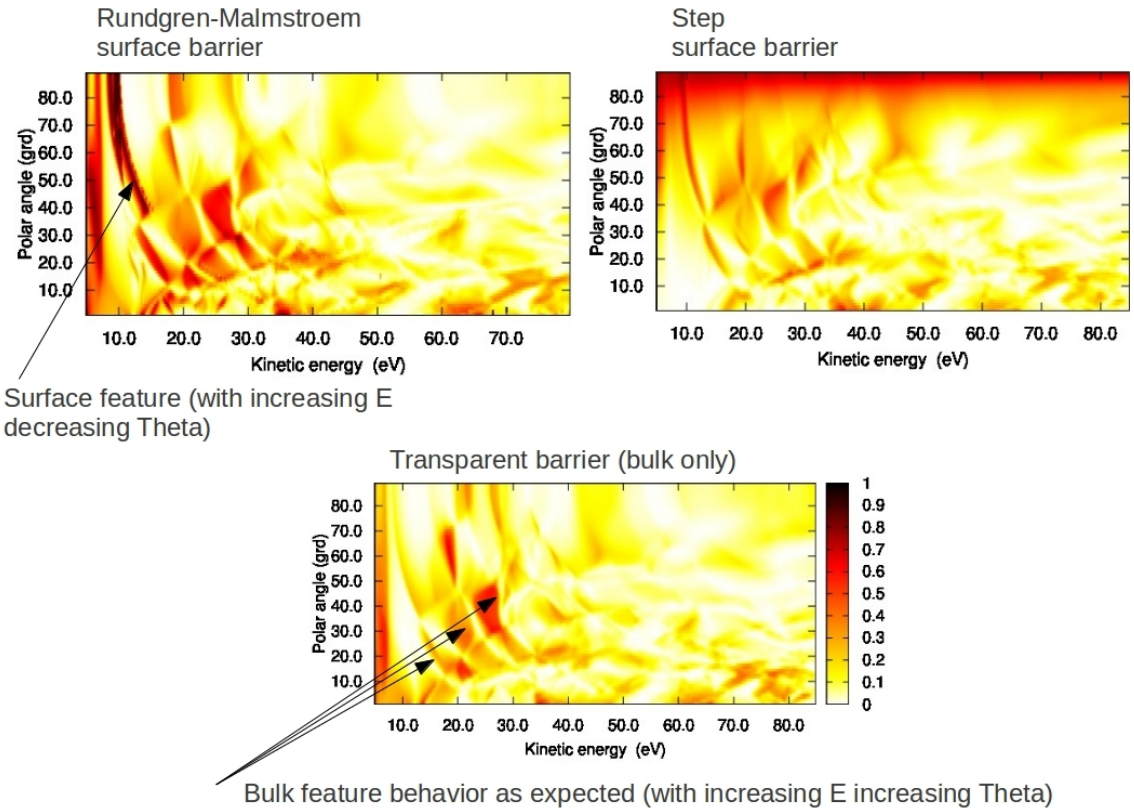

FIGURE 2.9: Reflectivity calculation of E-θ-landscape for Ir(001) crystal for three different surface barriers: Rundgren-Malmström, Step surface barrier and transparent barrier. (courtesy J. Braun and J. Minár)

t^{++} is the transmission matrix for the incoming beams at the barrier, r^{+-} is the internal reflection matrix for the surface barrier and t^{--} is the transmission matrix for the outgoing beams at the barrier. R^{-+} is the reflection coefficient matrix for the crystal substrate [Jones and Jennings, 1988].

The two-beam interference between the primary electron beam and a diffracted, pre-emergent beam is primary cause of the VLEED fine structure and produces the threshold effects [Jones and Jennings, 1988]. Additionally, the analysis of oscillations near thresholds helped to determine that the interference effects play a more important contribution to the LEED profiles than the surface resonance state [Bosse et al., 1982]. The main properties of fine structures have the following characteristics [Jones and Jennings, 1988]:

1) The fine structures peak are an order of magnitude narrower than the prominent

Bragg peaks. They are clearly visible at very low energies and washed out as the energy increases.

2) The series of peaks converge below on the emergence threshold (E_0) for a new diffracted beam. The width Γ_n and peak position $E(n)$ are approximately given by $E(n) = E_0 - \frac{1}{(n+2)^2}$ and $\Gamma_n = \frac{1}{(n-b)^3}$ with a and b depending on the crystal surface and diffraction conditions, $n = 1, 2, 3, \ldots, \infty$. This Rydberg-like series is attributed to the Coulombic part of the surface barrier.

3) Surface roughness reduces the intensity of threshold features relative to the Bragg reflexes.

4) Close to symmetry points on highly symmetric surfaces band structure effects were found, and probably belong to narrow gaps in the band structure near these points.

Taking into account all above-mentioned features of fine structures and surface barrier shapes, which play a prominent role in low-energy electron scattering, we can compare the asymmetry features for three different shapes of one-dimensional surface barriers. These calculations were done by J. Minár and J. Braun using the relativistic layer KKR formalism, based on the multiple scattering theory. The results are shown in Fig. 2.9.

The structure of the Rydberg-like series depends to a large extent on the shape of the surface potential barrier in the vicinity of the first atomic plane. The Rungren-Malmström barrier (top left panel), which is one of the widespread and more realistic barrier models, provides clear information about surface features – going down from top left corner to the right (with increasing energy and decreasing polar scattering angle) as well as bulk features – going up from bottom left corner to the right (increasing energy with increasing angle). The latter shown the well-known intensity oscillations known as I-V-curves.

Application of a simple step surface barrier (top right panel), which corresponds to higher surface damping, leads to washing out of almost all features, so that surface and bulk peaks are no longer resolved as the energy increases.

The transparent barrier (bottom panel) reveals only the bulk features. In this case we assumed that $t^{++} = t^{--} = 1$ and $t^{+-} = t^{-+} = 0$. Thus we have full transmission between barrier and bulk and no reflection between barrier and bulk. This is the pure bulk situation, which is clearly visible in the low energy range of the calculation.

Chapter 3

Imaging spin-filter for electrons based on specular reflection from W(001)

3.1 Description of variable-angle multichannel spin polarimeter

In terms of spin-detector development, a quantity of great interest is defined as the figure of merit (FoM) and is proportional to the inverse square of the statistical error in an electron counting experiment to measure the polarization of an incident beam [Kessler, 1976]. The FoM can be calculated from the square of the total scattering asymmetry multiplied by the reflection coefficient.

The functioning principle is the same for all applications of chapter 3 and 4. It is illustrated in Fig. 3.1 for the idealized case of a perfectly parallel beam specularly diffracted at a single-crystal surface. In this case the image information is "encoded" in the lateral coordinate on the spin-filter crystal. Alternatively, a crossover could be focused on the spin filter. In that case the image information would be encoded in the scattering angle. The Ewald construction in reciprocal

space (right figure) corresponds to specular reflection from W(001) at 45° impact angle. The full and dashed circles denote the Ewald sphere for the high- and low-energy working points (see below), i.e. 26 and 18 eV scattering energy, respectively.

Optimum working points are defined by the extrema in the (single-channel) figure of merit, given by

$$FoM_{single} = S^2 \frac{I}{I_0}, \tag{3.1}$$

depending on the square of the spin sensitivity S (also termed Sherman function [Kessler, 1976]) and reflectivity I/I_0. In addition, the number of simultaneously acquired data points must be large. The relevant statistical quantity for obtaining spin-filtered 2D images is the *two-dimensional figure of merit*

$$FoM_{2D} = N\langle FoM_{single}\rangle, \tag{3.2}$$

where N is the number of data points taken simultaneously and $\langle FoM_{single}\rangle$ is the single-channel figure of merit averaged over the utilized energy and angle interval [Kolbe et al., 2011; Tusche et al., 2011]. We will see in the next section that reflectivity and spin asymmetry vary strongly with scattering energy and angle. Several similar experiments were done up to now, all using specular diffraction from W(001) under 45° angle of incidence. At a scattering energy of 27 eV the asymmetry function reaches its maximum of $S = 0.42$ at a reflectivity of $I/I_0 = 1.3\,\%$, yielding $FoM_{single} = 2 \times 10^{-3}$. In the imaging spin filter behind a PEEM parallel detection of $N = 3800$ data points was achieved, leading to a corresponding 2D figure of merit of $FoM_{2D} = 8$ [Tusche et al., 2011]. Behind a hemispherical energy analyzer about 1000 data points could be acquired simultaneously; this corresponds to a $FoM_{2D} = 1.7$ [Kolbe et al., 2011]. These values are about four orders of magnitude higher than the FoM_{single} value of the classical Mott-detector or SPLEED detector.

The advantage of the multichannel approach has recently been demonstrated in

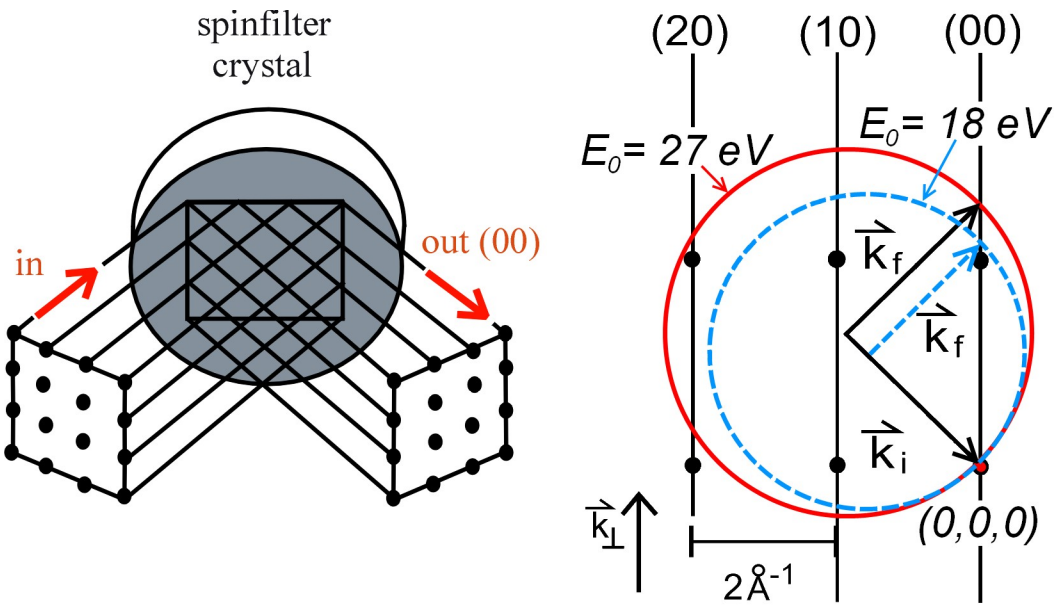

FIGURE 3.1: Functioning scheme of the imaging spin filter in real (left) and reciprocal space (right). The size of the Ewald sphere is determined by the scattering energy, here scaled for the case of W(001) and 27 eV (full circle) and 18 eV scattering energy (dashed circle). k_i and k_f denote the wave vectors of incoming and outgoing beams.

the study of highly reactive surfaces [Kolbe et al., 2012] and the extension to spin-resolved photoemission in the hard X-ray range is on its way (Spin-HAXPES was demonstrated with a single-channel spin detector [Stryganyuk et al., 2012]). Due to the low cross sections in the HAXPES regime, this technique is characterized by notoriously low count rates, demanding for multichannel detection.

It is well known from early SPLEED studies that two classes of single-crystal surfaces can show high spin asymmetries in the specular beam at certain energies. For high-Z targets the spin asymmetry is induced by spin-orbit interaction during the scattering process at the heavy atoms of the crystal as demonstrated for the "classical" system W(001) [Kirschner and Feder, 1979] and several others (Au, Pd, Pt). For ferromagnets the relevant mechanism is the exchange interaction [Bertacco et al., 1998; Hillebrecht et al., 2002; Okuda et al., 2008; Winkelmann et al., 2008].

Early experimental and theoretical works for spin polarized low energy electron diffraction from W(001) [Calvert et al., 1977; Feder, 1976; Kalisvaart et al., 1978;

McRae et al., 1981; O'Neill et al., 1975; Wang et al., 1981], which were carried out at the different energy regions from 10 eV to 200 eV and several fixed scattering angles below 30° and higher than 47° have shown numbers of "hot-regions" where one can expect a highly polarized diffracted beam correlated with intensity maxima, resulting in a favorable figure of merit. However, to the best of our knowledge, no full two-dimensional E-θ-landscapes were measured for initially polarized electrons specularly reflected from W(001); thus calling for a joint experimental and theoretical investigation.

3.2 Experimental setup

A schematic diagram of our experimental setup consisting of polarized electron source and spin detector is outlined in Fig. 3.2. The experiment was carried out in a setup of two ultra-high vacuum (UHV) chambers separated by a small gate valve from each other with the electron beam passing through its center. A self designed and constructed isolation valve was used in order to protect the spin detector during cleaning and activation of the photocathode or vice verse – isolation of the photocathode during oxygen treatment and flashing of the spin filter crystal. The electron source chamber was equipped with a cylindrical mirror analyzer (CMA) and a GaAs-type polarized electron source. It was pumped by an ion getter pump, turbo pump and titanium sublimation pump. The base pressure was 4×10^{-11} mbar or less.

Good UHV conditions were crucial for cleaning, activating and maintaining the GaAs photocathode. As it is well known electrons excited across the direct band gap to the conduction band minimum would be approximately 4 eV below the vacuum level and thus could not escape from the GaAs surface. However, by treating the surface of p-type GaAs with Cs and O_2 it is possible to lower the vacuum level at the surface below the energy of the conduction band minimum in the bulk to achieve the condition known as negative electron affinity (NEA) shown in Fig. 3.3. At this condition the vacuum level E_{vac} is lower than the

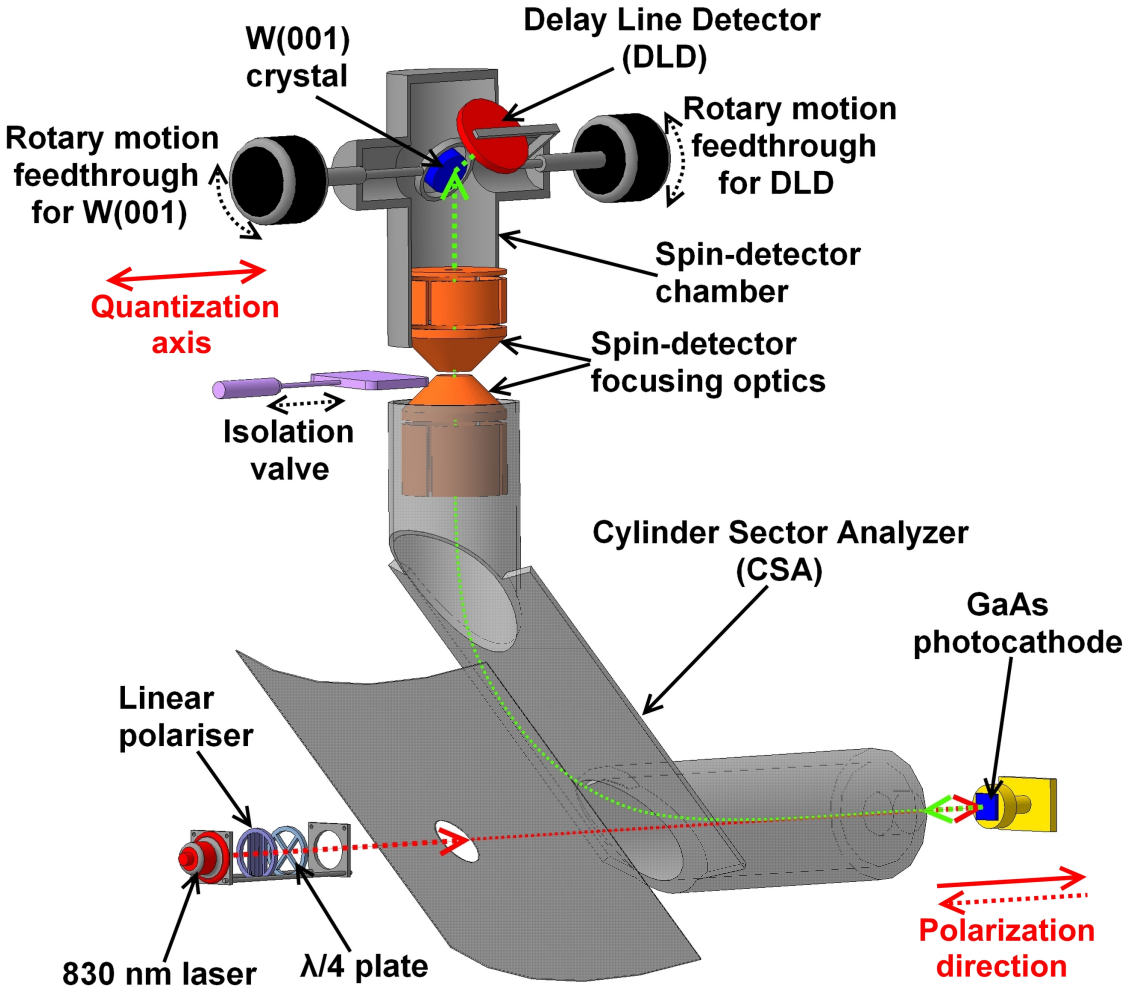

FIGURE 3.2: Experimental setup: source chamber (lower part) containing GaAs source and 90° deflector and spinfilter chamber (upper part) containing the rotating spin-filter mount and delay-line detector are separated by an isolation valve.

conduction-band minimum and thus electron excited across the band gap E_g by photons of energy $\hbar\nu \gtrsim E_g$ thermalize to the conduction-band minimum, diffuse to the surface, and escape into the vacuum. This reduction of the work function (activation of the crystal) is done in three steps:

- The GaAs crystal is heavily p-doped. This results in a band bending at the surface which reduces the electron affinity (see Fig. 3.3(a));
- a cesium layer is applied to the surface of the crystal, in order to reduced the electron affinity even more by the formation of a Cs^+ dipole layer (see

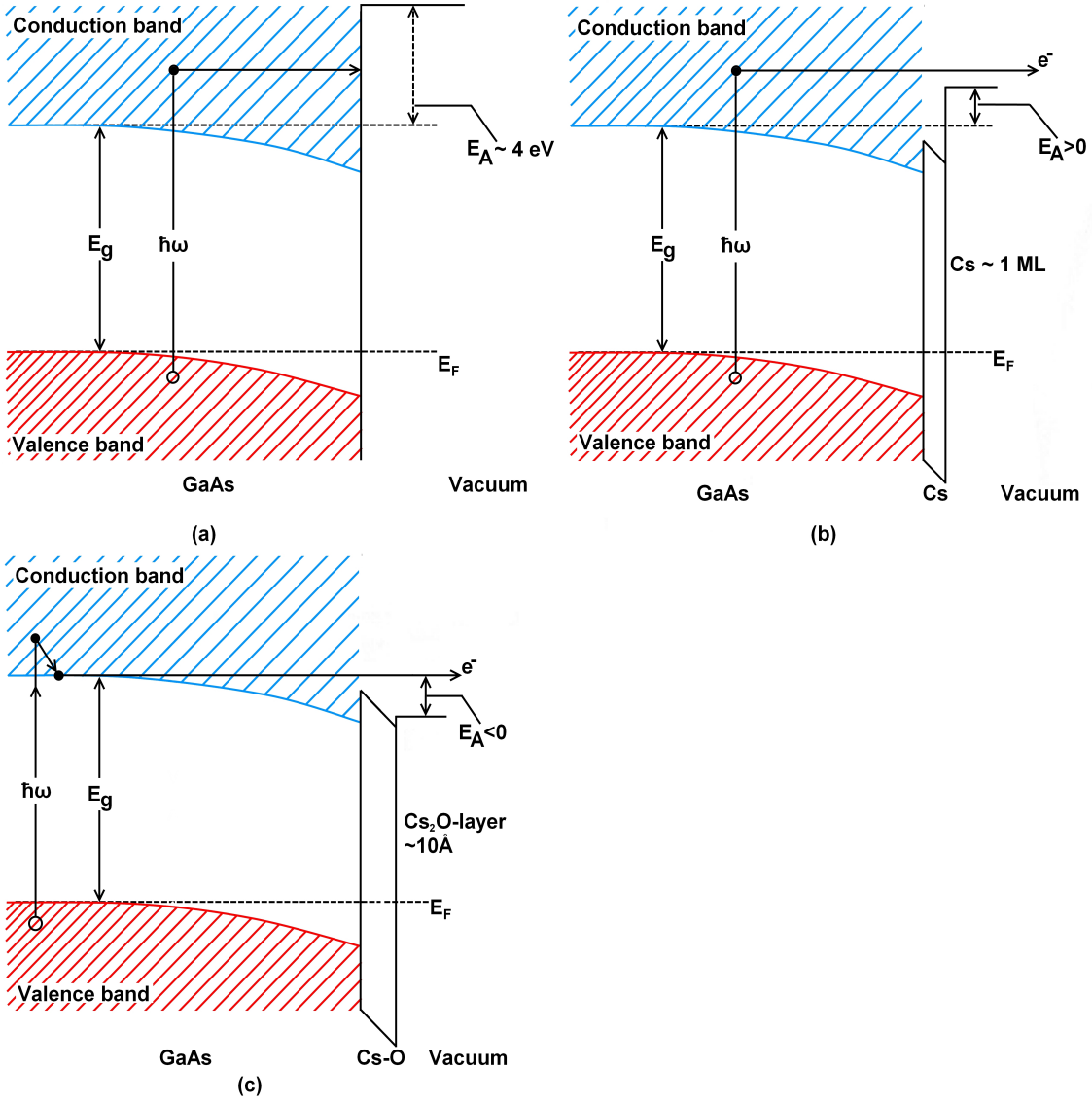

FIGURE 3.3: GaAs surface activated with Cs and O_2 to achieve negative electron affinity. (a) Band bending in p-doped GaAs; (b) lowering of the work-function by adsorption of Cs; (c) additional lowering of vacuum level to NEA regime by growing a Cs-suboxide layer.

Fig. 3.3(b));

- Introduction of oxygen leads to oxidation of the cesium layer. Thus the electron affinity decreases down to negative values. Therefore, the electrons in the conduction band are now able to escape from the surface directly into the vacuum (see Fig. 3.3(c)).

The cathode was cleaned by heating in UHV at $490 - 510°$ C and activated by Cs

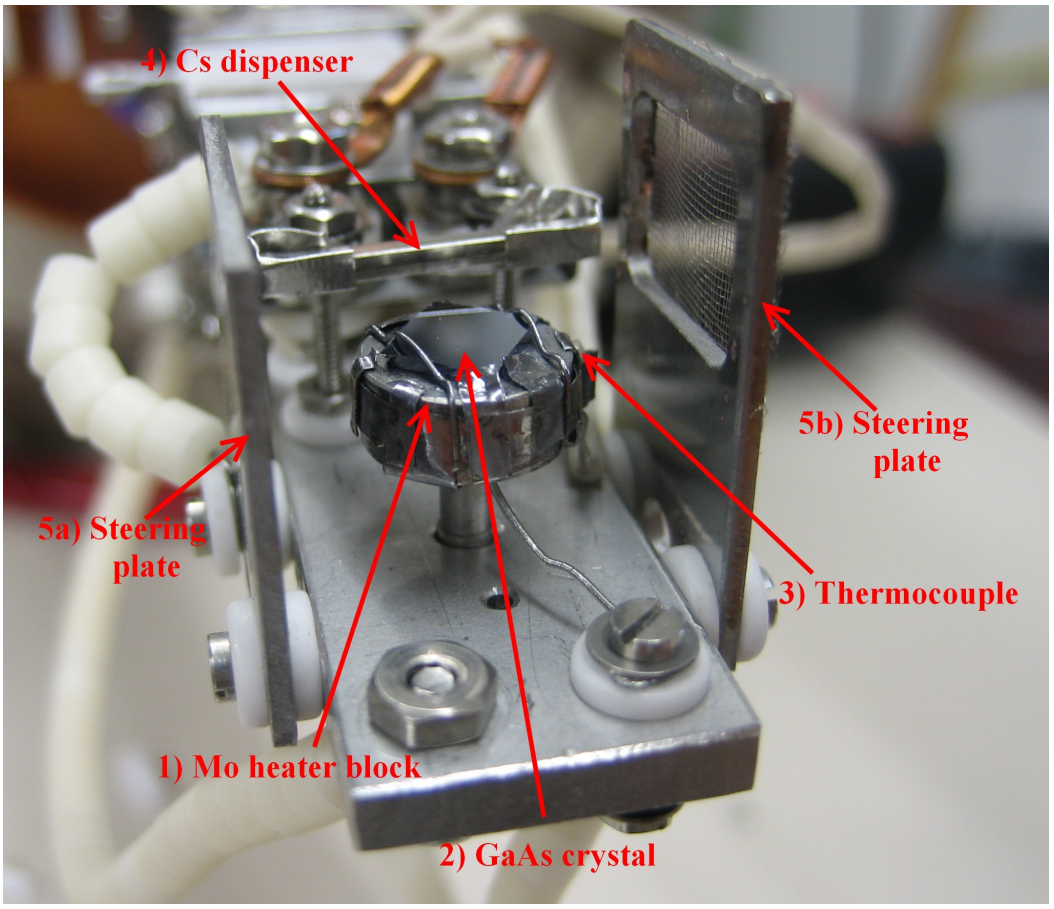

FIGURE 3.4: Photo of the GaAs crystal assembly: 1) Mo heater block; 2) GaAs crystal; 3) thermocouple; 4) Cs dispenser; 5) steering plates.

and O_2 according to the usual "yo-yo procedure" [Pierce et al., 1980]. Heating was done by clamping the GaAs against the Mo heater block which can be radiatively heated by a filament (see Fig. 3.4(1) and (2)). The temperature was monitored by a thermocouple (Fig. 3.4(3)), clamped to the Mo block. The Mo heater block together with GaAs was fixed to a manipulator which has the capability for rotation motions and tilt for positioning the GaAs in front of the spectrometer entrance optics. Additional treatment by an atomic hydrogen beam at about 300° C was applied for deep cleaning of the GaAs crystal from time to time to remove carbon contaminations. The atomic hydrogen beam was produced by feeding hydrogen gas through a tungsten capillary heated by electron bombardment to 2100° C. The temperature of the capillary was measured by a pyrometer. During the cleaning process, the hydrogen flow rate was controlled so that the pressure in the vacuum chamber was maintained at 1×10^{-6} mbar [Akatsu et al., 1999].

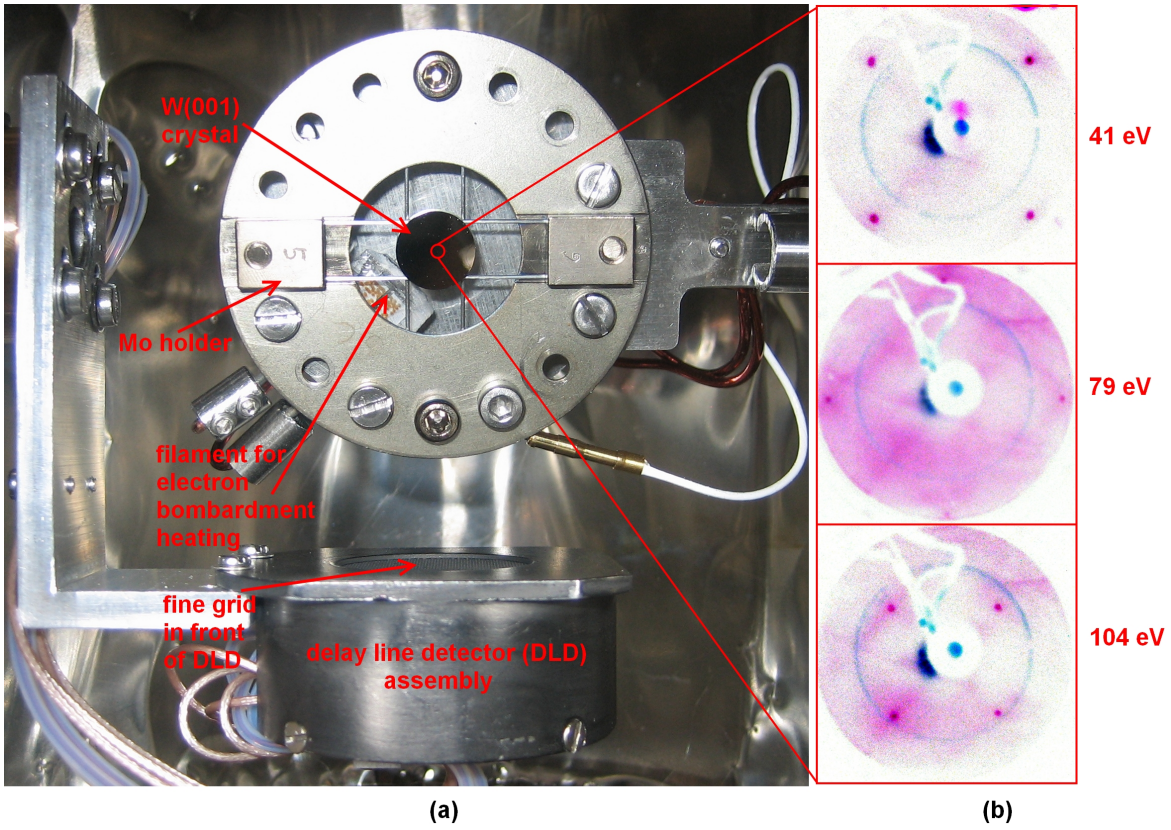

FIGURE 3.5: a) Assembly of spin filtered W(001) crystal and delay line detector (DLD) inside of scattering chamber; b) LEED images of W(001) crystal taken at 41, 79 and 104 eV beam energy.

Spin-polarized electrons were emitted from the GaAs surface, irradiated by circularly polarized light from a laser diode with a photon energy of $h\nu = 1.4$ eV ($\lambda = 830$ nm). Circularly polarized light was generated by using a linear polarizer and a quarter wave retarding element. Perhaps the simplest approach for modulating the polarization was used – a motor driven rotating $\lambda/4$ plate. It turned out that the CsO_x activation layer becomes Cs deficient after a certain period of time. Fortunately, this can be corrected by recesiation and "peaking up" with Cs. The Cs was dosed on the GaAs surface using a SAES cesium dispenser (SAES Getters, CS/NF/3.9/12 FT10+10) shown on Fig. 3.4(4). This was possible to do with the crystal in operating position. The separate Cs dispenser was installed used on top of the spectrometer entrance in order to prevent overheating of the GaAs assembly during activation procedure caused by high current (5.5 – 6 A) flow through the connection electrodes.

The CMA was used for electrostatic deflection of electrons by 90° resulting in a transversely polarized electron beam, which was initially longitudinally polarized. When applying a bias voltage U_{bias} between photocathode and spinfilter crystal the scattering energy with respect to the Fermi level is given by $eU_{bias} + h\nu$, where eU_{bias} denotes the energy difference between the Fermi levels of photocathode and scattering target. Scattering energies are commonly referenced to the vacuum level. Thus, the workfunction Φ_W of the W(001) crystal enters into the equation and we arrive at $E_{scatt}^{vac} = eU_{bias} + h\nu - \Phi_W$. Two additional steering plates (one with fine grid) situated left and right from the GaAs crystal (Fig. 3.4(5a and 5b)) were installed for the alternative case of using a hemispherical electron energy analyzer with 180° deflection instead of the CMA. They were designed as electrostatic micro-deflectors in order to get a transversely polarized electron beam from the GaAs crystal before entering the 180° spectrometer. The data shown below were taken with the CSA.

The scattering chamber has an internal μ-metal shielding and additionally two pairs of Helmholtz coils for compensation of external magnetic fields. Despite of the μ-metal shielding, a residual field existed at the position of the scattering crystal that could not be compensated. Thus, a correction of the scattering angle of up to 9° was necessary, see discussion below. The axis of the residual stray field shows along the rotational axis of the scattering crystal. It was equipped with a W(001) crystal as scattering target and delay-line detector (DLD) (Surface Concept) as single-event detector. The DLD has an active diameter of 25 mm, a spatial resolution of about 50 microns and yields a maximum count rate of 10^7 counts per second. The base pressure in the spin-filter chamber was below 7×10^{-11} mbar. The scattering crystal as well as the DLD was mounted on high-precision rotary motion feedthroughs that allowed changing scattering and detection angles independently.

As the SPLEED process is highly surface sensitive, the spin-filter crystal must be frequently cleaned. Before the spin resolved measurements and installation into the scattering chamber, the W(001) electron mirror was mounted in a LEED apparatus for the initial preparation, cleaning and characterization. It was prepared by many

repeated heating cycles to 1700 K in 5×10^{-8} mbar O_2 atmosphere, and a final high temperature (2200 K) flash removing the oxide layer. This well established procedure is known to lead to clean, carbon free surfaces of W(001) [Zakeri et al., 2010]. During operation, short flashes are necessary in order to desorb adsorbates like CO [Yu et al., 2007]. Additionally, proper azimuthal orientation of spin-filter crystal was done by matching the position of crystal and molybdenum holder with the LEED spots corresponding to the proper crystallographic direction (see Fig. 3.5(b)). It shows the case of azimuthal angle $\phi = 45°$ i.e. the scattering plane intersects the surface plane along the [110] direction.

3.3 E-θ-landscapes

The intensity and spin asymmetry data have been measured as energy spectra at constant scattering angle, with energy steps of 0.5 eV in a range from 12.7 eV to 36.7 eV. The scattering angle was varied in steps of 2° from 30° to 60° with a detailed extra scan at 45° because all previous multichannel detectors used that angle. Thus the experimental E-θ-landscape contains about 800 data points in total. In order to maintain the quality of the W(001) crystal, a high temperature flash is usually the "oxide flash" at 2200 K was performed before each energy scan for each individual angle setting. The dwell time for a single energy point for each polarization was set to 2 s. In order to avoid drift effects, the primary polarization of the electrons from the GaAs source was reversed for every data point via switching the helicity of the circular polarization of the 830 nm laser. Parallel to the measurement, a SPLEED-calculation in relativistic layer-KKR code was carried out by J. Minár and J. Braun (Department Chemie, LMU München) [Ebert et al., 2011].

The position-sensitivity of the DLD was used for the reduction of a contribution of diffusely (quasi-) elastically scattered electrons resulting from scattering at point defects and from electron - phonon interaction. The latter, being stronger for the spin direction that is scattered elastically with lower probability, leads to a reversed

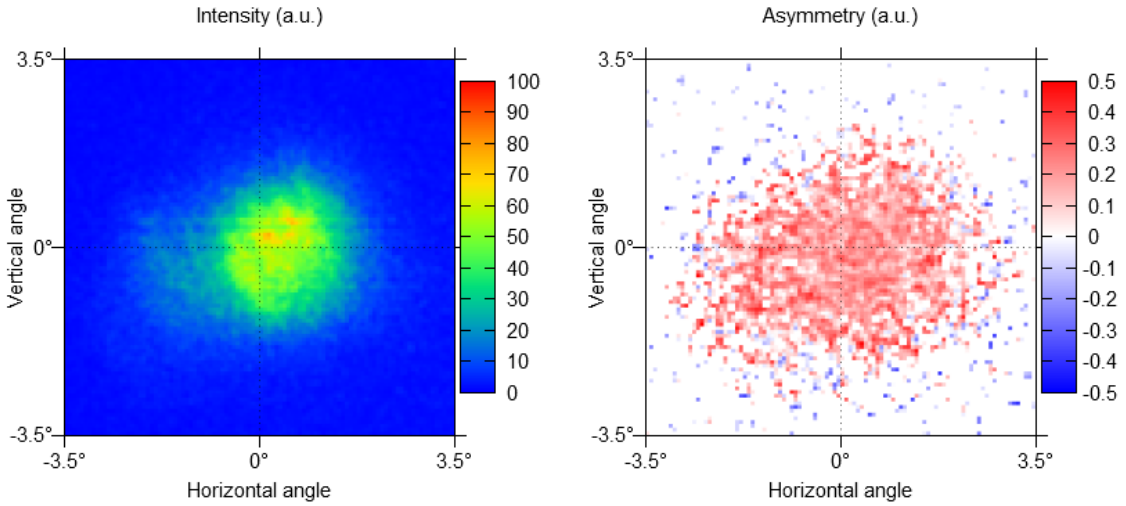

FIGURE 3.6: Total intensity and corresponding asymmetry patterns taken at scattering angle $\theta = 45°$ and scattering energy 26.2 eV. The integral asymmetry in the central area determined according to Eq. 3.3 is $A \approx 17\%$.

sign of the background and thus causes a reduction of the integral asymmetry. In order to suppress such contributions we selected on the DLD a small (7×7 mm) area corresponding to an acceptance angle of ± 2 degree around the diffraction spot for the evaluation of the asymmetry. Samarin et al.[Samarin et al., 2010] also noted that the selection of elastically scattered electrons close to the center of the diffraction spot increases the measured asymmetry of elastic scattering.

As we can see from a typical example of intensity and asymmetry spot profile recorded on the DLD, shown in Fig. 3.6, the inelastic part of the spectrum has very low intensity and the asymmetry changes sign with increasing distance from the center of the spot. Despite the low intensity of the background it may considerably contribute to the asymmetry when it is integrated over a larger area. The intensity at a large distance is caused by inelastic scattering at the W(001) surface with small energy losses of less then 1eV that cannot be discriminated by a retarding grid. The left panel represents the total intensity (sum of the specular beam intensities for two opposite polarization directions) measured at the scattering angle of $\theta = 45°$ and scattering energy of $E = 26.2$ eV, the right panel is the (raw) spin asymmetry determined according to

$$A = \frac{I_\uparrow - I_\downarrow}{I_\uparrow + I_\downarrow}, \tag{3.3}$$

with $I_\uparrow$ and $I_\downarrow$ denoting the specular beam intensities for opposite polarization directions integrated over the selected area. The integrated value of the raw asymmetry from the area around the diffraction spot was determined as $\approx 17\,\%$. Increasing of the detection area to 14×14 mm in a particular energy and angle point leads to a decrease of integrated asymmetry to $< 7\,\%$, whereas decreasing of the detection area to 3.5×3.5 mm or less did not show a significant change in asymmetry. Several isolated dots with extremely large positive and negative asymmetry at larger distance from the center are likely due to statistical error.

Experimental SPLEED results for W(001) as a function of scattering energy and polar angle of incidence are shown in Fig. 3.7. For all measurements the azimuthal angle ϕ was fixed to 0°, i.e. the scattering plane intersects the surface plane along the [010] direction. The E-θ-landscape for the intensity measurements (see Fig. 3.10) represents the sum of two different intensity distributions, measured for opposite polarization directions. A normalization to the intensity distribution without spin-filter crystal I_0 could not be done under the given experimental conditions. Therefore we show the scattering intensities on a relative scale, normalized to their maximum value. The spin sensitivity S (also called Sherman function) is determined from the measured raw asymmetries A (Eq. (3.3)) by normalization to the primary polarization P_0 of the GaAs source, assumed to be $30 \pm 3\,\%$ [Pierce et al., 1980]. Finally, the figure of merit for each image point in an imaging spin filter (FoM_{single}) in Fig. 3.7 was determined according to Eq. (3.1). We assume that $I_0 = const$. The experimental FoM is shown on a relative scale normalized to the maximum. Further, the FoM values are characterized by a larger uncertainty compared to the asymmetry. However, the zeros are correct and the locations of maxima are rather reliable.

Data acquisition and analysis was done with help of a self designed and written LabView code. Controlling of spectrometer voltages and all elements of the spin-detector focusing optics as well as accumulation of count rates from the DLD for each energy point and polarization at fixed scattering angle position was implemented into this code. Look up tables of all voltages were determined and stored

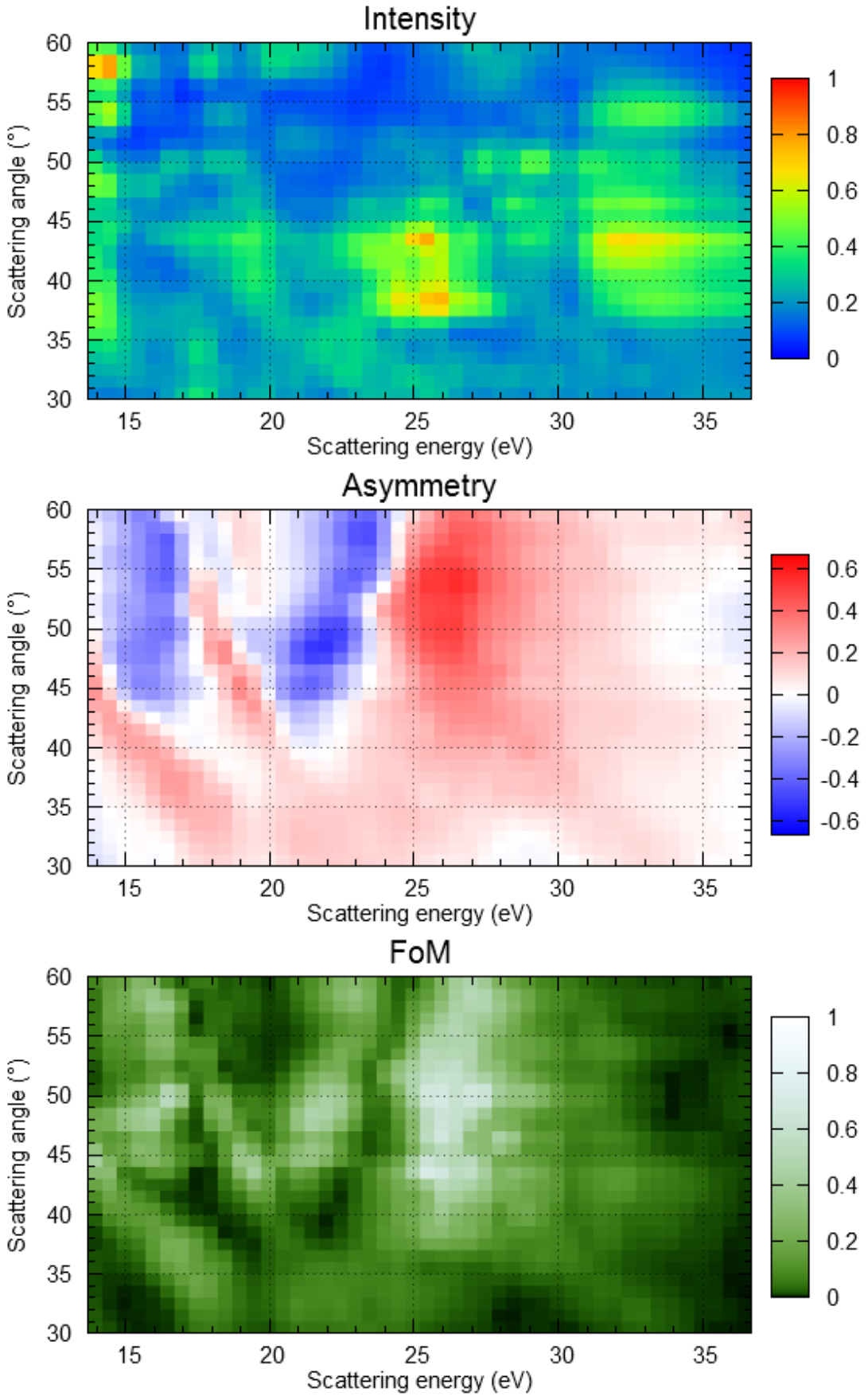

FIGURE 3.7: Specular reflection of spin-polarized electrons from W(001) as a function of scattering energy and polar angle of incidence. From top to bottom: measured intensity I (in relative units, normalized to the maximum), spin-orbit asymmetry S and resulting figure of merit FoM (normalized to the maximum). The scattering plane intersects the surface along the [010] direction.

on the laboratory computer and were used by this code for the energy sweep. Flipping of polarization with help of a motor-driven rotating quarter wave plate also was controlled and changed after dwell time elapsing. Additionally, direct data analysis provided live results for the asymmetry resulting in the line scan for the chosen energy range at a particular analyzed angle.

Our theoretical results for the intensities, spin-orbit induced asymmetries and figures of merit have been obtained by means of fully relativistic VLEED (VSPLEED) calculations [Burgbacher et al., 2013; Ebert et al., 2012], which are based on the layer Korringa-Kohn-Rostoker approach introduced first by Pendry [Pendry, 1974] and later on by Feder [Feder, 1981]. The electronic structure in terms of the single-site scattering t-matrix t is obtained on the basis of a self-consistent SPRKKR calculation [Ebert et al., 2012]. With the t-matrix available, one can define, in a second step, the scattering matrix for a certain layer of the semi-infinite half-space. With this matrix one accounts for all multiple scattering events within the corresponding layer. The multiple scattering between different layers is then accounted for by means of layer-doubling techniques[Pendry, 1974]. As a result of this procedure one ends up with the bulk reflection matrix $\mathbf{R}$, which describes the scattering properties of a semi-infinite stack of layers. As a final step, it remains to include the surface potential barrier treated within the multiple-scattering formalism as an additional layer. A realistic description of the surface potential is given through a Rundgren-Malmström barrier [Malmström and Rundgren, 1980], which connects the asymptotic regime $z < z_A$ to the bulk muffin-tin zero V_{or} by a third order polynomial in z, spanning the range $z_A < z < z_E$. In other words z_E defines the point where the surface region ends and the bulk region starts, while z_I gives the position of the classical image plane. The shape of the image potential is shown in Fig. 3.8. The bulk muffin-tin zero V_{or} is chosen to 17.4 eV for the full energy range; an energy dependence was not explicitly considered. The image plane z_I is located at 0 Å. The polynomial region ranges from about 0.9 Å to -0.9 Å and the distance of the image plane from the center of the first atomic layer is 0.3 of the interlayer spacing in the [001] directionaround 0.2 Å. This means, we have matched this third order polynomial at 0.9 Å to the inner potential of the bulk

and at -0.9 Å to the long-range image potential $1/z$. Therefore, the calculated scattering coefficients of the surface potential are based on the complete potential including the long-ranged image term. The complete computational implementation of this surface barrier for the use in V-SPLEED calculations was done by us recently after it was tested by corresponding numerical simulations on Cu, Fe and Co [Burgbacher et al., 2013]. This way we developed the corresponding computational scheme as a new calculational option in the framework of the Munich SPRKKR program package. This allows us to combine in a homogenous way our self-consistent electronic half-space calculations with model-type surface barriers like the Rundgren-Malmström-potential in the V-SPLEED mode of our computer code. The work function Φ was assumed to be 4.6 eV. It results from our ab-initio formalism, where we are able to handle two dimensional systems for which it is possible two determine the work function via a sum of the Madelung potentials of the atoms located in the so-called interaction zone of the surface system. As it has been shown by Zabloudil et al.[Zabloudil et al., 2005] this results in reasonable values for the theoretical predicted work functions already in the atomic sphere approximation.

The computational results are summarized in Fig. 3.9. They contain more features than experimental date and look rather different, but still show similar to experimental data regions with high asymmetry (negative: $20 < E < 23$ eV and $44° < \theta < 52°$; positive: $24 < E < 27$ eV and $45° < \theta < 56°$) which are slightly shifted to higher energies as well as regions with high FoM, which are present in both data sets.

Looking for possible explanation of the discrepancies between experimental data and theoretical calculations we consider an error in the θ-scale. Because the geometrical angle of the crystal and the DLD were set by a high precision motion feed-through with an accuracy of $< 1°$, a geometric error can be excluded. An error in the θ-scale can be caused by external magnetic fields, leading to energy-dependent deflection and thus a systematic angular error. We tried to suppress magnetic fields in the vicinity of the scattering crystal by using Helmholtz coils

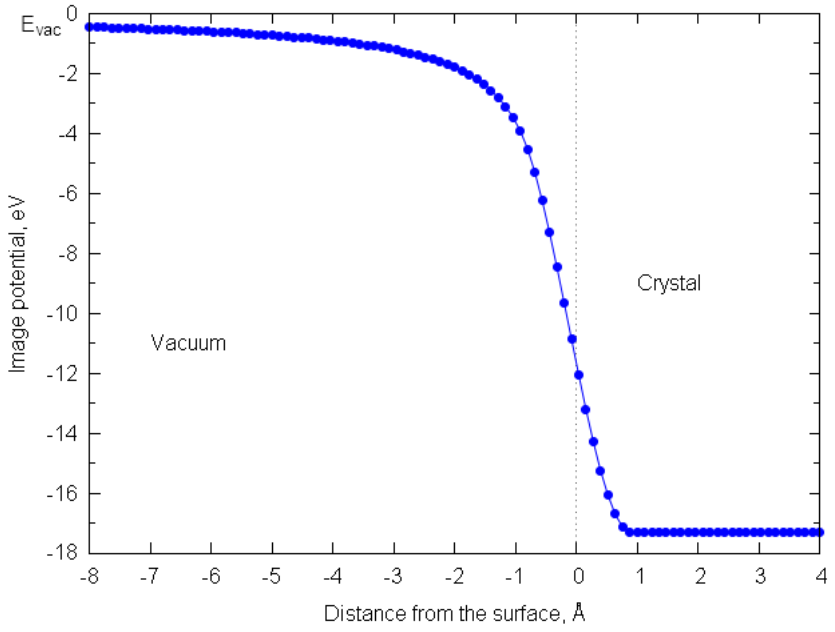

FIGURE 3.8: Surface potential used by [Braun et al., 2013] for the calculations shown in this chapter.

installed close to the scattering chamber. But the compensation does not cancel magnetic field completely. Magnetic fields bend the electron beam in such a way that it impinges onto the crystal under a different scattering angle than the geometrical angle.

We compared our experimental data measured at different scattering angles with the spin asymmetry profile at 45° reported by Tusche et al.[Tusche et al., 2013, 2011]. In particular, as an indicator we used the asymmetry maximum at 45° and 17 eV taken from work done by Tusche et al.[Tusche et al., 2011]. The true scattering angle θ can be determined by adding a field-dependent correction angle θ_{corr} to the measured angle θ_{meas}, $\theta = \theta_{corr} + \theta_{meas}$. θ_{corr} results from the field dependent deflection according to

$$\tan\theta_{corr} = \frac{x}{\sqrt{\frac{2m}{e^2}\frac{E^{vac}_{scatt}}{B^2} - x^2}}, \tag{3.4}$$

with x denoting distance from the last lens element to the scattering crystal, E^{vac}_{scatt} is the kinetic energy of electrons scattered from the crystal, m and e denote

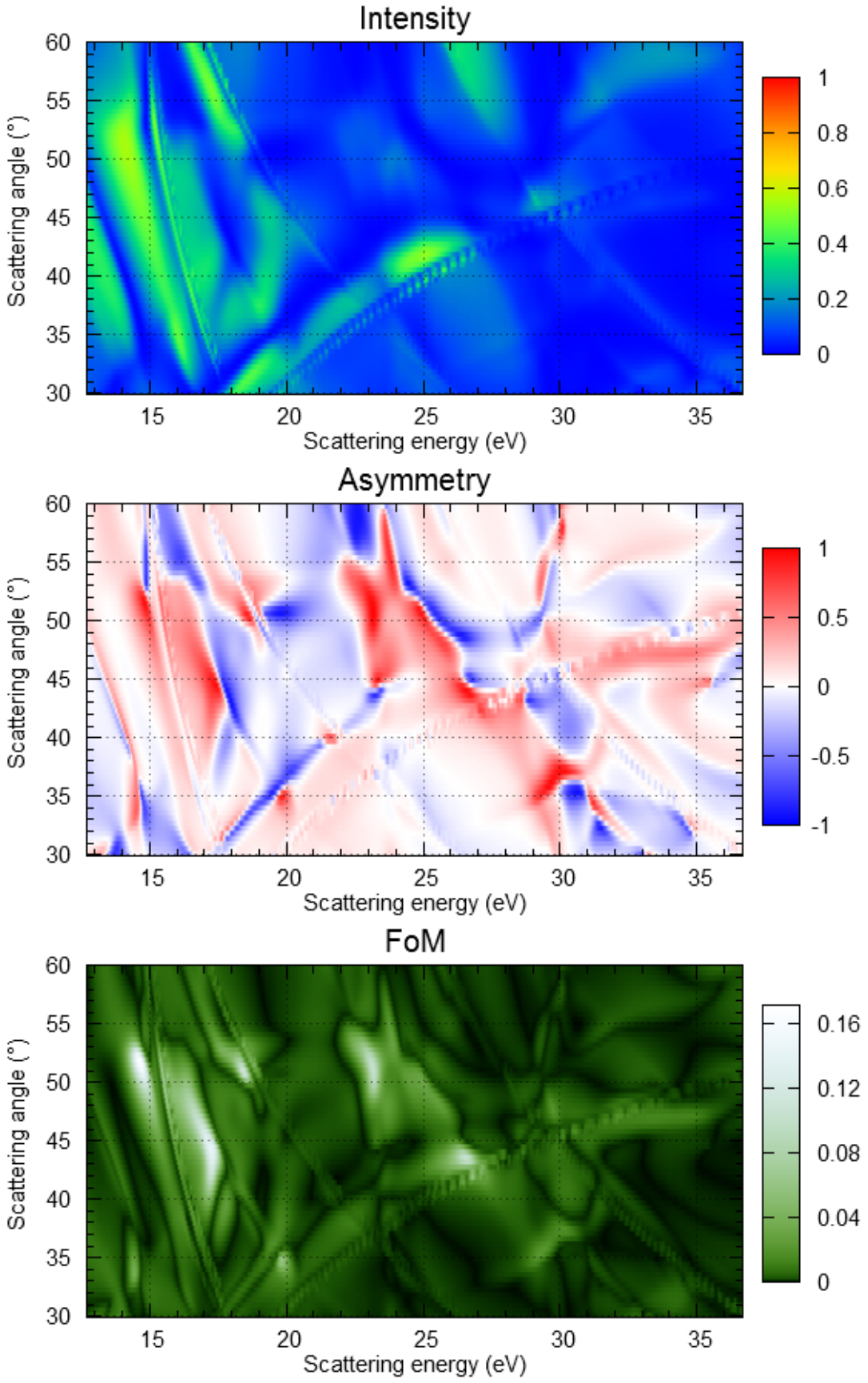

FIGURE 3.9: Specular reflection of spin-polarized electrons from W(001) as a function of scattering energy and polar angle of incidence. From top to bottom (calculated by the relativistic layer-KKR SPLEED code): intensity I, spin-orbit asymmetry S and resulting figure of merit FoM (all on absolute scale). The scattering plane intersects the surface along the [010] direction.

the electron mass and charge. B is the magnetic field and the only adjustable parameter. Thus we obtain a variation of the angular scale from 0° above 27.7 eV to 10° at 13.7 eV. This energy dependent deflection corresponds to a magnetic field of 0.5 Oe, which is on the same order of magnitude as the earth magnetic field.

Additionally, in order to get more realistic and physical model of theoretical calculations we implemented appropriate values for energy broadening (damping) and surface relaxation into theory. The comparison of experiment with corrected angular scale and broadening is plotted in Figs. 3.10, 3.11, 3.12. we used the same method as described above and surface barrier as shown in Fig. 3.8, but the energy-dependent broadening of the final state was strongly increased. The relaxation parameters for our self-consistent electronic structure calculation were taken from work done by Batirev et al.[Batirev et al., 1998]. This theoretical study used the full potential LAPW method, which is suitable for the determination of the minimal total energy of a surface according to lattice relaxations. Thus, the topmost layer shows an inward relaxation of -4.02 % and the subsurface layer an outward relaxation of 3.06 %. The inter-atomic distance parallel to the surface was fixed to $a_W = 3.193$ Å of bulk W, which is larger than the experimental value ($\sim$ 1%). Also according to the theoretical results and their agreement to experimental LEED measurements shown in the paper of Batirev et al.[Batirev et al., 1998] the $c(2 \times 2)$ reconstruction of the two surface layers of W(001) seem to have a minor influence on the spectroscopic properties mentioned in our paper.

The comparison of experimental and theoretical energy-angular landscapes for intensity in Fig. 3.10 still reveals differences. As discussed above this may be explained by a poor control of the incident intensities. Spin-orbit asymmetries are determined for identical conditions of the incident beam by swapping the electron polarization. Therefore, the determination of spin-orbit asymmetries is more reliable.

The experimental and theoretical energy-angular landscapes for the spin-orbit

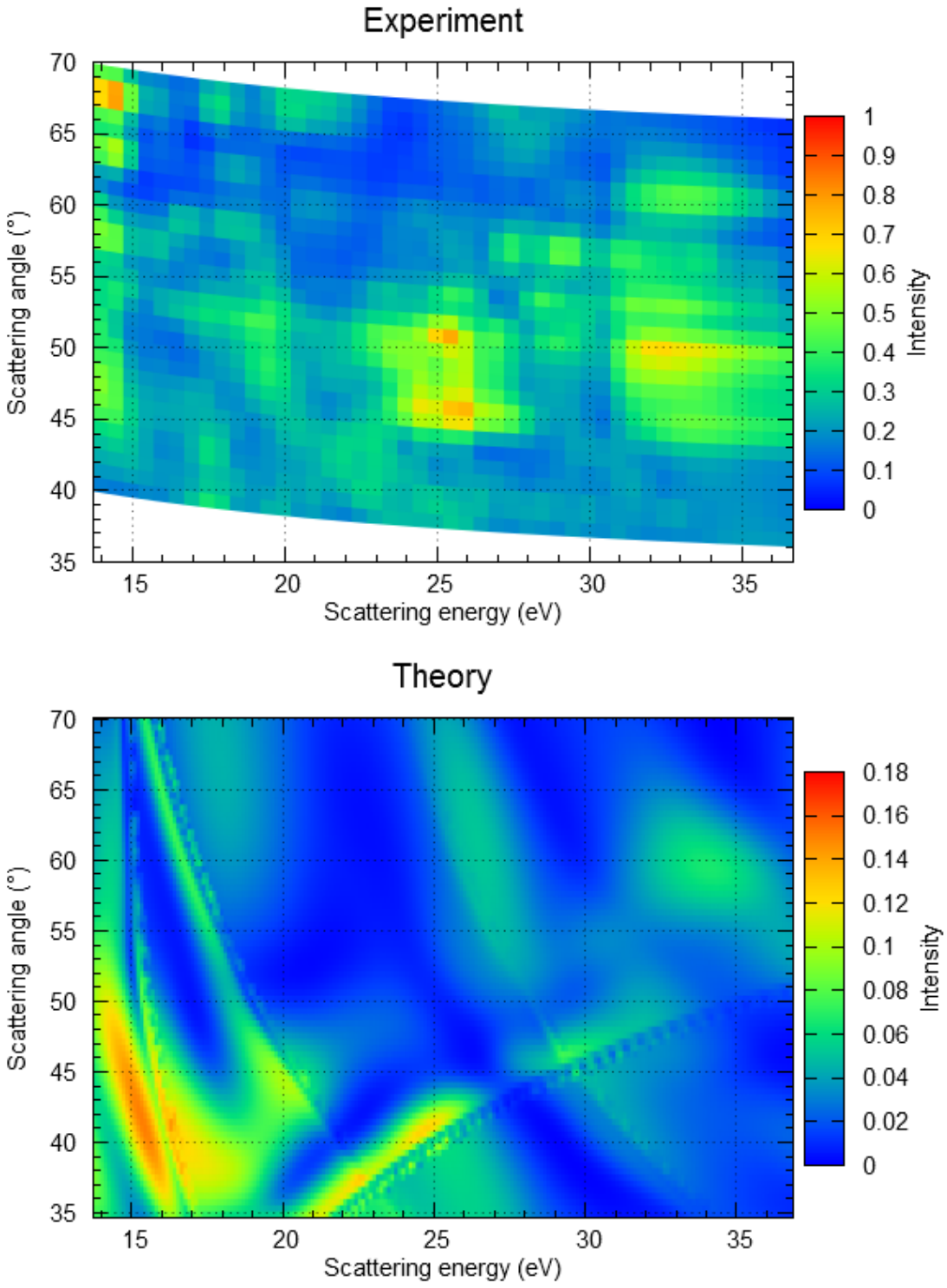

FIGURE 3.10: E-θ-landscape of reflectivity for W(001), experimental (top) and calculated [Braun et al., 2013] by the relativistic layer-KKR SPLEED code (bottom). The scattering plane intersects the surface along the [010] direction.

asymmetry are shown in Fig. 3.11. A bird's eye survey reveals reasonable agreement between experiment and theory concerning the main features and regarding that the experiment smears out fine details (see below). The systematic tilt (increasing energy - decreasing scattering angle) of well pronounced positive and negative features corresponds to surface-barrier induced features. Inspecting these measurements in more detail we can identify several areas with positive (red) and negative(blue) polarization values.

1) $14.0 < E < 18.0$ eV and $53° > \theta > 40°$ (red);

2) $14.5 < E < 17$ eV and $53° < \theta < 68°$ (blue);

3) $18.0 < E < 19.5$ eV and $49° < \theta < 58°$ (red);

4) $20.0 < E < 24.0$ eV and $51° < \theta < 65°$ (blue);

5) $24.5 < E < 28.5$ eV and $45° < \theta < 65°$ (red).

Some of these regions have homogeneous and quite sizable values of asymmetry and are thus suitable for spin-filter purposes. The relative asymmetry values are characterized by statistical uncertainties of approximately 5 % (relative uncertainty). Region **1** has a maximum spin sensitivity value of about $S = +27 \pm 5$ % at 16.7 eV and 46°, whereas region **3** has maximum spin sensitivity value at 18.2 eV and 56° equal to $S = +44 \pm 5$ %. The highest value around $S = +66 \pm 5$ % is observed in region **5** at 26.5 eV and 60°, which is significantly higher than the values reported for 45° working point at 26 eV and 45° or at 27 eV and 45°, which was used in recent spin-filter applications[Kolbe et al., 2011; Tusche et al., 2011] and has a value of $S = +42$ %. All measured values are consistently smaller than the theoretical predictions. Additionally, the theoretical spin-orbit asymmetry landscape is more structured and shows sharper features than the experimental map. For the low energy region, where we can see more structures, the agreement between theory and experiment is apparently better. The reason for that is the larger probing

depth which leads to an increasing inelastic mean free path at low energies. Thus, we have more impact on the relative contribution from deeper-lying layers than

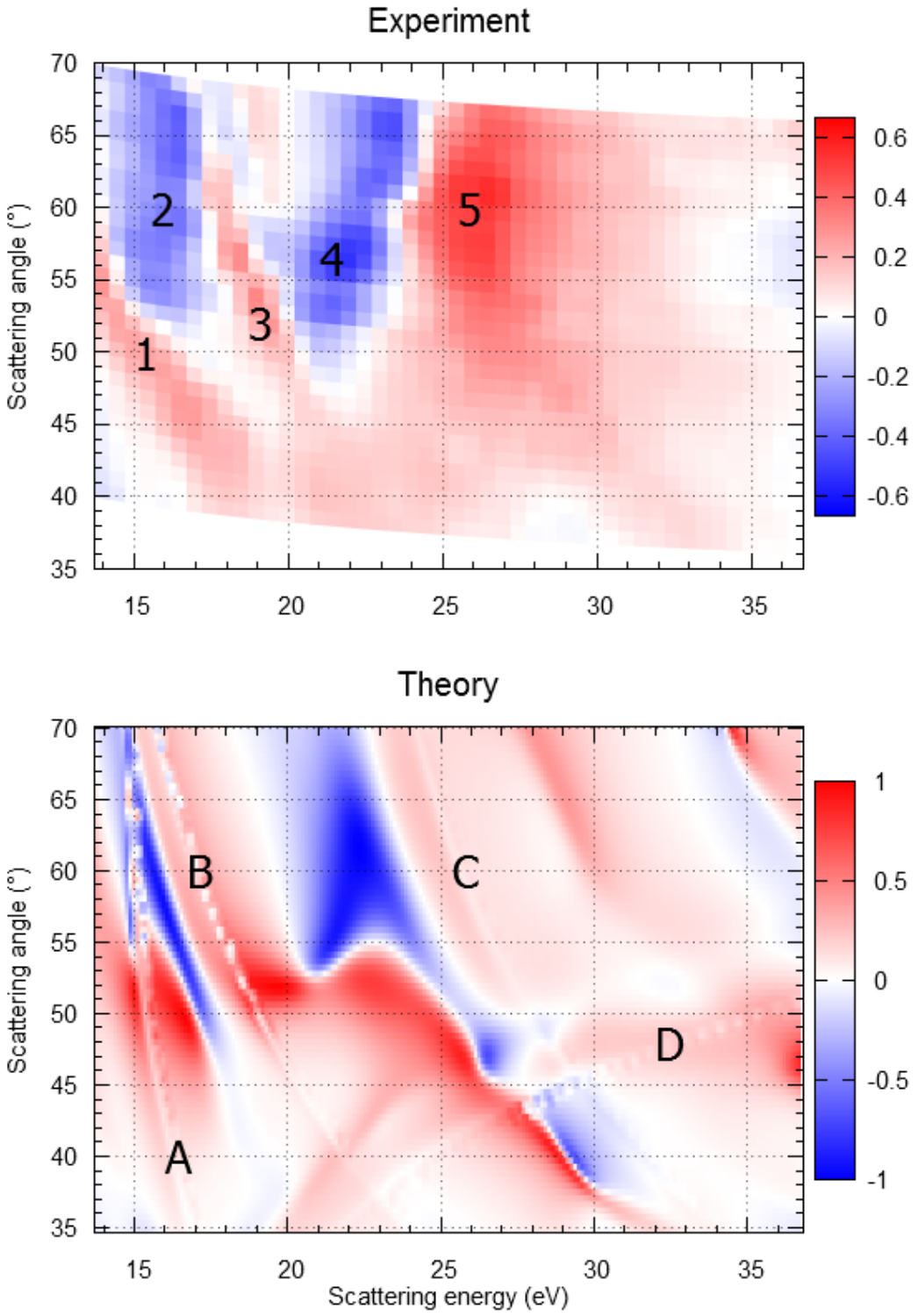

FIGURE 3.11: E-θ-landscape of spin asymmetry for W(001), experimental (top) and calculated by the relativistic layer-KKR SPLEED code (bottom) [Braun et al., 2013]. The experimental false color scales denote the spin-orbit asymmetry according to Eq. 3.3 (b). The statistical uncertainty of the experimental values is 5 %. The scattering plane intersects the surface along the [010] direction. Numbers 1-5 denote pronounced structures that can be identified in experiment and theory. Letters A-D denote sharp characteristic (visible as "dashed lines") structures in the calculation that are not resolved in the experiment.

from the surface regime, which can be affected by residual contamination due to the short "life time" of W(001) in UHV. In the asymmetry (Eq. (3.3)) secondary influences like transport losses or others cancel out, because they act in the same way on $I_\uparrow$ and $I_\downarrow$. However, transport losses vary the reflectivity. Some other possible reasons for the differences between experiment and theory were discussed in a previous paper[Kutnyakhov et al., 2013].

The negative asymmetry region **2** has an average value of about $S = -33 \pm 5\,\%$ with a maximum of $S = -43 \pm 5\,\%$ at 16.7 eV and 58°. Similar to the first positive region **1** it has a relatively narrow usable energy band of about 1 eV FWHM and can be a favorable working point for high-resolution applications. The negative region **4** has an average asymmetry of more than $-50 \pm 5\,\%$ with an extremum of $S = -57 \pm 5\,\%$ at 21.7 eV and 55°. It is adjacent to region **5** with a large positive asymmetry of nearly the same value. This is a favorable feature for switching the asymmetry by a slight variation of the scattering energy. Switching from roughly $-50\,\%$ to $+50\,\%$ can be achieved by varying the scattering energy from 22.2 eV to 26.2 eV. This region is also present in the theoretical asymmetry landscape, but slightly shifted ($\sim$ 1 eV) to lower scattering energies. The 45°-geometry of previous experiments is at the lower end of the favorable region, significantly away from the optimum. The reversing sign of the asymmetry with scattering energy can be used to enhance the performance of the imaging spin filter using the fact that the difference of two images taken at opposite asymmetry values of the spin filter already comprises the spin information. Thus, the procedure described by Tusche et al.[Tusche et al., 2013] allows the determination of spin polarization of samples that cannot be magnetized in two opposite directions as it is the case for Rashba-split surface states or for the complex spin textures in topological insulators.

The fact that experimental features are broadened can have intrinsic and extrinsic reasons. Intrinsic reasons could be incoherent (elastic) scattering or inelastic scattering with small energy losses. Extrinsic reasons are mainly the limitation in energy and angular resolution of the electron beam scattered at the spin-filter

crystal, as well as not sufficient finite lifetime of the electronic states in the theory. Another extrinsic reason is the surface quality of the W(001) crystal.

As it was mentioned above, intensity and FoM E-θ-landscapes bear the additional uncertainty of the missing normalization to the intensity of the incoming beam.

Nevertheless, the asymmetry plays the main role (quadratic function) compared to the intensity (linear function) for the determination of the figure of merit. Furthermore, the zero lines in the FoM are correct. In view of a potential use for spin polarimetry it makes sense to draw attention to four regions with promising experimental values of the FoM, such as **2**, **3**, **4** and **5**. Regions **3** and **5** were confirmed by the calculations but again for slightly lower scattering energies. The weaker appearance of regions **2** and **4** in theory as compared to experiment is probably caused by using non-normalized intensity values for the FoM calculations. Thus, as we can see not only from experimental and theoretical data for the asymmetry but also from the calculated FoM, the tendency to increase the scattering angle from 45° to $50° - 60°$ for better performance of spin-filter detectors is confirmed. Similar results are shown in the papers focused on the imaging spin filter based on Ir(001) [Kutnyakhov et al., 2013] and pseudomorphic Au on Ir(001) [Kirschner et al., 2013]. The availability of different favorable regions allows an optimization of spin detectors for different applications, e.g. as a two-dimensional spin-polarizing mirror in momentum microscopes (narrow ridges with high value of asymmetry, preferably including rapid changes of sign) or as a spin-polarizing mirror behind dispersive electron energy analyzer (broad regions with large energy window and weak energy- and angle-dependence of asymmetry).

Despite the fact that in several regions of interest the measured asymmetry and FoM agree reasonably well with theoretical results, some of the features are washed out in the experimental landscapes. Several of such narrow ridges (appearing as "dashed lines") are marked in the asymmetry plot in Fig. 3.11

A) $15 < E < 17.5$ eV and $70° > \theta > 40°$;

B) $16 < E < 22$ eV and $70° > \theta > 40°$;

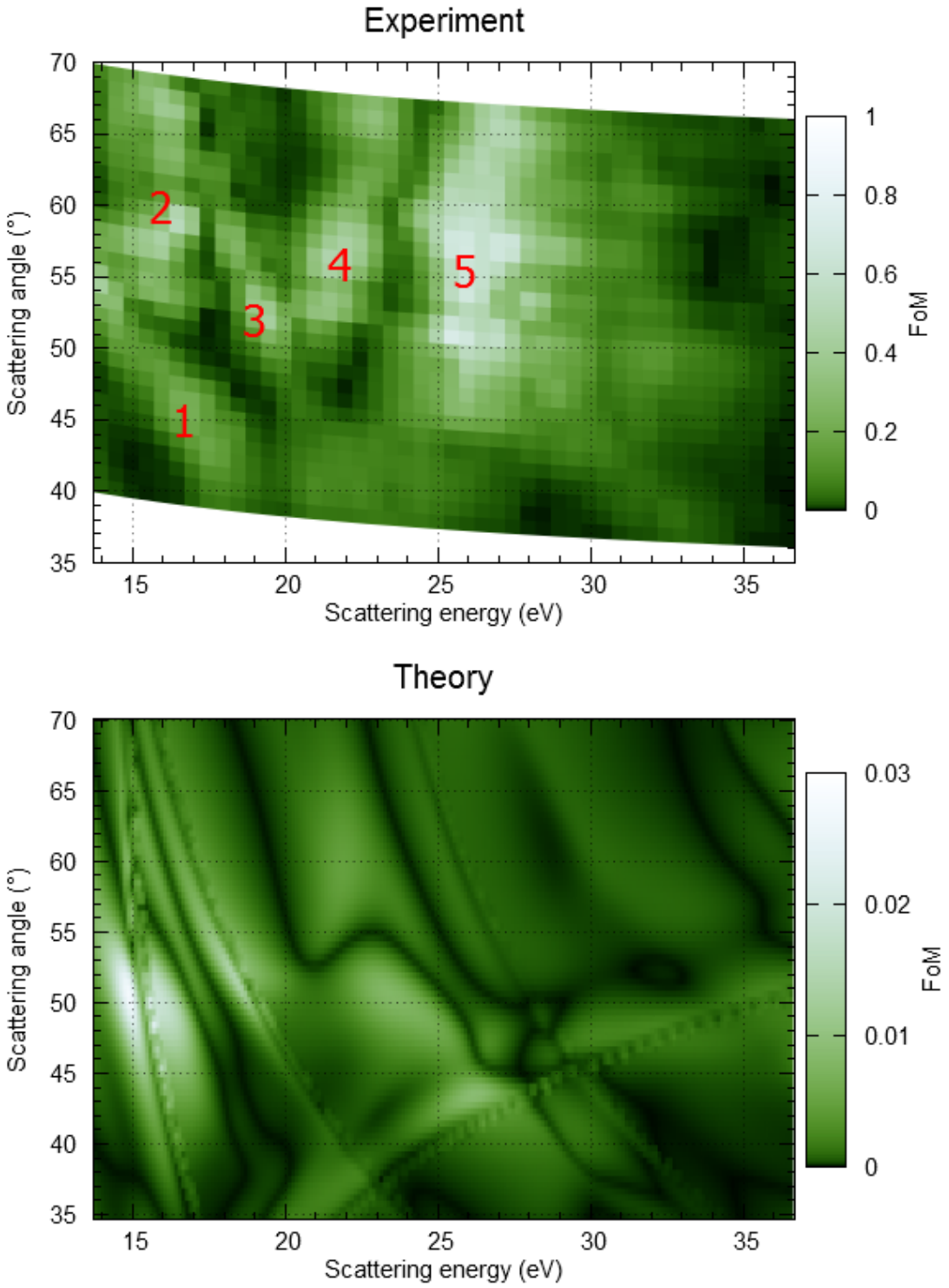

FIGURE 3.12: E-θ-landscape of single-channel figure of merit for W(001), experimental values (top) and data calculated by the relativistic layer-KKR SPLEED code (bottom) [Braun et al., 2013]. The experimental false color scale denotes FoM_{single} according to Eq. 3.1 (c) as a relative scale normalized to the maximum. Numbers 1-5 denote pronounced structures that can be identified in experiment and theory. The theoretical scale is absolute. The scattering plane intersects the surface along the [010] direction

C) $24 < E < 30$ eV and $70° > \theta > 45°$;

D) $19.5 < E < 36$ eV and $30° < \theta < 50°$.

The first three regions (**A**, **B**, **C**) are surface-barrier induced resonances associated with the emergence threshold of nonspecular LEED beams and the last one (**D**) is a bulk-diffraction derived feature. These very fine structures are not resolved in the experimental landscapes probably due to the relatively high energy step width of 0.5 eV in connection with insufficient energy resolution. The second reason is given by certain parameters and settings of the focusing optics which cause nonparallel electron rays with a certain angular divergence, which may lead to the mixture of several scattering angles in one line scan.

A qualitative understanding of the observed asymmetry patterns can be gained from a combination of diffraction and spin-orbit energy. Due to the spin-orbit coupling the energy for spin-up and spin-down electrons is different while they are scattered. This is equivalent to a different wavelength and accordingly leads to slightly changed parameter combinations of angle and scattering energy for constructive or destructive interference.

Interference conditions are created from translational symmetry in-plane (**A**, **B**, **C**) and out-of-plane (**D**). These conditions show up as lines of large or low scattering intensity. Asymmetry values obtained from the difference of the diffraction patterns show the same general dependence on angle and energy with sign changes occurring in between the maximum and minimum conditions. Absolute intensity values also depend on the spin-direction. This shifts the asymmetry sign changes close to the minimum conditions. This general behavior can be nicely observed both in experiment and theory. Negative asymmetry values are largely suppressed below a scattering angle of 45° because of the occurrence of the bulk related interference maximum (**D**).

3.4 Summary

The present measurements of two-dimensional E-θ-landscapes of the spin-orbit asymmetry reveals rather good agreement between experiment and theory. The experimental results confirm the good choice of the geometry (scattering angle 45°) and energy working point (about 27 eV) used in previous setups [Kolbe et al., 2011; Tusche et al., 2011]. The full E-θ-landscape shows that an increased scattering

TABLE 3.1: Comparison of experimental and theoretical values of asymmetry and estimated FoM for 5 different regions. The experimental FoM values are relative values, normalized to the maximum.

Region (cf. Figs. 3.11 3.12	Asymmetry		FoM	
	exp	theo	exp (relative)	theo $\times 10^{-2}$ (absolute)
1	0.27	0.40	22.98	2.79
2	-0.43	-0.87	100	0.57
3	0.44	0.93	55.68	1.55
4	-0.57	-0.93	54.08	0.47
5	0.66	0.76	86.36	0.62

angle of $50° - 60°$ enhances the FoM significantly and, in addition, opens up the possibility of an asymmetry reversal from $S = -53 \pm 5\,\%$ to $+51 \pm 5\,\%$ within just 4 eV change of scattering energy. Additionally, we found other regions (see Table 3.1) with rather high asymmetry and figure of merit, in particular at low energies and higher scattering angles, which open a path to a modification and substantial improvement of the existing multichannel spin detectors.

The useful lifetime of spin detectors based on scattering from W(001) is limited to typically 2 hours at 10^{-10} mbar due to the fast contamination of the surface in UHV by residual gases. This effect requires frequent cleaning by flashing to 1200°C for CO and H desorption, but can be compensated by a higher coherence length of the reflected beam due to smaller mosaicity or mosaic spread of W(001) surface in comparison to the Ir(001) surface. In the future our setup will be used

for the investigation and characterization of such candidates, like e.g. W(001)/O-p(1×1). The determination of full E-θ-landscapes as described in this paper for W(001) and for the highly inert Ir(001)-p(1×1)Au system[Kirschner et al., 2013] can serve as a guideline for the next generation of two-dimensional spin-polarizing mirrors for the application in momentum microscopes [Tusche et al., 2011] and behind dispersive electron energy analyzers[Kolbe et al., 2011].

Chapter 4

Imaging spin-filter for electrons based on specular reflection from Ir(001)

In order to overcome the delay time due to frequent cleaning and flashing of the spin-filter crystal, we searched for a high-Z material with a much longer lifetime. Due to its low reactivity, we have chosen the Ir(001) surface for the present study. This surface is much less reactive than W(001) and should allow for longer lifetimes in UHV. The spin-filter performance of Ir(001) is presented in this chapter along with some examples of its application. A SPLEED-calculation in relativistic layer-KKR code by R. Feder and coworkers served as valuable guideline in search for optimum working points.

The Ewald construction (see Fig. 4.1) in reciprocal space corresponds to specular reflection from Ir(001) at 45° impact angle. The full and dashed circles denote the Ewald sphere for the high- and low-energy working points (see below), i.e. 39 and 10 eV scattering energy, respectively. If extremely low incident kinetic energy is used, the Ewald sphere becomes so small that there are no higher order diffracted beams, leading to increased intensity of the (0,0) specular reflection [Hillebrecht

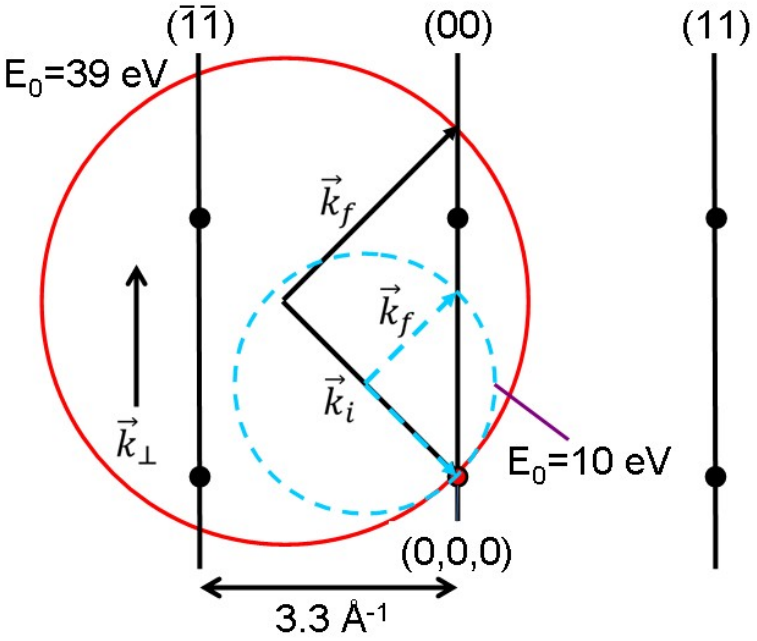

FIGURE 4.1: Diffraction condition for Ir(001) at 45° impact angle in reciprocal space. The size of the Ewald sphere is determined by the scattering energy, here scaled for the case of 39 eV (full circle) and 10 eV scattering energy (dashed circle).

et al., 2002]. This suggests that a spin-filter based on very low energy electron scattering, sometimes referred to as VLEED, may give very high total efficiencies.

4.1 Calculation for Ir(001)

Parallel to the experiments calculations for the $Ir(001) - 1 \times 1$ surface were performed [Feder et al., 2012], yielding the theoretical "landscape" of reflectivity, spin asymmetry and figure of merit as function of scattering energy E and scattering angle θ (impact angle with respect to the surface normal). According to an earlier LEED structure analysis [Besold et al., 1983] the topmost atomic layer of $Ir(001) - 1 \times 1$ is relaxed inward by about 2 %. Using the above described (section 2.4.4) Full-potential Linearized Augmented Plane Wave (FLAPW) computer code FLEUR [FLAPW] under a local density approximation for the exchange-correlation energy, the *ab initio* electronic structure of the ground state of an eleven-layer thin film was computed within density functional theory. The thus

obtained real one-electron potential was augmented by a complex self-energy correction to yield the quasi-particle potential appropriate for SPLEED. The imaginary part of this self-energy correction, which accounts for the influence of inelastic scattering, was chosen as $V_i(E) = 0.1(E+\Phi)^{0.83}$ eV [Samarin et al., 2007], where E is the kinetic energy of the diffracted electron and $\Phi = 5.91$ eV the work function of the sample as obtained from the ground state calculation. The real part of the self-energy correction acts essentially two-fold: firstly, the ground state real inner potential ($V_0 = 15.76$ eV) is reduced with increasing kinetic energy E; secondly, the surface potential barrier moves closer to the topmost internuclear plane. Since these two corrections are not quantitatively known a priori, but would have to be determined by comparing calculated with experimental SPLEED spectra, Feder et al. firstly used the ground state inner potential. For the surface barrier, they employed a smooth form with image asymptotics [Samarin et al., 2007] and performed SPLEED calculations with parameters appropriate for the ground state as well as with values yielding an inward-displaced barrier.

Using the above quasiparticle potential, SPLEED calculations were performed by means of a relativistic layer-Korringa-Kohn-Rostoker (KKR) code [Feder, 1985]. The resulting E-θ-landscapes for the specular beam from the $Ir(001) - 1 \times 1$ surface are shown in Fig. 4.2(a-c). The energy E is the kinetic energy of the SPLEED electrons relative to the vacuum level of a semi-infinite $Ir(001)$ crystal. The scattering plane was chosen to intersect the surface along the (010) direction. Since it is a mirror plane of the semi-infinite crystal, the 00 beam spin polarization vector obtained in the case of an unpolarized primary beam is perpendicular to the scattering plane and equal to the spin asymmetry vector in the case of a spin-polarized primary beam, cf. [Feder, 1985; Kirschner, 1985]. Complete information is therefore contained in the spin-averaged reflectivity I/I_0 and in the spin asymmetry, according to Eq. 3.3. With $I_\uparrow$ and $I_\downarrow$ denoting the specular beam intensities for a completely polarized primary beam with polarization vector perpendicular (up and down) to the scattering plane.

Since the contour plots in Fig. 4.2(a-c) are quite self-explanatory, it may suffice to draw attention to some salient FoM features in Fig. 4.2(c). Below 6 eV, a ridge

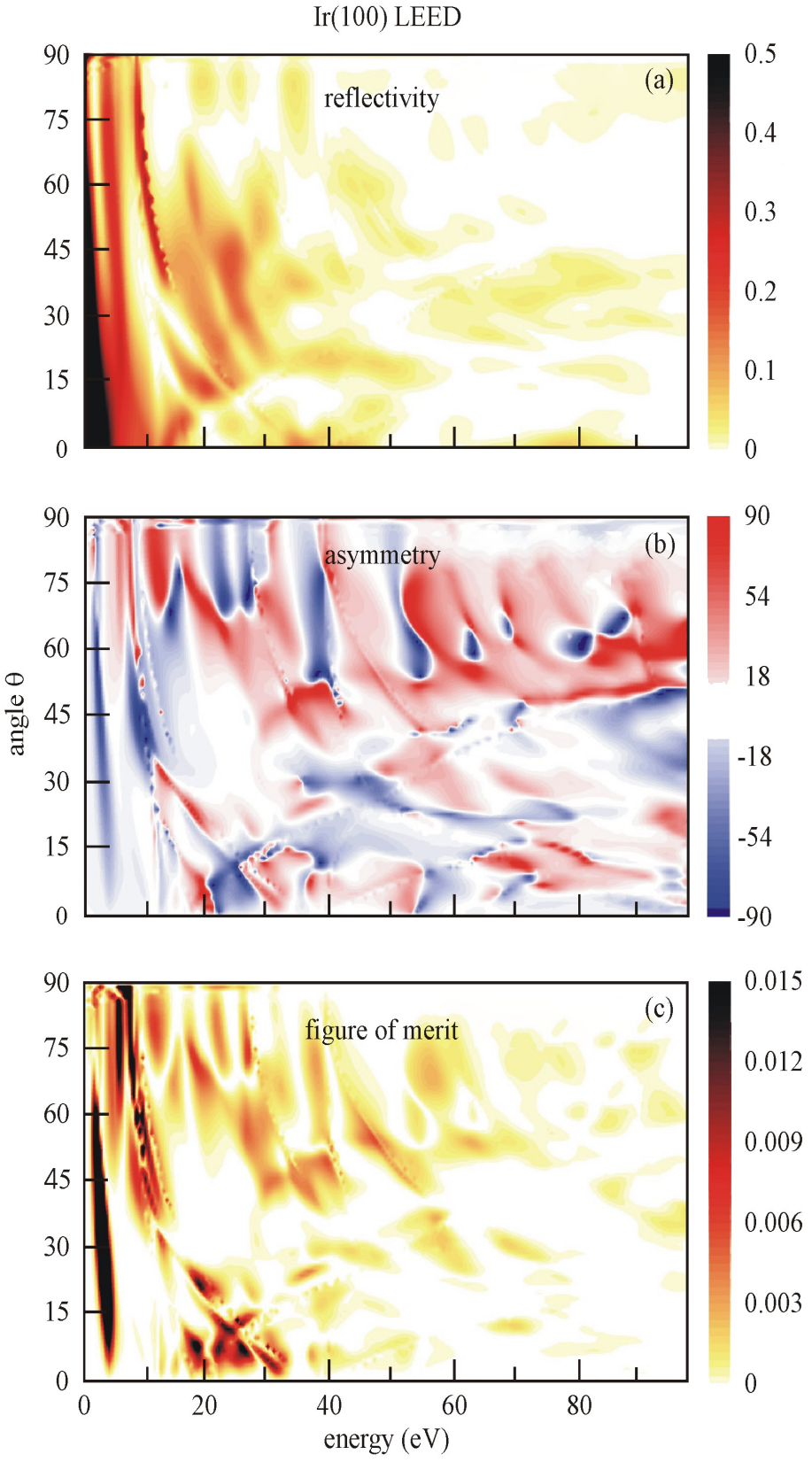

FIGURE 4.2: E-θ-landscape of reflectivity (a), spin asymmetry (b) and single-channel figure of merit (c) for unreconstructed Ir(001), calculated by the relativistic layer-KKR SPLEED code [Feder et al., 2012]. The false colour scales denote absolute spin-averaged reflectivity (a), spin asymmetry according to Eq. 3.3 in % (b) and absolute FoM_{single} according to Eq. 3.1 (c). The scattering plane intersects the surface along the (010) direction.

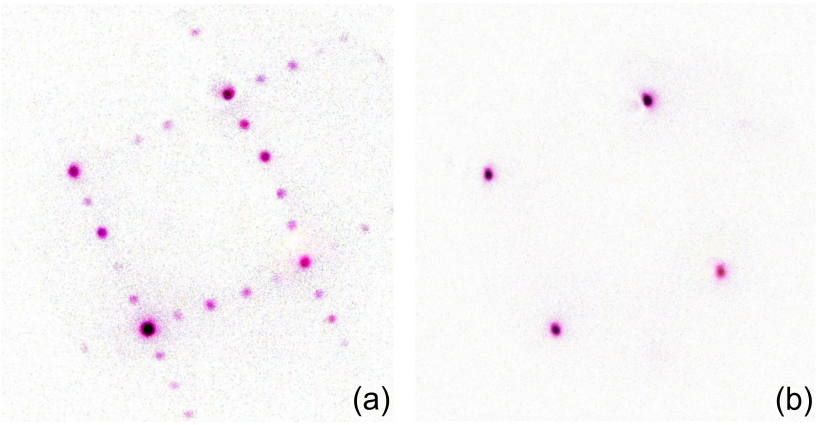

FIGURE 4.3: LEED patterns of the reconstructed Ir(001)-5 × 1 (a) and Ir(001)-1 × 1 surface (b).

with FoM values up to 0.015 extends over a wide angular range, from $\theta = 6°$ to $\theta = 65°$. These values are similar to the peak values obtained in a recent SPLEED study on Au(111) [Samarin et al., 2010], which was, however, restricted to energies below 20 eV and to angles below 40°. For our present spin-filter purpose, angles between 40° and 50° are more suitable. In this angular range, the FoM in Fig. 4.2(c) exhibits, in addition to the already mentioned ridge, two regions with quite sizable values, one between 7 and 14 eV, the other between 30 and 40 eV. At higher energies, there is only a smaller FoM mountain around 52 eV.

4.2 LEED characterization

For initial preparation and characterization of spin-integral reflectivity the Ir(001) crystal was studied by LEED/Auger and recipes for a "blind" preparation in the spin polarimeter were tested out with particular emphasis on the conditions for occurrence of the 5 × 1 reconstruction. Typical LEED patterns are shown in Fig. 4.3. I-V-curves of the specular beam at near-normal incidence (6°) served as a first guideline for comparison with the calculation, see Fig. 4.4. For the LEED studies the Ir(001) crystal was prepared at a base pressure of 7×10^{-11} mbar following the guidelines given by [Musket et al., 1982].

For hot oxygen treatment the crystal was heated up to 1100–1150 K under O_2 partial pressure of 8×10^{-8} mbar during 5 – 10 cycles for 5 minutes. Subsequently a short ($\sim$ 20 s) high temperature ($\sim$ 1600 K) oxide-flash was carried out at 3×10^{-10} mbar. After this procedure the Ir(100) surface always showed the well-known 5×1 reconstruction [Koch et al., 1991; Lehwald et al., 1991] as visible in Fig. 4.3(a). Temperature was monitored by a $W5\%Re/W26\%Re$ thermocouple attached to the crystal.

We also investigated methods to suppress the reconstruction as described in [Heinz et al., 1985; Küppers and Michel, 1979]. These procedures were capable of removing the reconstruction completely (see Fig. 4.3(b)), but sometimes led to an incomplete quenching of the superstructure (faint 5×1 reflexes or lateral inhomogeneous LEED pattern). The reproducibility of the resulting structure was not as reliable as for the 5×1 surface. Hence, all subsequent spin asymmetry measurements were made for the reconstructed surface, produced as described above. It should be mentioned that the Ir(001) $- 5 \times 1$ surface is extremely stable and does not change during many hours of residual gas adsorption at room temperature in a vacuum in the low 10^{-10} mbar range.

LEED patterns were recorded for kinetic energy values in the range of 10–120 eV. On their basis I-V intensity profiles were determined for the 00, 10 and 11 spots. Fig. 4.4(a) shows the measured I-V-curves of the (00) spot for the 1×1 and 5×1 surfaces (the latter being shifted along the ordinate) in comparison with the calculation (full curve). The measurement for the 1×1 surface shows reasonable agreement with the theory curve, with the theoretical maxima and minima being smeared out in the experiment. The I-V-curve for the 5×1 surface looks quite similar as the 1×1 curve, except for an additional maximum around 37 eV. This region of the E-θ-landscape is interesting because it provides a high FoM between 18 and 34 eV (see Fig. 4.4c). Close to 20 eV the theoretical asymmetry shows a pronounced bipolar feature with high extremal values of almost $\pm 100\,\%$, see Fig. 4.4(b). Such points are very useful in practice because they allow to reverse the spin analyzing power for elimination of apparatus-related asymmetries etc. The figure of merit shows peak values of 10^{-2} at a very convenient scattering

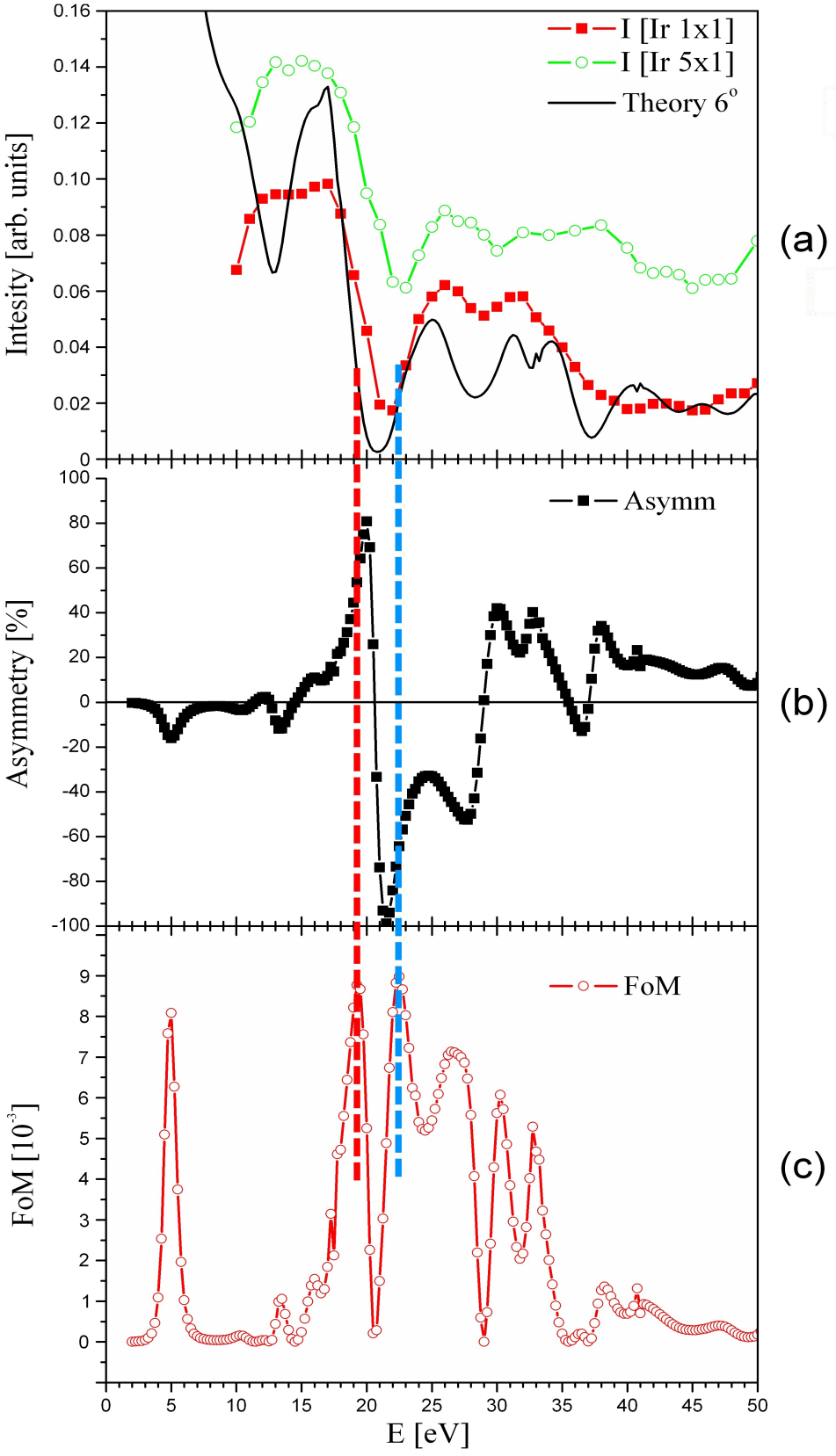

FIGURE 4.4: Measured I-V-curves of the (0,0)-beam at $\theta = 6°$ scattering angle for the reconstructed (open circles) and unreconstructed surface (squares) in comparison with theory (full line) (a). As guideline for the spin filter application we included the theoretical spin asymmetry (b) and figure of merit (c). The dashed lines mark two closely-spaced working points with high FoM but different signs of asymmetry.

energy around 20 eV. The experimental I-V-curves in Fig. 4.4(a) show the same basic structure as their theoretical counterparts except for a slight shift of the minimum. Thus we could expect that the asymmetry and FoM will be similar to the theoretical prediction as well.

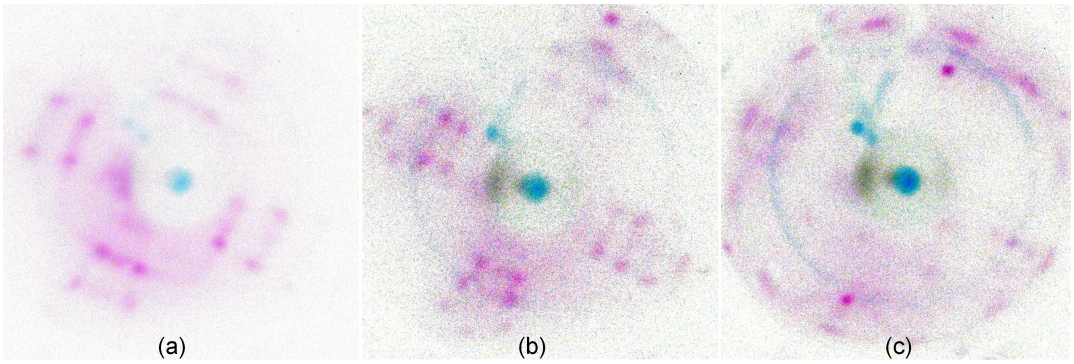

FIGURE 4.5: LEED patterns of the carbon superstructure on the surface of Ir(001) at 13 eV (a), 30 eV (b) and 70 eV (c).

One of the crucial points during preparation and subsequent use the of Ir(001) crystal was proper control of the temperature for the oxygen treatments and high temperature flashes. As it came out (due to temporary problems with the thermocouple) after several overheating cycles of the crystal, the formation of a strong and very stable carbon superstructure was observed on the surface of scattering target, caused probably by creeping of carbon from bulk of the crystal. It was analyzed with LEED and Auger electron spectroscopy (AES) in an ex-situ experiment. The corresponding LEED pattern is shown in Fig. 4.5 for different energies of incident beam. AES gave evidence of a carbon overlayer. Such a strong carbon contamination, especially at low energies, leads to continuous decrease of the measured asymmetry after each high temperature flash, as it was seen during test runs with the spin-detector at the SLS beamtime. These superstructures could not be removed from the surface using the standard preparation procedure of oxidation and flashing as described above. Thus, in order to get rid of it several cycles of Ar ion sputtering with subsequent high temperature flashes for smoothing the surface were necessary. Such a procedure results firstly in the Ir(001) $-$ 1×1 structure (see Fig. 4.3(b)) and secondly, with the help of further oxygen treatment combined with high temperature flashes, lead to the formation of a clean surface

with Ir(001) $-$ 5 $\times$ 1 structure as shown in Fig. 4.3(a)). Final check with Auger spectroscopy revealed that the carbon Auger signal intensity dropped below the instrument noise level.

4.3 Experimental setup

In order to investigate the reflectivity and spin asymmetry as function of scattering energy, the novel imaging spin filter was adapted to a hemispherical electron energy analyzer [Phoibos]. This was done in the frame work of our joint project on ultrafast magnetism seen by time- and spin-resolved photoemission with ETH Zürich, group of Prof. Vaterlaus and Prof. Acremann. Measurements were carried out at two synchrotron facilities: the Swiss Light Source (SLS) at the Paul Scherrer Institut (Villigen, Switzerland) and at FLASH, the soft X-ray free-electron laser (FEL) at DESY (Hamburg, Germany). A beamtime at the SLS we used as the test run in order to check and prepare everything for the beamtime at FLASH, where we successfully demonstrated the feasibility of time and spin resolved photoemission experiments using FEL femtosecond radiation. This experiment confirmed the existence of ultrafast demagnetization processes in iron. A ferromagnetic iron film on tungsten was pumped by an 800 nm femtosecond laser beam synchronized to the FEL time structure. The FEL induced photoelectrons were analyzed with help of our imaging spin filter. The measured spin polarization as a function of time delay shows a decay on sub-picosecond time scale followed by a recovery on the picosecond time scale, in line with previous non-FEL experiments.

For this experiment the multichannel spin filter had to be adapted to a hemispherical electron analyzer (type SPECS, Phoibos150). As compared to our first design [Kolbe et al., 2011], the lens diameters have been scaled up by a factor of 1.5 to account for the larger exit field of this analyzer. For adjustment purposes a real exit slit could be used, whereas for multichannel operation the full exit field of the spectrometer was focused in a demagnified spot onto the spin filter crystal and subsequently focused onto the 2D electron detector in a magnified image using the

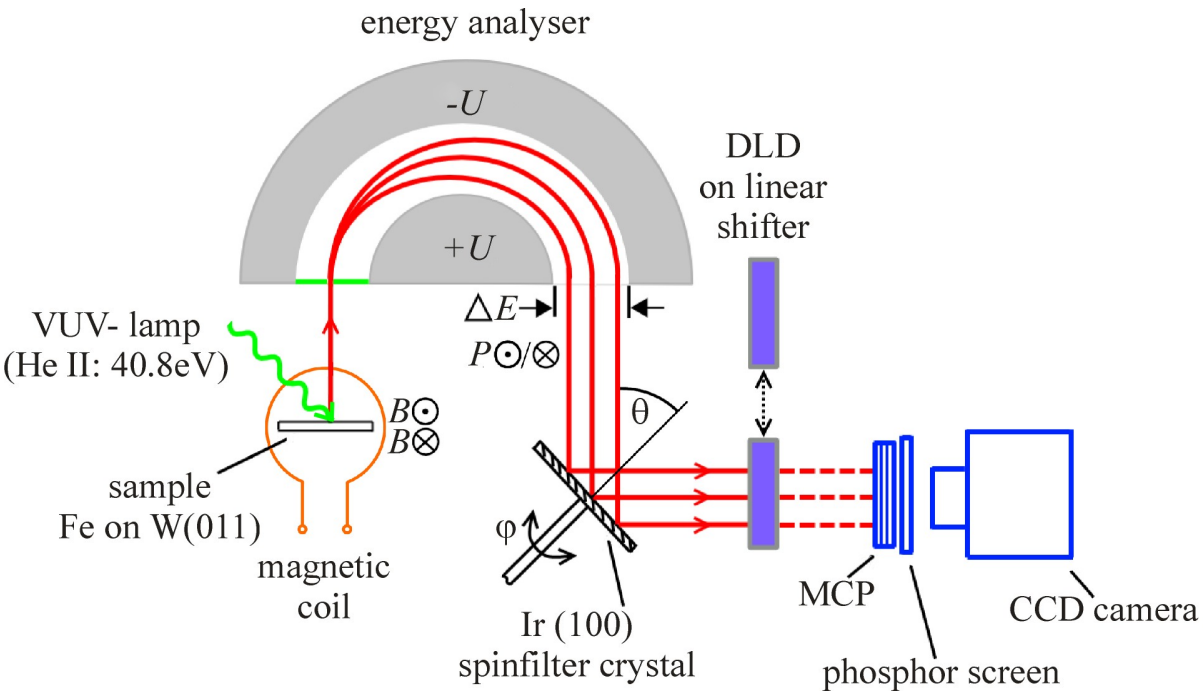

FIGURE 4.6: Electron-optical layout of the imaging spin polarimeter in the dispersive plane (schematic: lenses omitted and scattering plane rotated by 90° with respect to the drawing plane). The spin-filter crystal is rotatable about its surface normal in order to vary the azimuthal scattering angle ϕ at fixed polar angle $\theta = 45°$.

projective optics. The Ir crystal was mounted under a fixed polar scattering angle of 45°. The azimuthal angle could be varied by means of a high-precision rotary motion feedthrough. A schematic sketch of the setup is shown in Fig. 4.6; for sake of simplicity, all lens elements have been omitted.

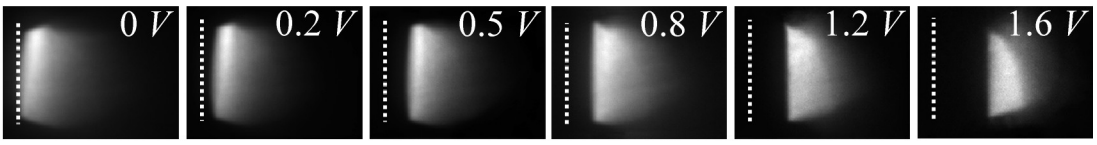

FIGURE 4.7: Snapshots of the secondary-electron distribution taken behind the spinfilter crystal during an energy sweep. Note how intensity maximum and sharp low-energy cutoff shift in the field of view; sweep voltages are given.

For all results shown below the spectrometer was operated at a pass energy of 80 eV. In this case a wide energy band can be accumulated simultaneously. The dispersion of the spectrometer at 80 eV is 0.265 eV per mm, meaning that an interval of 5.3 eV fits into an exit field of 20 mm width. In the multichannel

acquisition mode this 20 mm wide field of view is analyzed simultaneously. If now the kinetic energy is scanned (in the standard operation mode of the spectrometer) the whole spectrum shifts across the field of view as visible in the image series in Fig. 4.7. During the energy sweep, the intensities measured at a given point in the exit field are a function of the coordinate in the exit field and of the present sweep voltage. When summing up the data in the multichannel mode this relation of sweep voltage and coordinate is taken into account. A line scan across the cutoff edge in the series yields a resolution of 160 meV FWHM at these settings. Thus, about 33 energy points can be resolved simultaneously.

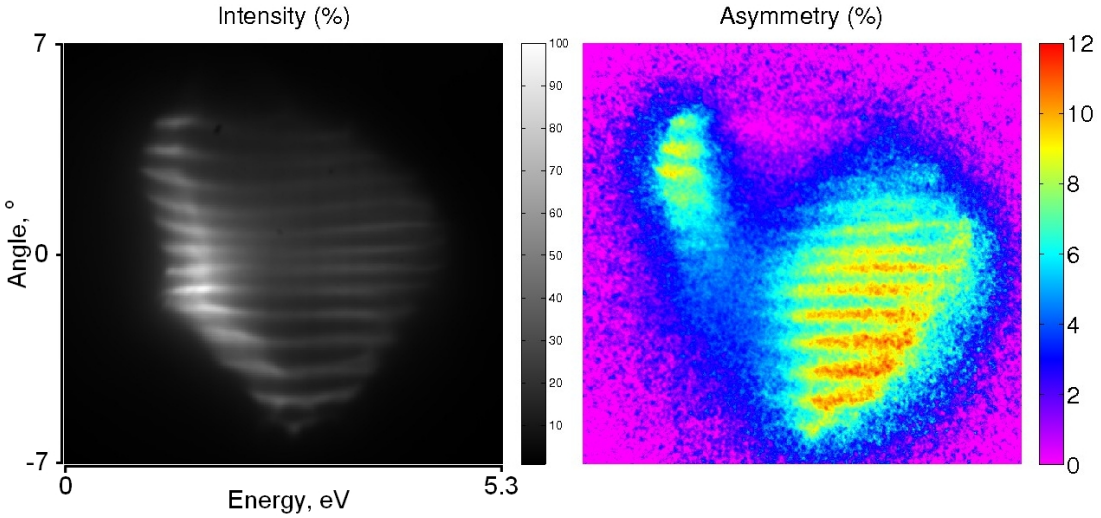

FIGURE 4.8: Measured intensity and corresponding asymmetry. Calibration grid inside.

In non-dispersive direction a fine grid could be inserted in front of the entrance lens of the spectrometer just for angular calibration purpose. That grid can be easily removed during measurements. It consists of 23 slits of 0.2 mm width and 1 mm period. Corresponding intensity and asymmetry images with grid shadow (wavy structure) are shown in Fig. 4.8. Using linescas (shown in Fig. 4.7) as well as grid helped us to quantify energy and angular scale. Thus in the low-angular-dispersion mode an interval from $-7°$ to $+7°$ polar emission angle from the sample can be accepted. From a linescan across this grid pattern we conclude that more than 30 angular intervals can be acquired simultaneously. Hence, N in Eq. 3.2 is almost 1000.

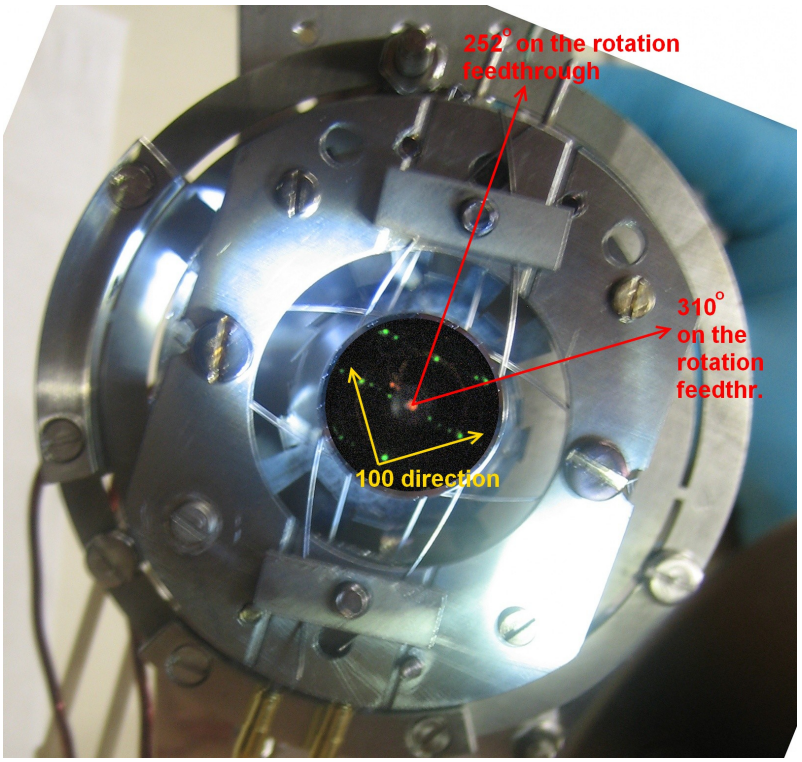

FIGURE 4.9: Ir(001) crystal assembly with LEED patterns matched with corresponding orientation.

The electron image could either be accumulated using the common multichannelplate – screen – CCD camera imaging unit that is normally used directly behind the electron analyzer. Alternatively we used a single-electron counting delayline detector [Oelsner et al., 2001], which can be moved into the beam path using a linear motion feedthrough. The DLD is characterized by a large dynamic range of more than 5 orders of magnitude. It has an active diameter of 40 mm, a spatial resolution of about 50 μm and a maximum count rate of 10^7 counts per second. An isolation valve of ultra-flat design (thickness of shutter plate only 2 mm) was integrated into the transfer optics between spectrometer and spin detector, in order to shut off the spin detector from the main vacuum system during preparation of the spin-filter crystal or the sample in the main chamber.

Prior to the main measurements azimuthal angle adjustment was done for the optimization of the scattering asymmetry. It is known from previous measurements on W(001) and W(110) [Kirschner, 1985; Samarin et al., 2013; Venus, 1993] that the azimuthal dependence of scattering asymmetry in so-called rotation diagrams

can be very pronounced and can even show reversals of sign (that in principle could be utilized for elimination of apparatus-related spurious asymmetries). As it turned out it was quite crucial also in our case. Azimuthal angle variation was done in 2.5° steps, refered to the optimum position, (defining $\phi = 0°$). The resulting intensity and asymmetry patterns are shown in Fig. 4.10 for positive and negative angle directions. Proper orientation of the crystal on the crystal holder was additionally checked in LEED before installation into spin-scattering chamber. As it is visible from Fig. 4.9, LEED patterns of clean Ir(001) with 5×1 reconstruction was matched to the crystal surface as it was fixed and oriented in the LEED chamber. Thus we could note the corresponding values on the high precision rotation feedthrough, which facilitated for the azimuthal orientation of the scattering target inside of the spin chamber. The optimum angle (see Fig. 4.10) was chosen as $\phi = 0°$ reference for the azimuthal dependence measurement.

As we can see from the images in Fig. 4.10, change of azimuthal angle by 5° leads to decreasing of the asymmetry by about 25 % and rising of the negative asymmetry area. Further rotation decreases positive as well as negative asymmetry extrema. Thus, already at $\phi = -12.5°$ we observed almost complete vanishing of the spin asymmetry as well as decreasing of the effective working area. Additionally, moving and rearrangement of areas with maximum positive and negative asymmetries is visible over the whole measured sequence.

Intensity images in Fig. 4.10 also shown severe changes. Firstly, squeezing of the effective working area in both direction (dispersive and non-dispersive), which leads to decreasing of energy and angle intervals, could be observed. Secondly, strong distortion of the angular-calibration stripes could be caused by non proper orientation of the scattering crystal surface. All these problems pushed us to construction and installation of improved crystal goniometers, e.g. hexapod manipulators in the next generation of spin-filter detectors in order to fulfill all possible angle and tilt adjustments of the scattering crystal.

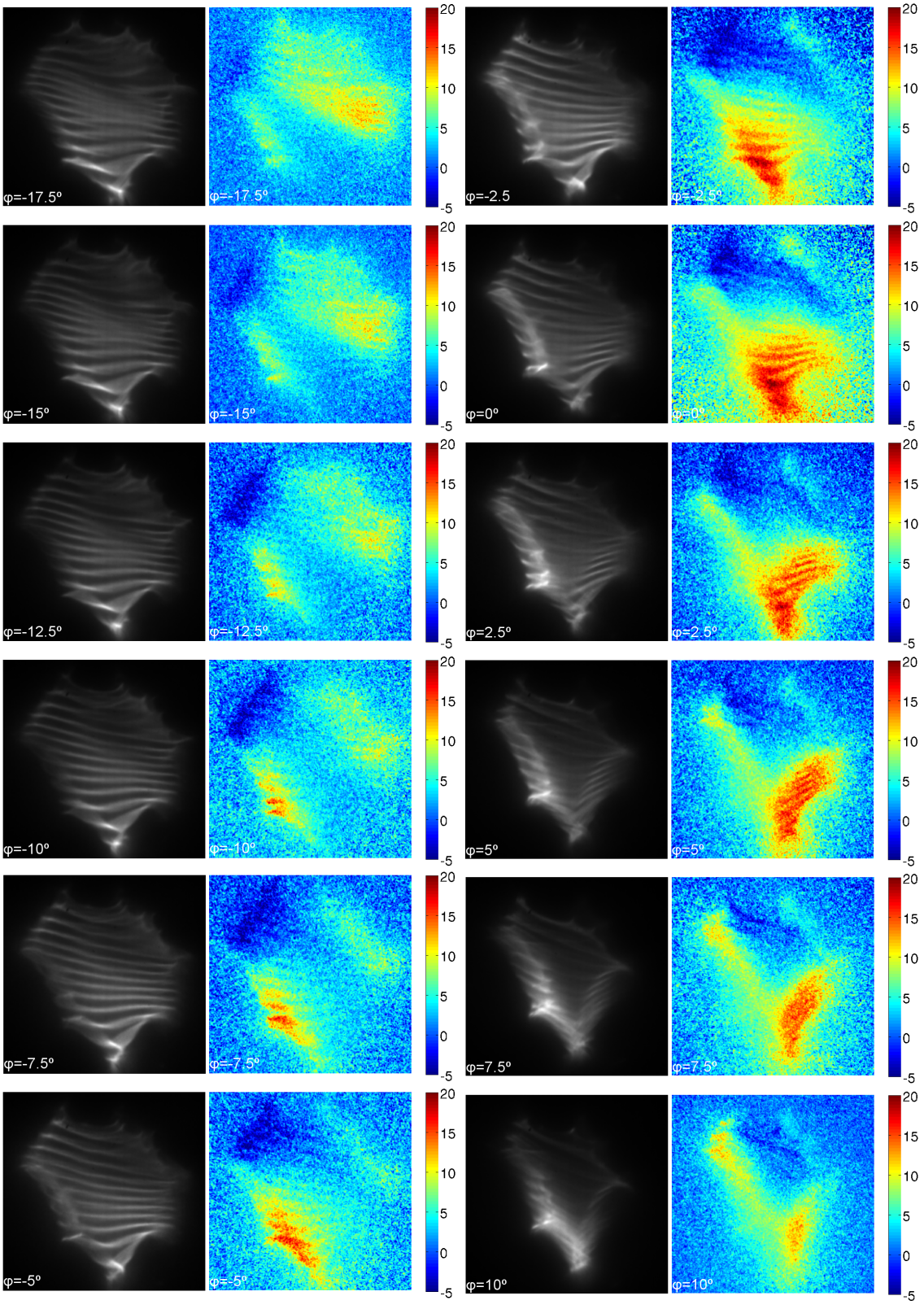

FIGURE 4.10: Azimuthal variation of intensity and asymmetry.

4.4 Measurements of reflectivity and spin asymmetry at 45°

Theory predicts several regions of high FoM at angles of incidence between $\theta = 40°$ and 50°. A scattering geometry around $\theta = 45°$ is very convenient for a practical design of the spin filter. Therefore we have studied this scattering region in detail using the set-up sketched in Fig. 4.6. As polarized source we used the secondary electrons from an epitaxial Fe film of 15 ML thickness on W(110), providing a spin polarization of 30% in the intense peak of the secondary-electron cascade [Allenspach and Landolt, 1986; Landolt, 1986]. Details of the sample preparation and characterization explained are in the article [Miesch et al., 2011].

The experimental data have been taken for freshly-deposited Fe films magnetized by an in-vacuum coil along the two directions perpendicular to the scattering plane. At each energy the spin asymmetry A was determined according to Eq. 3.3 from the intensity distributions $I_\uparrow$ and $I_\downarrow$ for opposite magnetization directions. Switching of the magnetization was done by the coil pair. The coils are arranged like a Helmholtz pair and placed behind the sample, but are oriented such that the coils' plane is parallel to the sample surface, giving rise to a large magnetic stray field, which is used to switch the sample [Fognini et al., 2012]. The denominator of Eq. 3.3 is proportional to the spin-integral intensity. The results are summarized in Fig. 4.11(a-i) together with line scans in the theoretical E-θ-landscape along $\theta = 45°$. In addition, sections of the false-color plots of reflectivity, asymmetry and FoM between 30° and 60° are included on the same energy scale in order to illustrate the angular dependence around 45°.

The figure reveals rather good overall agreement between theory and experiment, despite the fact that the calculation and measurement were made for the unreconstructed and 5×1 reconstructed surface, respectively. Many details (G-M) of the pronounced structure of the measured spin asymmetry (spectrum f) agree well with theory (spectrum e). For the reflectivity the agreement is obviously worse, both concerning signal positions (e.g. B and C) and intensity (e.g. deep minimum

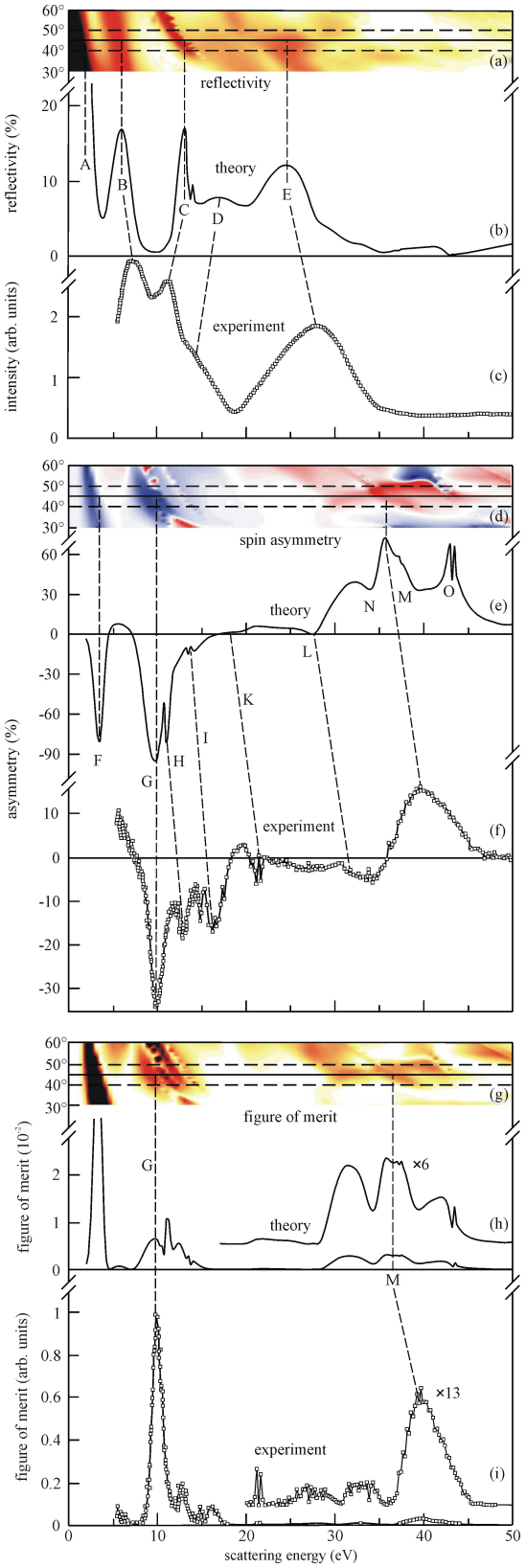

FIGURE 4.11: Results for reflectivity (a-c), spin asymmetry (d-f) and figure of merit (g-i) for elastic specular scattering from Ir(001) at $\theta = 45°$. Note that the measurement was taken for the 5×1 reconstructed surface (c,f,i), whereas the calculations assumed a non-reconstructed surface (b,e,h). The false-color plots represent details of Fig. 4.2 in the angular range of 30°-60°.

in experimental spectrum (c) between signals D and E. The measured figure of merit (spectrum i) reveals two prominent working points in this energy range below 50 eV, as predicted by theory (spectrum h). Again, significant deviations are obvious. In the following we will discuss these results in detail.

The experimental and theoretical energy scales have been adjusted at the pronounced negative peak G in the asymmetry curve at low energies. Best agreement was achieved by a small shift of the experimental curve (by 1 eV) to higher energy. The energy scale of the experiment is derived from the potential difference (including the work function difference) between the electron source (in this case the secondary electron signal of the iron film with the kinetic energy being selected by the spectrometer) and the spin filter crystal. The theoretical energy scale from Figs. 4.2(a-c) and 4.11(a-i) is the kinetic energy of the diffracted electrons with respect to the vacuum level above a semi-infinite iridium crystal. The diffraction energy inside of the material depends on the quasi-particle inner potential, which is not known quantitatively. For the results shown in Fig. 4.2(a-c) we had taken the ground state inner potential $V_0 = 15.76$ eV. In a future experiment we will determine the true scattering energy using a time-of-flight technique and thence also the quasi-particle inner potential.

The *low energy working point* at about 10 eV scattering energy is characterized by a high peak in the figure of merit (theoretical value 1×10^{-2}) but relatively narrow usable energy band of about 1 eV FWHM. This is a favorable working point for high-resolution applications. The measured spectral variation of the spin asymmetry (f) agrees in many details with the theory curve (e). The asymmetry values of the experiment are consistently smaller, similar as found for the Au(111) case [Samarin et al., 2010]. For the shown measurement sequence an experimental asymmetry maximum of 11 % at the given primary polarization of 30 % [Allenspach and Landolt, 1986; Landolt, 1986] we derive a maximum asymmetry function S of 37 % in peak G. This value is about a factor of two smaller than the theoretical prediction. In later measurements after many more preparation cycles the asymmetry extremum value increased to about 70 %, still somewhat smaller than the theoretical value of 95 %. We conclude that there are contributions to

the scattering process that are not included or not treated properly in the theoretical code. An intrinsic contribution may be incoherent (elastic) scattering, an indication being that the intensity minima in Figs. 4.11(c) and 4.12(c) are not as deep as their theoretical counterparts. As possible extrinsic reasons we can name the limited energy and angular resolution of the electron beam at the spin filter crystal. The theoretical profile shows wings at both sides of the sharp maximum, the measurement (spectrum i) reveals a wing only on the high-energy side.

The dashed lines and labels G - M denote characteristic features that agree quite well. Polarization feature F is not visible in experiment, most likely due to strong quenching of such low kinetic energies as 5 eV by spurious magnetic fields. Theoretical features N and O are also not visible. Possibly they are smeared out and merge into the broad experimental peak M.

The sections of the E-θ-landscape indicate the angular variation of the features. We see that the negative asymmetry extremum G is centered at about $\theta = 45°$, see dark blue feature in (d). Above 52° and below 35° it is accompanied by regions of reverse asymmetry as visible in the red regions in (d). We will see below that these in fact occur in the scattering patterns.

The *high-energy working point* is characterized by a broad maximum of positive asymmetry M centered at about 39 eV. The FoM curve shows a FWHM of 5 eV, meaning that this working point is well suited for cases where a large energy band is analyzed simultaneously. It lies on the high-energy side of the intensity feature E. Experimentally, the intensity feature is broadened and does not show a splitting into several maxima as predicted by theory. The theoretical maximum N is merged into the broad peak M and the sharp double peak O is missing in the measured asymmetry curve. In the asymmetry landscape (d) the maximum shows up at significantly larger angles of incidence of almost 50° (dark red feature in d). This is different from the low-energy point, where both extrema intersect the 45° line. An interesting feature is visible around 33 eV scattering energy, i.e. in the wing of the intensity maximum. We observe a clear negative asymmetry feature L (in theory only a small dip reaching zero asymmetry). This negative extremum

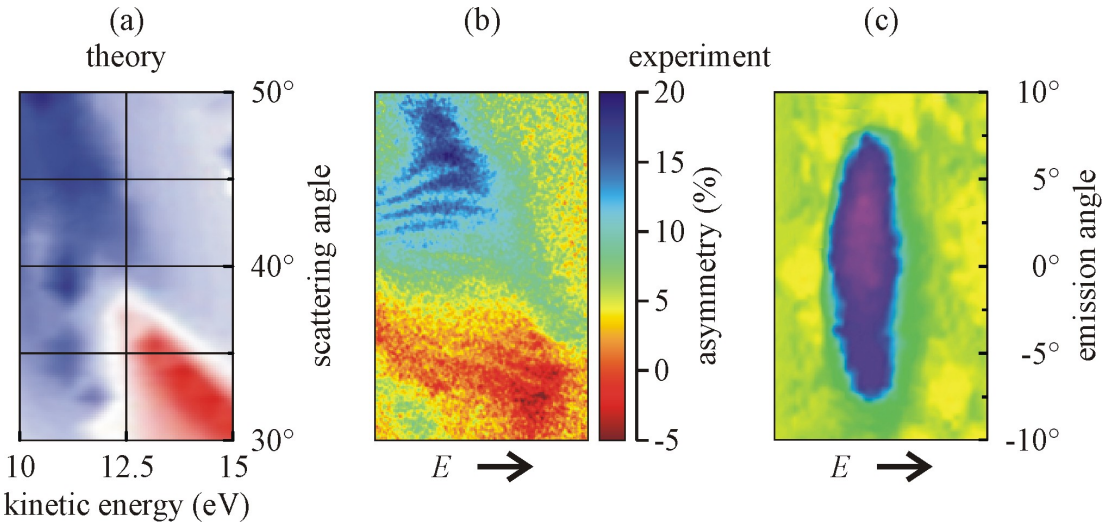

FIGURE 4.12: Theoretical asymmetry pattern around the low-energy working point. Detail of Fig. 4.2(b) is given in (a). Asymmetry pattern observed in the exit plane of the analyzer in this energy vs scattering angle region (b). The wavy structure originates from a grid inserted into the electron optical path to mark the angles. Pattern obtained at a different setting with homogeneous asymmetry function in the oval field of view (c).

offers the possibility of *asymmetry reversal* for zero calibration by taking electron distributions in the 39 and 33 eV extrema.

In search for the origin of the discrepancies between experiment and theory we found that they cannot be removed by physically reasonable changes of the input parameters to the SPLEED calculations for the unreconstructed surface, in particular not by displacements of the surface potential barrier. This leaves us with ascribing them to genuine differences of the SPLEED spectra for the 1×1 and the 5×1 surface geometry. It is clear from Fig. 4.7 that the scattering energy varies along the lateral coordinate in the drawing plane, also called dispersive plane because electrons with different energies are dispersed in this plane. In the non-dispersive plane perpendicular to the drawing plane different angles are "sorted", up to an interval of $\pm 15°$ emission angle from the sample. The electron optics can be adjusted in such a way that the variation of the emission angle at the sample shows up in terms of a variation of the scattering angle at the spin filter crystal. Under such conditions the lateral coordinates in the observed pattern correspond to scattering energy and –angle and one can directly observe a small section of the

2D landscape like the inset (d) in Fig. 4.11. Such measurements are performed in a spectral region where the spin polarization of the source signal is constant. An example of this kind of measurement is shown in Fig. 4.12. A comparison of theory (panel a) and experiment (panel b) reveals in both cases a characteristic bipolar asymmetry feature in the low-energy region between 10 and 15 eV scattering energy and 30° and 50° scattering angle. The asymmetry maximum of 20 % corresponds to a spin sensitivity (Sherman function) of about 70 %.

The wavy structure in the image results from a grid that can be shifted into the electron optical path for optimizing the angular resolution in test experiments. For real spectroscopic measurements the grid is retracted. Systematic measurements of this kind allow mapping out the full 2D asymmetry landscape as demonstrated in 3. For normal measurements the electron optics is adjusted such that the asymmetry function varies only little across the field of view. Such a case is shown in Fig. 4.12(c). In this working point the asymmetry is practically homogeneous in the field of view and the vertical scale directly represents the emission angle from the sample, as denoted by the right ordinate. Here the angular grid was retracted. In general, the variation of the asymmetry function across the field of view must be taken into account via the image acquisition software as we discussed in [Tusche et al., 2013].

4.5 Spin- and time-resolved measurements

All these characterizations of the spin-detector were done in the framework of our joint project with ETH Zürich, Laboratory of Solid-State Dynamics and Education. This group focuses on the fast manipulation of magnetic order and the fundamental properties of matter which limit this fast dynamics. In order to achieve this goal, spin- and energy-resolved photoemission experiments are carried out at various free electron laser (FEL) sources and also with bench-top laser systems. As it is known if a ferromagnet is exposed to an ultrafast laser pulse its magnetization can be reduced within less than a picosecond [Beaurepaire et al.,

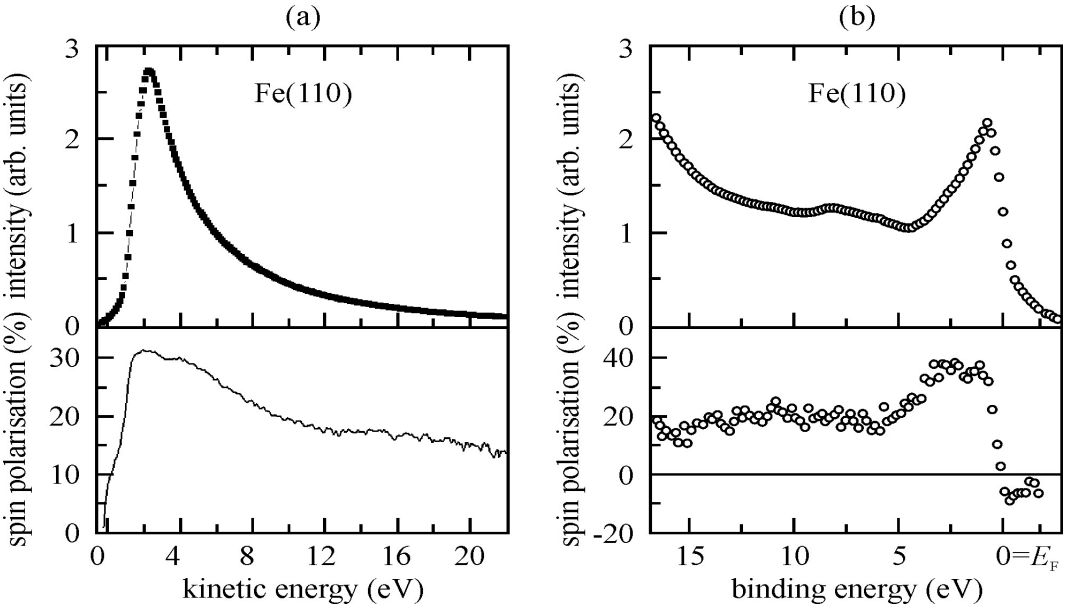

FIGURE 4.13: Intensity and spin polarization spectra of the secondary electrons from an Fe(110) thin film induced by electron bombardment (a) and spin-resolved ARUPS spectrum of the same sample taken with He radiation (b).

1996]. Most detection schemes for the magnetization focus on electrons close to the Fermi energy (by magneto-optical Kerr effect and threshold photoemission) or the density of empty states (using the circular dichroism effect). But on the on a sub-picosecond time scale it is quite demanding to detect the "classical" magnetization (the average spin polarization of the whole valence band). Thus, this project uses spin- and time- resolved photoemission using free electron laser radiation [Fognini et al., 2013]. An intense femtosecond 800 nm laser pulse excited an iron film. In order to detect the "classical" magnetization of the sample vacuum ultraviolet pulses from the free electron laser FLASH in Hamburg extracted polarized photoelectrons. Their spin polarization was detected by our novel spin analyzer based on specular reflection from an Ir(001).

Typical spectra taken with this set up are shown in Fig. 4.13. The left panel (a) shows a spin-resolved spectrum of the secondary electrons, after excitation with 10 keV electrons. The spectrum agrees fairly well with literature data. The feature above 12 eV was also observed in previous work [Allenspach and Landolt, 1986; Landolt, 1986] and is presumably a final-state feature. The right panel (b) shows a spin-resolved photoelectron spectrum taken with a Helium lamp. The spectrum

shows the characteristic rapid drop of the spin polarization from positive values below the Fermi energy to negative values at the Fermi energy. The value of the asymmetry two times smaller then reported in Ref. [Kurzawa et al., 1986], which likely can be explained by different experimental conditions, and in particular by the larger angular range used for the averaging of the signal. These spectra have been taken in multichannel mode at a pass energy of 80 eV, with the exit field of the analyzer fully open, as explained in Fig. 4.6. For the spectrum in Fig. 4.13(b) the angular range was $\pm 7^\circ$ at an angular resolution of 0.5°. The energy resolution was about 400 meV and the spectrum was acquired in 0.5 h. Both spectra are displayed after integration over the angular coordinate. More details of the multichannel acquisition mode can be found in [Kolbe et al., 2011].

For the time-resolved measurements a newly developed multi-segmented delayline detector (DLD) was used. The purpose of this novel detector is to solve the problem of multi-hit particle detection on high-brilliance but low-repetition-rate sources like free electron lasers because many events have to be registered within one pulse. It consists of an array of $16 \times 9 = 144$ discrete anodes, where the 16 columns are read out by a 16-channel DLD electronics unit, whereas the 9 rows are separated by delayline coupling. The readout of each channel is designed such that all 9 in a row can register simultaneously a hit, thus all 144 anodes can register hits in parallel. The dead time of the detector is as short as 80 ns. This approach increases the detection efficiency by more than an order of magnitude (limited by Poisson statistics) in comparison to the standard DLD [Oelsner et al., 2001]. Data acquisition was based on LINUX and integrated in FLASH DAQ system to transfer all results synchronously per macrobunch. For details, see [Luschchyk et al., 2014].

4.6 Summary

The present chapter is the result of the quest to find a novel material with much larger lifetime in UHV, thus avoiding the frequent flashes required for tungsten.

We found that the Ir(001) surface is a very good alternative to W(001). Its spin analyzing power is very high, the Sherman function reaches values up to 70 %, it shows very good imaging properties in the spin filter application and typical lifetimes of the freshly prepared surface were about one day. As a guideline for the search for extrema in the figure of merit the reflectivity and spin asymmetry in the 2D E-θ-landscape (scattering energy vs angle of incidence)was calculated by Feder et al. using a relativistic layer-KKR SPLEED code.

Ir(001) was first studied using LEED/Auger with emphasis placed on a reproducible preparation of the surface, being mandatory for the application as imaging spin filter. We found that the clean 5×1 reconstructed surface could be prepared reliably, whereas recipes removing the reconstruction often left residues of reconstructed regions on the surface. Thus, all measurements have been performed for the clean, reconstructed surface. First results for ultrathin layers of Au on Ir(001) suggest that this system exhibits a non-reconstructed surface and offers the chance for a further substantial improvement of the lifetime of the surface in UHV. This was confirmed in the recent results from Kirschner et al., where the authors presented experimental and theoretical results of two-dimensional E-θ-landscapes of the pseudomorphic monolayer of Au on Ir(001) [Kirschner et al., 2013]. Similar as visible in Fig. 4.11f for the (5×1)-Ir(001) surface, Kirschner et al. found a pronounced, broad asymmetry extremum of 77 % around 40 eV scattering energy and 45° scattering angle. This paper appeared when the present studies were finished.

The central result of chapter 4 is the survey study of spin asymmetry and reflectivity for the 5×1 surface in the energy region up to 50 eV at an angle of incidence of 45° in specular geometry. Two attractive working points were found in this region: At 10 eV we find the total maximum in figure of merit in a rather narrow peak of about 1 eV width; at 39 eV scattering energy we observed a broad maximum characterized by a usable energy interval of 5 eV.

Despite of the fact that the experiment was performed for the 5×1 reconstructed surface, and theory studied the non-reconstructed surface, the overall agreement of

experimental and theoretical spin asymmetry curves is rather good. We can conclude that relativistic layer-KKR SPLEED calculations provide a valuable guideline in the search for other high-Z spin filters. Generally, the agreement is significantly better for the asymmetry than for the reflectivity. In the asymmetry (Eq. 3.3) many secondary influences like transport losses etc. cancel out, because they act in the same way on $I_\uparrow$ and $I_\downarrow$. However, such effects alter the reflectivity.

The agreement between theory and experiment is apparently better in the low energy region. This may be due to the larger probing depth owing to the increasing inelastic mean free path at low energies. Thus, the relative contribution from the reconstructed surface is smaller in relation to the contribution from deeper-lying layers. In search for the origin of the discrepancies it was found that they cannot be removed by physically reasonable changes of the input parameters to the SPLEED calculations for the unreconstructed surface, in particular not by displacements of the surface potential barrier. This leaves us with ascribing them to genuine differences of the SPLEED spectra for the 1×1 and the 5×1 surface geometry.

The results confirm that an angle of incidence of 45° is a good choice in the total E-θ-landscape. The other regions with large FoM (at 6° and 18 – 28 eV or the low energy region above 70°) are attractive as well, but geometrically less favorable for the present experiment.

Chapter 5

Summary and Conclusion

Since the pioneering work of Kirschner and Feder in 1979 spin detectors based on spin polarized low-energy electron diffraction (SPLEED) are widely used as polarimeters in spectroscopy, for generation of magnetic images in the scanning electron microscope with polarization analysis (SEMPA) and, more recently, for parallel-imaging spin filters. The prototype high-Z material for SPLEED detectors is still W(001) since it is best understood and its preparation is comparably easy. Moving to specular reflection of electrons from the W(001) surface at low energies lead to the implementation of the multichannel approach with higher detection efficiency well suitable for different kinds of spin-resolved spectroscopies and microscopies [Kolbe et al., 2012, 2011; Tusche et al., 2013, 2011].

The present work aims at a systematic survey study of the use of imaging spin filters for electrons based on the specular reflection from two high Z-materials, i.e. W(001) and Ir(001).

Up to very recently there was a lack of experimental investigations of two-dimensional E-θ-landscapes of such materials suitable for spin filter applications. However, theoretical relativistic layer-KKR SPLEED calculations were done and served as guideline for the design, fabrication and usage of novel types of imaging spin filters. This problem was overcome by the full 2D E-θ survey study in chapter 3, focusing on the experimental and theoretical investigations of spin-polarized electrons

scattered from W(001). For a wide range of energies (from 12 to 37 eV, which is mainly used for such purposes) and angles of incidence of spin-polarized primary electrons between 30° and 60° the reflectivity and spin asymmetry of the specularly reflected beam was measured and compared with a recent first-principles calculation. The full E-θ-landscape reveals that an increased scattering angle of $50° - 60°$ enhances the FoM significantly and, in addition, opens up the possibility of an asymmetry reversal from $A = -53 \pm 5\,\%$ to $+51 \pm 5\,\%$ within just 4 eV change of scattering energy. Several regions of high asymmetry and sizable intensity were identified in the resulting energy-angular landscapes. They revealed rather good agreement between experiment and theory.

In the second part of this thesis another high-Z material for the spin filtering purpose was investigated, with longer lifetime in ultrahigh vacuum, Ir(001). It is much less reactive than W(001) and has even higher efficiency according to the geometrical and electronic structure investigations based on *ab initio* calculation within density functional theory. Relying on the relativistic layer-KKR SPLEED calculation of the two-dimensional E-θ-landscapes, we fixed the scattering angle in our detector to 45° in specular geometry and explored a wide scattering energy range (few eV up to 50 eV) in order to characterize and determine the spin analyzing power of the 5×1 reconstructed surface of the Ir(001) spin filter crystal. As a result, two attractive working points were found with high spin asymmetry and reflectivity.

The limits of the imaging spin filter with respect to aberrations are very different for different applications. Behind the exit of a hemispherical analyzer we encounter a very large field of view (width 20 mm or more) for large state-of-the-art spectrometers and also a large angular divergence of about 4° (characteristic for hemispherical analyzers). Furthermore, the kinetic energy varies by 5-10% of the pass energy across the field of view. This leads to electron-optical aberrations that set a limit to the number of simultaneously resolvable data points. Simulations reveal that more than 40 energy intervals and 40 angular intervals (i.e. > 1600 data points) can be principally resolved in this mode. The maximum value is

dictated by electron-optical aberrations. Experiments to explore the limit are under way. In a photoemission microscope (or momentum microscope) the field of view is small and beam divergence can be reduced to 0.5° to 1° at the position of the spin filter. Tusche et al. [Tusche et al., 2013, 2011] demonstrated that almost 4000 data points can be resolved in spin-filtered PEEM using a W(001) crystal. Unlike the first case, here the limit is set by the diffraction process, in particular the angular spread of the diffracted beam and the mosaic pattern of the spin-filter crystal. A thorough discussion of these influences and the procedure for quantitative measurements in the microscopy application is given in [Tusche et al., 2013]. In a third application the imaging spin filter is combined with time-of-flight photoelectron spectromicroscopy. In this case, the chromatic aberration due to the energy spectrum acquired simultaneously and the width of the usable asymmetry features of the spin-filter crystal set additional requirements. For this application the 5 eV wide asymmetry profile at the high energy working point (cf. Fig. 4.11(f)) is advantageous.

Our experiments point out that the superior performance of multichannel spin detectors based on specular reflection from high-Z materials promises a bright future of novel experiments in spin-physics. It provides a powerful method for magnetic domain imaging with an efficiency higher than exploiting magnetic circular dichroism (MCD) [Tusche et al., 2011]. The parallel image acquisition further paves the way to single-shot experiments at ultra-bright fs-sources like FELs. Combined with a hemispherical electron spectrometer, the spin filter improves spin detection efficiency by orders of magnitude and thus facilitates experiments on highly reactive surfaces like in-situ prepared Heusler films, radiation-sensitive organic layers or in low-intensity spectroscopy like Spin-HAXPES. Also it opens a way to momentum microscopy with integral analysis of the spin polarization and momentum distribution of photoelectrons.

A possible further improvement of the multichannel method will be the exploitation of the exchange scattering from a ferromagnetic surface or thin film. In that case the spin asymmetry can simply be reversed by reversing the magnetization direction of the target. This is not possible in spin-orbit scattering, where the

asymmetry can only be changed by variation of the scattering energy or angle. A particular interesting system is the oxygen-passivated surface Fe(001)-p(1 × 1)O which shows lifetimes of weeks in UHV [Okuda, 2013; Okuda et al., 2008]. For that surface two orthogonal spin quantization directions can be measured by switching magnetization between the two orthogonal in-plane magnetization directions.

Bibliography

Akai, H. (1998). Ferromagnetism and its stability in the diluted magnetic semiconductor (In, Mn)As. Phys. Rev. Lett., 81(14):3002–3005.

Akatsu, T., Plössl, A., Stenzel, H., and Gösele, U. (1999). GaAs wafer bonding by atomic hydrogen surface cleaning. Journal of Applied Physics, 86(12):7146–7150.

Alder, B., Fernbach, S., and Rotenberg, M. (1968). Methods in computational physics: Energy bands of solids. Vol. 8. Methods in computational physics. Academic Press.

Allenspach, R. and Landolt, M. (1986). Spin polarized auger spectroscopy from Fe(100). Surface Science Letters, 171(3):L479 – L482.

Batirev, I., Hergert, W., Rennert, P., Stepanyuk, V., Oguchi, T., Katsnelson, A., Leiro, J., and Lee, K. (1998). Surface atomic forces and multilayer relaxation of W(001), W(110) and Fe/W(110). Surface Science, 417(1):151 – 158.

Beaurepaire, E., Merle, J.-C., Daunois, A., and Bigot, J.-Y. (1996). Ultrafast spin dynamics in ferromagnetic nickel. Phys. Rev. Lett., 76:4250–4253.

Bertacco, R., Merano, M., and Ciccacci, F. (1998). Spin dependent electron absorption in Fe(001)-p(1x1)O: A new candidate for a stable and efficient electron polarization analyzer. Applied Physics Letters, 72(16):2050–2052.

Besold, G., Heinz, K., Lang, E., and Müller, K. (1983). Structure analysis of Ir(100) 1x1 by LEED (100–500 ev). Journal of Vacuum Science & Technology A: Vacuum, Surfaces, and Films, 1(3):1473–1476.

Blaha, P., Schwarz, K., Sorantin, P., and Trickey, S. (1990). Full-potential, linearized augmented plane wave programs for crystalline systems. Computer Physics Communications, 59(2):399 – 415.

Bosse, J. C. L., Lopez, J., Gaubert, C., Gauthier, Y., and Baudoing, R. (1982). Threshold effects in LEED: resonance or interference effects? Journal of Physics C: Solid State Physics, 15(15):3425.

Braun, J., Math, C., Postnikov, A., and Donath, M. (2002). Surface resonances versus surface states on Fe(110). Phys. Rev. B, 65:184412.

Braun, J., Minár, J., Borek, S., and Ebert, H. (2013). Private communications.

Burgbacher, U., Braun, J., Brüning, A. K., Schmidt, A. B., and Donath, M. (2013). Spin-dependent surface barrier from very-low-energy electron diffraction fine structures: A feasibility study. Phys. Rev. B, 87:195411.

Calvert, R. L., Russell, G. J., and Haneman, D. (1977). Spin polarization and temperature effects in reflection diffraction from W(001). Phys. Rev. Lett., 39:1226–1229.

Connolly, J. (1977). Modern Theoretical Chemistry. Plenum, New York.

Dietz, R. E., McRae, E. G., and Campbell, R. L. (1980). Saturation of the image potential observed in low-energy electron reflection at Cu(001) surface. Phys. Rev. Lett., 45:1280–1284.

Drittler, B., Weinert, M., Zeller, R., and Dederichs, P. (1991). Vacancy formation energies of fcc transition metals calculated by a full potential green's function method. Solid State Communications, 79(1):31 – 35.

Ebert, H., Ködderitzsch, D., and Minár, J. (2011). Calculating condensed matter properties using the KKR-Green's function method - recent developments and applications. Reports on Progress in Physics, 74(9):096501.

Ebert et al., H. (2012). The munich SPR-KKR package: version 6.3 (http://olymp.cup.uni-muenchen.de/ak/ebert/SPRKKR).

Elmers, H.-J. (2007). Spin-polarized Low Energy Electron Diffraction. John Wiley & Sons, Ltd.

Feder, R. (1976). Spin polarization in low-energy electron diffraction from W(001). Phys. Rev. Lett., 36:598–600.

Feder, R. (1981). Spin-polarised low-energy electron diffraction. Journal of Physics C: Solid State Physics, 14(15):2049.

Feder, R. (1985). Polarized electrons in surface physics. World Scientific, Singapore.

Feder, R., Giebels, F., and Gollisch, H. (2012). Private communications.

Feder, R., Rosicky, F., and Ackermann, B. (1983). Relativistic multiple scattering theory of electrons by ferromagnets. Zeitschrift fr Physik B Condensed Matter, 52(1):31–36.

Fognini, A., Michlmayr, T. U., Bähler, T., Wetli, C., Vaterlaus, A., and Acremann, Y. (2012). Magnetic pulser and sample holder for time- and spin-resolved photoemission spectroscopy on magnetic materials. Review of Scientific Instruments, 83(6):063906.

Fognini, A., Salvatella, G., Sorgenfrei, F., Dell'Angela, M., Beye, M., Hieke, F., Kutnyakhov, D., Lushchyk, P., Eschenlohr, A., de Jong, S., Kukreja, R., Gerasimova, N., Redlin, H., Raabe, J., Oelsner, A., Stamm, C., Ramsperger, U., Stöhr, J., Dürr, H., Föhlisch, A., Wurth, W., Schönhense, G., Vaterlaus, A., Michlmayr, T., and Acremann, Y. (2013). Ultrafast loss of the classical magnetization. In DPG Spring Meeting of the Condensed Matter Section (SKM).

Gay, T. (2009). Chapter 4 physics and technology of polarized electron scattering from atoms and molecules. In E. Arimondo, P. R. B. and Lin, C. C., editors, Advances in Atomic Molecular and Optical Physics, volume 57 of Advances In Atomic, Molecular, and Optical Physics, pages 157 – 247. Academic Press.

Hahn, M., Schönhense, G., Jorge, E. A., and Jourdan, M. (2011). Significant spin polarization of Co_2MnGa heusler thin films on MgO(100) measured by ultraviolet photoemission spectroscopy. Applied Physics Letters, 98(23):232503.

Hedin, L. and Lundqvist, B. I. (1971). Explicit local exchange-correlation potentials. Journal of Physics C: Solid State Physics, 4(14):2064.

Heinz, K., Schmidt, G., Hammer, L., and Müller, K. (1985). Dynamics of the reconstruction process Ir(100) $1 \times 1 \longrightarrow 1 \times 5$. Phys. Rev. B, 32(10):6214–6221.

Hillebrecht, F. U., Jungblut, R. M., Wiebusch, L., Roth, C., Rose, H. B., Knabben, D., Bethke, C., Weber, N. B., Manderla, S., Rosowski, U., and Kisker, E. (2002). High-efficiency spin polarimetry by very-low-energy electron scattering from Fe(100) for spin-resolved photoemission. Review of Scientific Instruments, 73(3):1229–1234.

Huhne, T., Zecha, C., Ebert, H., Dederichs, P. H., and Zeller, R. (1998). Full-potential spin-polarized relativistic Korringa-Kohn-Rostoker method implemented and applied to bcc Fe, fcc Co, and fcc Ni. Phys. Rev. B, 58:10236–10247.

Jansen, H. J. F. and Freeman, A. J. (1984). Total-energy full-potential linearized augmented-plane-wave method for bulk solids: Electronic and structural properties of tungsten. Phys. Rev. B, 30:561–569.

Jones, R. and Jennings, P. (1988). LEED fine structure: Origins and applications. Surface Science Reports, 9(4):165 – 196.

Jones, R. O., Jennings, P. J., and Jepsen, O. (1984). Surface barrier in metals: A new model with application to W(001). Phys. Rev. B, 29:6474–6480.

Kalisvaart, M., O'Neill, M. R., Riddle, T. W., Dunning, F. B., and Walters, G. K. (1978). Electron-spin polarization in low-energy electron diffraction from tungsten (001). Phys. Rev. B, 17:1570–1578.

Kessler, J. (1976). Polarized Electrons. Springer Berlin.

Kirschner, J. (1985). Polarized electrons at surfaces. Springer Tracts in Mod. Phys, 106.

Kirschner, J. and Feder, R. (1979). Spin polarization in double diffraction of low-energy electrons from W(001): Experiment and theory. Phys. Rev. Lett., 42:1008–1011.

Kirschner, J., Giebels, F., Gollisch, H., and Feder, R. (2013). Spin-polarized electron scattering from pseudomorphic Au on Ir(001). Phys. Rev. B, 88:125419.

Koch, R., Borbonus, M., Haase, O., and Rieder, K. H. (1991). New aspects on the ir(110) reconstruction: Surface stabilization on mesoscopic scale via (331) facets. Phys. Rev. Lett., 67:3416–3419.

Koelling, D. D. and Harmon, B. N. (1977). A technique for relativistic spin-polarised calculations. Journal of Physics C: Solid State Physics, 10(16):3107.

Kohn, W. and Rostoker, N. (1954). Solution of the schrödinger equation in periodic lattices with an application to metallic lithium. Phys. Rev., 94:1111–1120.

Kohn, W. and Sham, L. J. (1965). Self-consistent equations including exchange and correlation effects. Phys. Rev., 140:A1133–A1138.

Kolbe, M., Chadov, S., Jorge, E. A., Schönhense, G., Felser, C., Elmers, H.-J., Kläui, M., and Jourdan, M. (2012). Test of band structure calculations for heusler compounds by spin-resolved photoemission spectroscopy. Phys. Rev. B, 86:024422.

Kolbe, M., Lushchyk, P., Petereit, B., Elmers, H. J., Schönhense, G., Oelsner, A., Tusche, C., and Kirschner, J. (2011). Highly efficient multichannel spin-polarization detection. Phys. Rev. Lett., 107:207601.

Korringa, J. (1947). On the calculation of the energy of a bloch wave in a metal. Physica, 13:392 – 400.

Kotani, T. and Akai, H. (1996). KKR-ASA method in exact exchange-potential band-structure calculations. Phys. Rev. B, 54:16502–16514.

Küppers, J. and Michel, H. (1979). Preparation of Ir(100)-1x1 surface structures by surface reactions and its reconstruction kinetics as determined with LEED, UPS and work function measurements. Applications of Surface Science, 3(2):179 – 195.

Kurzawa, R., Kämper, K.-P., Schmitt, W., and Güntherodt, G. (1986). Spin-resolved photoemission study of in situ grown epitaxial fe layers on w(110). Solid State Communications, 60(10):777 – 780.

Kutnyakhov, D., Lushchyk, P., Fognini, A., Perriard, D., Kolbe, M., Medjanik, K., Fedchenko, E., Nepijko, S., Elmers, H., Salvatella, G., Stieger, C., Gort, R., Bähler, T., Michlmayer, T., Acremann, Y., Vaterlaus, A., Giebels, F., Gollisch, H., Feder, R., Tusche, C., Krasyuk, A., Kirschner, J., and Schönhense, G. (2013). Imaging spin filter for electrons based on specular reflection from iridium (001). Ultramicroscopy, 130(0):63 – 69. Eighth International Workshop on LEEM/PEEM.

Landolt, M. (1986). High-resolution magnetic measurements at surfaces with spin polarized electrons. Applied Physics A, 41:83–89.

Lehwald, S., Chen, J. G., Kisters, G., Preuss, E., and Ibach, H. (1991). Surface-phonon dispersion investigation of the (1x1)–(5x1) reconstruction of the Ir(100) surface. Phys. Rev. B, 43:3920–3927.

Luschchyk, P., Oelsner, A., Kutnyakhov, D., Fognini, A., Acremann, Y., Vaterlaus, A., Rybnikov, V., and Schönhense, G. (2014). Multi-segmented delayline detector: A new data acquisition strategy for fel and other timing experiments. In Preparation.

Malmström, G. and Rundgren, J. (1980). A program for calculation of the reflection and transmission of electrons through a surface potential barrier. Computer Physics Communications, 19(2):263 – 270.

McRae, E. G., Pierce, D. T., Wang, G. C., and Celotta, R. J. (1981). Polarized-low-energy-electron-diffraction study of the mechanism of electron reflection from W(001) at low energies. Phys. Rev. B, 24:4230–4239.

Miesch, S., Fognini, A., Acremann, Y., Vaterlaus, A., and Michlmayr, T. U. (2011). Fe on W(110), a stable magnetic reference system. Journal of Applied Physics, 109(1):013905.

Moruzzi, V. L., Janak, J. F., and Williams, A. R. (1978). Calculated electronic properties of metals / by V.L. Moruzzi, J.F. Janak, A.R. Williams. Pergamon Press New York.

Musket, R., McLean, W., Colmenares, C., Makowiecki, D., and Siekhaus, W. (1982). Preparation of atomically clean surfaces of selected elements: A review. Applications of Surface Science, 10(2):143 – 207.

Nekovee, M., Crampin, S., and Inglesfield, J. E. (1993). Magnetic splitting of image states at Fe(110). Phys. Rev. Lett., 70:3099–3102.

Oelsner, A., Schmidt, O., Schicketanz, M., Klais, M., Schönhense, G., Mergel, V., Jagutzki, O., and Schmidt-Böcking, H. (2001). Microspectroscopy and imaging using a delay line detector in time-of-flight photoemission microscopy. Review of Scientific Instruments, 72(10):3968–3974.

Okuda, T. (2013). Private communications.

Okuda, T., Takeichi, Y., Maeda, Y., Harasawa, A., Matsuda, I., Kinoshita, T., and Kakizaki, A. (2008). A new spin-polarized photoemission spectrometer with very high efficiency and energy resolution. Review of Scientific Instruments, 79(12):123117.

O'Neill, M. R., Kalisvaart, M., Dunning, F. B., and Walters, G. K. (1975). Electron-spin polarization in low-energy electron diffraction from tungsten (001). Phys. Rev. Lett., 34:1167–1170.

Papanikolaou, N., Zeller, R., and Dederichs, P. H. (2002). Conceptual improvements of the KKR method. Journal of Physics: Condensed Matter, 14(11):2799.

Pendry, J. (1974). Low Energy Electron Diffraction: The Theory and Its Application to Determination of Surface Structure. Techniques of Physics Series. Academic Press.

Phoibos (100/150). User manual for the Hemispherical Energy Analyzer Series PHOIBOS 100/150. SPECS GmbH-Surface Analysis and Computer Technology.

Pierce, D. T., Celotta, R. J., Wang, G., Unertl, W. N., Galejs, A., Kuyatt, C. E., and Mielczarek, S. R. (1980). The GaAs spin polarized electron source. Review of Scientific Instruments, 51(4):478–499.

Rundgren, J. and Malmstrom, G. (1977). Transmission and reflection of low-energy electrons at the surface barrier of a metal. Journal of Physics C: Solid State Physics, 10(23):4671.

Samarin, S., Williams, J., Artamonov, O., Henk, J., and Feder, R. (2010). Spin-asymmetry in elastic scattering of low-energy electrons from ultrathin au films on W(110). Surface Science, 604:1833 – 1839.

Samarin, S., Williams, J., Artamonov, O., Pravica, L., Sudarshan, K., Guagliardo, P., Giebels, F., Gollisch, H., and Feder, R. (2013). Intensity asymmetry of the (00) diffracted spin-polarized electron beam scattered from W(110): Azimuthal dependence. Applied Physics Letters, 102(25):251607.

Samarin, S. N., Williams, J. F., Sergeant, A. D., Artamonov, O. M., Gollisch, H., and Feder, R. (2007). Spin-dependent reflection of very-low-energy electrons from W(110). Phys. Rev. B, 76:125402.

Schlosser, H. and Marcus, P. M. (1963). Composite wave variational method for solution of the energy-band problem in solids. Phys. Rev., 131:2529–2546.

Schwarz, K. and Blaha, P. (2003). Solid state calculations using {WIEN2k}. Computational Materials Science, 28(2):259 – 273. Proceedings of the Symposium on Software Development for Process and Materials Design.

Schwarz, K., Blaha, P., and Madsen, G. (2002). Electronic structure calculations of solids using the WIEN2k package for material sciences. Computer Physics Communications, 147:71 – 76.

Slater, J. (1974). The self-consistent field for molecules and solids. Number 4 in Quantum theory of molecules and solids. McGraw-Hill.

Slater, J. C. (1937). Wave functions in a periodic potential. Phys. Rev., 51:846–851.

Stefanou, N., Akai, H., and Zeller, R. (1990). An efficient numerical method to calculate shape truncation functions for wigner-seitz atomic polyhedra. Computer Physics Communications, 60(2):231 – 238.

Stefanou, N. and Zeller, R. (1991). Calculation of shape-truncation functions for voronoi polyhedra. Journal of Physics: Condensed Matter, 3(39):7599.

Stryganyuk, G., Kozina, X., Fecher, G. H., Ouardi, S., Chadov, S., Felser, C., Schönhense, G., Lushchyk, P., Oelsner, A., Bernhard, P., Ikenaga, E., Sugiyama, T., Sukegawa, H., Wen, Z., Inomata, K., and Kobayashi, K. (2012). Spin polarimetry and magnetic dichroism on a buried magnetic layer using hard x-ray photoelectron spectroscopy. Japanese Journal of Applied Physics, 51(1):016602.

Tamura, E. and Feder, R. (1986). Three-dimensional surface potential barrier in electron-solid scattering: Theory and application to W(001). Solid State Communications, 58(10):729 – 733.

Thurgate, S. M. and Sun, C. (1995). Very-low-energy electron-diffraction analysis of oxygen on Cu(001). Phys. Rev. B, 51:2410–2417.

Tusche, C., Ellguth, M., Krasyuk, A., Winkelmann, A., Kutnyakhov, D., Lushchyk, P., Medjanik, K., Schönhense, G., and Kirschner, J. (2013). Quantitative spin polarization analysis in photoelectron emission microscopy with an imaging spin filter. Ultramicroscopy, 130(0):70 – 76. Eighth International Workshop on LEEM/PEEM.

Tusche, C., Ellguth, M., Ünal, A. A., Chiang, C.-T., Winkelmann, A., Krasyuk, A., Hahn, M., Schönhense, G., and Kirschner, J. (2011). Spin resolved photoelectron microscopy using a two-dimensional spin-polarizing electron mirror. Applied Physics Letters, 99(3):032505.

Venus, D. (1993). Use of spin-polarized LEED rotation curves to study disordered surfaces: W(001)-(1x 1) and W(001)-2H(1x1). Surface Science, 291(3):418 – 428.

von Barth, U. and Hedin, L. (1972). A local exchange-correlation potential for the spin polarized case. Journal of Physics C: Solid State Physics, 5(13):1629.

Wang, G.-C., Celotta, R. J., and Pierce, D. T. (1981). Polarized low-energy-electron diffraction from W(100). Phys. Rev. B, 23:1761–1770.

Weinert, M., Wimmer, E., and Freeman, A. J. (1982). Total-energy all-electron density functional method for bulk solids and surfaces. Phys. Rev. B, 26:4571–4578.

Wimmer, E., Krakauer, H., Weinert, M., and Freeman, A. J. (1981). Full-potential self-consistent linearized-augmented-plane-wave method for calculating the electronic structure of molecules and surfaces: O_2 molecule. Phys. Rev. B, 24:864–875.

Winkelmann, A., Hartung, D., Engelhard, H., Chiang, C.-T., and Kirschner, J. (2008). High efficiency electron spin polarization analyzer based on exchange scattering at Fe/W(001). Review of Scientific Instruments, 79(8):083303.

Yu, D., Math, C., Meier, M., Escher, M., Rangelov, G., and Donath, M. (2007). Characterisation and application of a spleed-based spin polarisation analyser. Surface Science, 601(24):5803 – 5808.

Zabloudil, J., Hammerling, R., Weinberger, P., and Szunyogh, L. (2005). Electron Scattering in Solid Matter. Springer-Verlag Berlin Heidelberg, Germany, Berlin.

Zakeri, K., Peixoto, T., Zhang, Y., Prokop, J., and Kirschner, J. (2010). On the preparation of clean tungsten single crystals. Surface Science, 604(2):L1 – L3.

Zeller, R. (1987). Multiple-scattering solution of schrodinger's equation for potentials of general shape. Journal of Physics C: Solid State Physics, 20(16):2347.

List of publications

Part of this work has been published in:

- *Imaging spin filter for electrons based on specular reflection from iridium (001).* Kutnyakhov, D., Lushchyk, P., Fognini, A., Perriard, D., Kolbe, M., Medjanik, K., Fedchenko, E., Nepijko, S., Elmers, H. J., Salvatella, G., Stieger, C., Gort, R., Bähler, T., Michlmayer, T., Acremann, Y., Vaterlaus, A., Giebels, F., Gollisch, H., Feder, R., Tusche, C., Krasyuk, A., Kirschner, J., and Schönhense, G. Ultramicroscopy, **130**, 63, (2013).

- *Quantitative spin polarization analysis in photoelectron emission microscopy with an imaging spin filter.* Tusche, C., Ellguth, M., Krasyuk, A., Winkelmann, A., Kutnyakhov, D., Lushchyk, P., Medjanik, K., Schönhense, G., and Kirschner, J. Ultramicroscopy, **130**, 70, (2013).

- *Specular reflection of spin-polarized electrons from W(001) spin-filter crystal in a larger range of scattering energies and angles.* Kutnyakhov, D., Elmers, H. J., Tusche, C. Kirschner, J., Borek, S., Braun. J., Minár, J. and Schönhense, G. In Preparation, (2014).

- *Multi-segmented delayline detector: A new data acquisition strategy for FEL and other timing experiments.* Luschchyk, P., Oelsner, A., Kutnyakhov, D., Fognini, A., Acremann, Y., Vaterlaus, A., Rybnikov, V., and Schönhense, G. In Preparation, (2014).

Further publications:

- *Electronic structure of large disc-type donors and acceptors.* Medjanik, K., Kutnyakhov, D., Nepijko, S. A., Schoenhense, G., Naghavi, S., Alijani, V., Felser, C., Koch, N., Rieger, R., Baumgarten, M., and Muellen, K. PHYSICAL CHEMISTRY CHEMICAL PHYSICS, **12**, 7184, (2010).

- *Theoretical study of new acceptor and donor molecules based on polycyclic aromatic hydrocarbons.* Naghavi, S. S., Gruhn, T., Alijani, V., Fecher, G. H., Felser, C., Medjanik, K., Kutnyakhov, D., Nepijko, S. A., Schoenhense, G., Rieger, R., Baumgarten, M., and Muellen, K. JOURNAL OF MOLECULAR SPECTROSCOPY, **265**, 95, (2011).

- *Sensor and microelectronic elements based on nanoscale granular systems.* Nepijko, S. A., Kutnyakhov, D., Protsenko, S. I., Odnodvorets, L. V., and Schoenhense, G. JOURNAL OF NANOPARTICLE RESEARCH, **13**, 6263, (2011).

- *Measurement of object height in emission electron microscopy.* Schertz, F., Kutnyakhov, D., Schuppler, S., Nagel, P., Nepijko, S. A., and Schoenhense, G. APPLIED PHYSICS A-MATERIALS SCIENCE & PROCESSING, **102**, 253, (2011).

- *Structure and magnetic properties of one-dimensional chains of ferromagnetic nanoparticles.* Nepijko, S. A., Kutnyakhov, D., Protsenko, I. E., Elmers, H. J., and Schoenhense, G. APPLIED PHYSICS A-MATERIALS SCIENCE & PROCESSING, **109**, 699, (2012).

- *Charge transfer in the novel donor-acceptor complexes tetra- and hexamethoxypyrene with tetracyanoquinodimethane studied by HAXPES.* Medjanik, K., Gloskovskii, A., Kutnyakhov, D., Felser, C., Chercka, D., Baumgarten, M., Muellen, K., and Schoenhense, G. J. OF ELECTRON SPECTROSCOPY AND RELATED PHENOMENA, **185**, 77, (2012).

- *Beyond the Heisenberg Model: Anisotropic Exchange Interaction between a Cu-Tetraazaporphyrin Monolayer and $Fe_3O_4(100)$.* Klanke, J., Rentschler, E., Medjanik, K., Kutnyakhov, D., Schoenhense, G., Krasnikov, S., Shvets,

I. V., Schuppler, S., Nagel, P., Merz, M., and Elmers, H. J. PHYSICAL REVIEW LETTERS, **110**, 137202, (2013).

- *Hard X-ray photoemission study of the Fabre salts (TMTTF)2X (X = SbF6 and PF6)* Medjanik, K., de Souza, M., Kutnyakhov, D., Gloskovskii, A., Müller, J., Lang, M., Pouget, J.-P., Foury-Leylekian, P., Moradpour, A., Elmers, H.-J., Schönhense, G. In Preparation, (2014)